

Search for the decay  $K_L \rightarrow \pi^0 \mu^+ \mu^-$

Masayoshi Sadamoto  
Osaka University

February 26, 1999

# Acknowledgements

Fisrt of all, I would like to thank my advisor, Prof. Yorikiyo Nagashima for his gentle support and supervising my education.

I would like to thank all the KTeV collabollation for their help with the experiment. Especially, I would like to thank Greg Bock and Bob Hsiung who are my supervisor in U.S. I also greatly appreciate many discussions with Richard J. Tesarek about muons.

I would like to mension especially Kazunori Hanagaki who were always willing to take time out to help with questions about analysis. I owe thanks to Tsuyoshi Nakaya, Takanori Hara, Motoharu Yagi, Koji Adachi, Takeo Kawasaki, Toshihiro Tsuji, Takayuki Yamaguchi, and Fumihiko Kato. They gave me usefull informations and discussions. I would like to thank all the graduate students in Nagashima group at Osaka University.

I would like to thank Taku Yamanaka for being my advisor for these years, for encouraging me to work on this search, giving me, and supporting my life in U.S.A. This thesis could not exist without his advice.

Masayoshi Sadamoto  
Toyonaka, Osaka  
Feburuary 1999

# Contents

<b>1</b>	<b>Introduction</b>	<b>2</b>
1.1	CP Violation in Standard Model . . . . .	2
1.1.1	Standard Model . . . . .	2
1.1.2	CP violation . . . . .	2
1.1.3	CP violation in Neutral Kaon system . . . . .	3
1.2	$K_L \rightarrow \pi^0 \mu^+ \mu^-$ . . . . .	7
1.2.1	Direct CP Violating Contribution . . . . .	7
1.2.2	Other Contribution . . . . .	8
1.2.3	$K_L \rightarrow \pi^0 \mu^+ \mu^-$ in Other Theories . . . . .	10
1.2.4	Theoretical Predictions Summary . . . . .	11
1.3	Summary . . . . .	11
1.4	Overview . . . . .	12
<b>2</b>	<b>KTeV Experiment</b>	<b>13</b>
2.1	KTeV Experiment . . . . .	13
2.1.1	$K_L$ Beam . . . . .	13
2.2	Detector . . . . .	15
2.2.1	Decay Region and Photon Veto Counter . . . . .	15
2.2.2	Spectrometer . . . . .	15
2.2.3	Trigger Hodoscopes . . . . .	18
2.2.4	Pure-CsI Electromagnetic Calorimeter . . . . .	18
2.2.5	Muon System . . . . .	21
2.3	Trigger . . . . .	23
2.3.1	Level 1 and Level 2 trigger . . . . .	23
2.3.2	Level 3 trigger and Data Acquisition System . . . . .	24
2.4	Accidental Trigger . . . . .	25
2.5	Data Taking . . . . .	25
2.5.1	Physics Run . . . . .	25
2.6	$K_L \rightarrow \pi^0 \mu^+ \mu^-$ Data Set . . . . .	25
<b>3</b>	<b>Monte Carlo Simulation</b>	<b>28</b>
3.1	Production of $K_L$ Beam . . . . .	28
3.2	$K_L$ Decay . . . . .	29
3.2.1	$K_L \rightarrow \pi^0 \mu^+ \mu^-$ . . . . .	30
3.2.2	$K_L \rightarrow \pi^0 \pi^+ \pi^-$ . . . . .	30

3.2.3	$K_L \rightarrow \mu^+ \mu^- \gamma, K_L \rightarrow \mu^+ \mu^- \gamma \gamma$	30
3.2.4	$K_L \rightarrow \pi^\pm \mu^\mp \nu(\bar{\nu})$	30
3.3	Tracing of Decay Products	31
3.3.1	Muon Scattering in Muon System	31
3.4	$\pi^\pm$ in Monte Carlo Simulation	31
3.4.1	$\pi^\pm$ Decay	32
3.4.2	$\pi^\pm$ Punch Through Muon System	32
3.4.3	Summary of $\pi^\pm$ misidentification simulation	32
3.5	Detector Response	33
3.5.1	Photon Veto Counters	33
3.5.2	Drift Chamber	34
3.5.3	CsI Calorimeter	35
3.5.4	Trigger Hodoscopes and Muon Counters	36
3.6	Accidental Activity	36
<b>4</b>	<b>Event Selection</b>	<b>37</b>
4.1	Backgrounds to $K_L \rightarrow \pi^0 \mu^+ \mu^-$	37
4.1.1	$K_L \rightarrow \mu^+ \mu^- \gamma \gamma, K_L \rightarrow \mu^+ \mu^- \gamma + \gamma_{acc}$	38
4.1.2	Kaon Decays including $\pi^\pm$	38
4.2	Policy of $K_L \rightarrow \pi^0 \mu^+ \mu^-$ Analysis	39
4.3	Event Reconstruction	40
4.3.1	Cluster Finding	40
4.3.2	Finding Track Candidates	41
4.3.3	Vertex Finding	42
4.3.4	Photon Veto	44
4.4	Particle Identification	44
4.4.1	$\mu$ identification	44
4.4.2	Gamma identification	45
4.5	Kinematic cuts	46
4.5.1	$\pi^0$ mass	46
4.5.2	Invariant Mass of the Charged Tracks( $M_{\mu\mu}$ )	47
4.5.3	Missing longitudinal momentum parameter( $P_{\pi^0}^2$ )	47
4.5.4	$P_T^2$ and Kaon Invariant Mass	48
4.6	Acceptance Correction	49
4.6.1	Energy deposit by muon	49
4.6.2	MU3 bank efficiency	50
4.7	Analysis of the $K_L \rightarrow \pi^0 \pi^+ \pi^-$	51
4.8	Sensitivity for $K_L \rightarrow \pi^0 \mu^+ \mu^-$	52
<b>5</b>	<b>Background Estimation</b>	<b>57</b>
5.1	Number of Background Events	57
5.2	Correction for Background Estimation	58
5.3	Uncertainty of Background Estimation	58
5.3.1	Branching Ratio	58
5.3.2	Monte Carlo Statistics	59

5.3.3	Statistical error on the number of $K_L$ decays . . . . .	59
5.3.4	Summary of Background Estimation . . . . .	60
5.4	Consistency between Data and MC . . . . .	60
5.4.1	Comparison of the Shape of the Distribution. . . . .	60
5.4.2	Comparisons in Side Bands . . . . .	61
5.4.3	Summary . . . . .	63
<b>6</b>	<b>Systematic Uncertainties on the Sensitivity</b>	<b>64</b>
6.1	Branching Ratio . . . . .	64
6.2	Statistical Uncertainty . . . . .	64
6.3	Energy Measurement . . . . .	65
6.4	Momentum measurement . . . . .	65
6.5	$\chi^2_{vertex}$ and $\pi^0$ mass . . . . .	66
6.6	Inefficiency of Drift Chamber . . . . .	66
6.7	Particle Identification . . . . .	67
6.8	Different trigger Uncertainty . . . . .	67
6.9	Summary . . . . .	68
<b>7</b>	<b>Result and Discussion</b>	<b>69</b>
7.1	Criteria for claiming the observation of $K_L \rightarrow \pi^0 \mu^+ \mu^-$ . . . . .	69
7.2	Analysis of data in the Masked Region . . . . .	70
7.3	Result . . . . .	70
7.4	Discussions . . . . .	71
7.4.1	Theory . . . . .	71
7.4.2	Future Perspective of Searching for $K_L \rightarrow \pi^0 \mu^+ \mu^-$ . . . . .	71
<b>8</b>	<b>Conclusion</b>	<b>74</b>
<b>A</b>	<b><math>K_L \rightarrow \mu^+ \mu^- \gamma \gamma</math> Analysis</b>	<b>75</b>
A.1	Backgrounds to $K_L \rightarrow \mu^+ \mu^- \gamma \gamma$ . . . . .	75
A.2	Event Selection . . . . .	76
A.2.1	Photon Energy . . . . .	76
A.2.2	$\pi^0$ mass . . . . .	76
A.2.3	Missing Longitudinal Momentum Parameter( $P_{\pi^0}^2$ ) . . . . .	77
A.2.4	Invariant Mass of the Charged Tracks( $M_{\mu\mu}$ ) . . . . .	78
A.2.5	Angle between 2 Photons . . . . .	78
A.2.6	Kaon mass and $P_T^2$ . . . . .	79
A.2.7	Summary of the Event Selection . . . . .	79
A.3	Background Estimation . . . . .	83
A.3.1	Correction for Background Estimation . . . . .	83
A.3.2	Uncertainty of the background estimation . . . . .	83
A.3.3	Summary for backgrounds . . . . .	84
A.3.4	Consistency between Data and MC . . . . .	84
A.3.5	Summary of the background estimation . . . . .	85
A.4	Criteria for claiming $K_L \rightarrow \mu^+ \mu^- \gamma \gamma$ observation . . . . .	88
A.5	Result . . . . .	88



# List of Figures

1.1	The box diagrams which are expected to provide the dominant contribution to $K^0-\bar{K}^0$ mixing. . . . .	5
1.2	The penguin diagram which is expected to provide the direct CP violation. . . . .	6
1.3	The direct CP violation. The upper figure is an electroweak penguin diagram. The lower figure is called W box diagram. . .	8
1.4	The diagram of the indirect CP violation . . . . .	9
1.5	CP-conserving contribution . . . . .	9
2.1	The energy spectrum of the kaon at the target . . . . .	14
2.2	KTeV Spectrometer . . . . .	16
2.3	The photon veto detectors. The left figure shows a RC which was located inside the vacuum region. The right figure shows the SA and CIA. . . . .	17
2.4	Wire geometry of a drift chamber . . . . .	18
2.5	Schematic view of Trigger Hodoscopes(V, V' bank). . . . .	19
2.6	The upper plot shows the E/P distribution for electrons in $K_L \rightarrow \pi e \nu$ , where E denotes an measured energy by the calorimeter, and P represents a measured momentum by the spectrometer. The lower plot shows the intrinsic energy resolution of the calorimeter as a function of electron momentum. . . . .	20
2.7	Pure-CsI Electromagnetic Calorimeter . . . . .	21
2.8	The MU2 bank. . . . .	22
2.9	The upper figure shows MU3x bank. The lower figure illustrates MU3y bank. . . . .	26
2.10	KTeV Data Acquisition System . . . . .	27
3.1	The $\pi^\pm$ punch through probability as a function of $\pi^\pm$ momentum, obtained by GEANT simulation. The line shows the result from the linear fit. . . . .	33
3.2	The probability that $\pi^\pm$ is identified as muon for MC(solid line) and data(dot) as a function of $\pi^\pm$ momentum. The dot shows the probability of the misidentification of the $\pi^\pm$ in $K_L \rightarrow \pi e \nu$ data. The dashed line shows the probability of misidentifying by $\pi^\pm$ decay in MC. The solid line shows the sum of the dashed line and Figure 3.1. . . . .	34

4.1	The deviation of sum of drift distance from the offset of 6.35 mm.	42
4.2	The distributions for the vertex variables for the $K_L \rightarrow \pi^0 \mu^+ \mu^-$ after the vertex reconstruction. The top left plot shows the Z distribution of the reconstructed vertex. The top right plot shows the $\chi_{vertex}^2$ distribution. The bottom plots shows the projected position of the vertex from the target to the CsI calorimeter. The bottom left(right) plot shows the X(Y) distribution of the projection. The arrows in the plots show our requirements for the vertex. . . . .	43
4.3	The energy distribution of the cluster associated with a track at CsI calorimeter for $K_L \rightarrow \pi^0 \mu^+ \mu^-$ trigger events. . . . .	45
4.4	The efficiency for detecting muons by MU3x bank as a function of its momentum. We required more than 10GeV/c for muon momentum as shown by arrow in the plot. . . . .	46
4.5	The $\mu$ momentum distribution of the $K_L \rightarrow \pi^0 \mu^+ \mu^-$ for the $K_L \rightarrow \pi^0 \mu^+ \mu^-$ trigger events after the event reconstruction. We required the momentum to be greater than 10GeV/c and less than 100GeV/c as shown by arrow in the plot. . . . .	47
4.6	The upper(lower) plot shows the number of isolated hits in the MU3X(MU3Y) bank for the $K_L \rightarrow \pi^0 \mu^+ \mu^-$ trigger data after the event reconstruction. . . . .	48
4.7	The $\pi^0$ distribution of the $K_L \rightarrow \pi^0 \mu^+ \mu^-$ MC after the event reconstruction. The arrow in the plot shows our requirement( $132 < M_{\gamma\gamma} MeV/c^2 <$ . . . . .	49
4.8	$M_{\mu\mu}$ distribution for each decay after the $\pi^0$ mass cut. The upper plot shows distribution of $K_L \rightarrow \pi^0 \mu^+ \mu^-$ . The middle plot shows the distribution of the $K_L \rightarrow \mu^+ \mu^- \gamma\gamma$ . The lower plot shows the distribution of the $K_L \rightarrow \pi^\pm \mu^\mp \nu(\bar{\nu})$ . We required $M_{\mu\mu} < 0.35 GeV/c^2$ as indicated by the arrow. . . . .	50
4.9	The upper plot shows $P_{\pi^0}^2$ distribution after $M_{\mu\mu}$ cut for $K_L \rightarrow \pi^0 \mu^+ \mu^-$ (solid line), $K_L \rightarrow \pi^0 \pi^+ \pi^-$ (dashed line), $K_L \rightarrow \pi^\pm \mu^\mp \nu(\bar{\nu})$ (dotted line), and $K_L \rightarrow \mu^+ \mu^- \gamma\gamma$ (dot-dash line) as normalized by area. . . . .	51
4.10	The upper plot shows the reconstructed $\pi^0 \mu^+ \mu^-$ mass distribution. The lower plot shows $P_T^2$ of $K_L \rightarrow \pi^0 \mu^+ \mu^-$ MC events after the event reconstruction. The arrow in these plots shows our requirement. ( $492 < M_{\pi^0 \mu^+ \mu^-} MeV/c^2 < 504, P_T^2 < 100 (MeV/c)^2$ ) . . . . .	52
4.11	The muon energy deposit in the CsI calorimeter. The solid line(dot) shows the energy deposit by muon in MC sample(data). . . . .	53
4.12	The detection efficiency of MU3 bank for muons as a function of the extrapolated track position at MU3x bank. The muons were selected to have momentum to be greater than 40GeV/c. . . . .	54

4.13	The top left(right) plot shows the kaon mass( $P_T^2$ ) distribution of $K_L \rightarrow \pi^0\pi^+\pi^-$ MC events and data after all cuts. The bottom left plot shows the momentum distribution of the track in the $K_L \rightarrow \pi^0\pi^+\pi^-$ events. The bottom right plot shows the vertex z position. Dots represent the distribution of the observed events. Open histogram shows that of MC events. The MC distribution was normalized by the measured number of decayed $K_L$ . . . . .	55
4.14	The left plot shows $\gamma\gamma$ mass distribution of data(dot) and MC(open histogram) of the accepted $K_L \rightarrow \pi^0\pi^+\pi^-$ events as normalization. The right plot shows $\chi_{vertex}^2$ distribution of data(dot) and MC(open histogram). . . . .	56
5.1	The plot (A) shows the kaon mass distribution with all requirements except for kaon mass. The plot (B) shows the $P_{\pi^0}^2$ distribution without kinematic requirements. The plot (C) shows $M_{\mu\mu}$ distribution after the particle identification. The dots represent data, open histogram represent the summed MC. . . . .	61
5.2	The kaon mass distribution in the $P_T^2 < 100(MeV/c)^2$ region. The dot indicates the data. The open histogram represents the summed MC. . . . .	62
5.3	The $P_T^2$ distribution in the kaon mass region. The dots indicate data. The open histogram represents the summed MC. . . . .	63
6.1	The illumination of the tracks at the first drift chamber. . . . .	67
7.1	The reconstructed $\pi^0\mu^+\mu^-$ mass distribution with all the cuts except for the mass cut. There are two events in the masked region. Dots are data. Open histogram is sum of all background MC events. . . . .	70
A.1	The energy distribution of the photon in the $K_L \rightarrow \mu^+\mu^-\gamma$ (solid) and the accidental photon(dot). . . . .	76
A.2	The $\pi^0$ distribution of the $K_L \rightarrow \mu^+\mu^-\gamma\gamma$ MC events(solid line) and $K_L \rightarrow \pi^0\pi^+\pi^-$ MC events(dash line) after particle identification. These distributions are normalized by area. . . . .	77
A.3	$P_{\pi^0}^2$ distribution for $K_L \rightarrow \mu^+\mu^-\gamma\gamma$ (solid line) and $K_L \rightarrow \pi^0\pi^+\pi^-$ (dashed line) which include both $\pi^\pm$ decayed in flight. We required the $P_{\pi^0}^2$ to be less than -0.06 as indicated arrow in the plot. The distributions are normalized by area. . . . .	78
A.4	$M_{\mu\mu}$ distribution for each decay after the $\pi^0$ mass cut. The upper plot shows the distribution for the $K_L \rightarrow \mu^+\mu^-\gamma\gamma$ . The lower plot shows the distribution for the $K_L \rightarrow \pi^\pm\mu^\mp\nu(\bar{\nu})$ . We required $M_{\mu\mu} < 0.34GeV/c^2$ as indicated by the arrow. . . . .	79
A.5	The illustration showing the angle between two photons in the center of mass system. . . . .	80

A.6	The $\cos\theta_{\gamma\gamma}$ distribution of $K_L \rightarrow \mu^+\mu^-\gamma\gamma$ and $K_L \rightarrow \pi^\pm\mu^\mp\nu(\bar{\nu})$ . The solid(dashed) line represents the distribution for $K_L \rightarrow \mu^+\mu^-\gamma\gamma(K_L \rightarrow \pi^\pm\mu^\mp\nu(\bar{\nu}))$ after $P_{\pi^0}^2$ cut. The arrow shows our requirement. . . . .	81
A.7	The kaon mass distribution in the $P_T^2 < 100(MeV/c)^2$ region. The dot indicates the data. The open histogram represents the summed MC. The dashed line shows the contribution from $K_L \rightarrow \mu^+\mu^-\gamma + \gamma_{acc}$ . Most of the other contribution is from $K_L \rightarrow \pi^\pm\mu^\mp\nu(\bar{\nu}) + 2\gamma_{acc}$ . . . . .	86
A.8	The $P_T^2$ distribution in the kaon mass region. The dots indicate data. The open histogram represents the summed MC. . . . .	87
A.9	The reconstructed mass distribution with all cuts except for the mass cut. There are two events in the masked region. . . . .	89
A.10	The spectrum of the minimum energy photon in our $K_L \rightarrow \mu^+\mu^-\gamma\gamma$ MC events. The solid line shows the spectrum at the generation. The dashed line shows the spectrum for the accepted events. The arrow shows the cutoff which was used to calculate the branching ratio. . . . .	90
B.1	The $\delta_{scat}$ distribution. The left plot shows the distribution for 10~11GeV/c muons. The right plot shows the distribution for 30~31GeV/c. . . . .	92
B.2	The $\delta_{scat}$ distribution as a function of the muon momentum. The upper plot shows the distribution for x direction. The lower plot shows the distribution for y direction. . . . .	92
B.3	The $\delta_{scat}$ distribution as a function of $\mu$ momentum for data(solid) and MC(dash) in $K_L \rightarrow \pi^\pm\mu^\mp\nu(\bar{\nu})$ decays. . . . .	93

# List of Tables

1.1	Theoretical prediction for each contribution . . . . .	11
2.1	The period of the experiments . . . . .	13
2.2	The position and size of the collimator . . . . .	14
2.3	The position and the size of the photon veto detectors . . . . .	17
2.4	The position and size of the drift chamber . . . . .	18
2.5	The shields and banks in the Mu system . . . . .	22
2.6	Summary of the Trigger condition Symbols . . . . .	23
2.7	The condition difference of the periods. . . . .	25
3.1	The parameters used by Malensek [22]. . . . .	29
4.1	Backgrounds to $K_L \rightarrow \pi^0 \mu^+ \mu^-$ with their branching ratio. Branching ratio of $K_L \rightarrow \mu^+ \mu^- \gamma \gamma$ was calculated in Appendix A. $\gamma_{acc}$ means the accidental photon. The infrared cutoff for $K_L \rightarrow \mu^+ \mu^- \gamma \gamma$ analysis is set to 10 MeV in the center of mass system. . . . .	37
4.2	Analysis cuts and efficiencies for $K_L \rightarrow \pi^0 \mu^+ \mu^-$ . . . . .	56
5.1	Summary of the expected number of events from various background sources. D represents a $\pi^\pm$ decayed in flight before CsI calorimeter. P denotes that a $\pi^\pm$ punched through the muon filter. . . . .	57
5.2	The summary of the correction for the misidentification. D represented a $\pi^\pm$ decayed in flight before CsI calorimeter. P meant that a $\pi^\pm$ punched through the muon filters. . . . .	58
5.3	The summary of the uncertainties in the branching ratio of the background decays. . . . .	59
5.4	The summary of the uncertainties from MC statistics for the background decays to $K_L \rightarrow \pi^0 \mu^+ \mu^-$ . D represented a $\pi^\pm$ decayed in flight before the CsI calorimeter. P meant that a $\pi^\pm$ punched through the muon filters. . . . .	59
5.5	Summary of the number of the events from various background sources with their uncertainties after the correction. D represented a $\pi^\pm$ decayed in flight before the CsI calorimeter. P represented a $\pi^\pm$ punched through the muon filter. . . . .	60
6.1	Systematic uncertainty from the number of generated MC. . . . .	64

6.2	Summary of systematic error studies on the energy measurement. . . . .	65
6.3	Summary of systematic uncertainties on the momentum measurement. . . . .	66
6.4	The systematic error on the single event sensitivity from each source. . . . .	68
7.1	Poisson distribution of the expected number of background events while 0.96 events are expected. . . . .	69
A.1	Background candidates to $K_L \rightarrow \mu^+ \mu^- \gamma \gamma$ with their branching ratio . . . . .	75
A.2	Analysis Cuts and efficiencies for $K_L \rightarrow \mu^+ \mu^- \gamma \gamma$ . . . . .	81
A.3	The systematic error from each source. . . . .	82
A.4	The summary of the correction for the misidentification. D represents a $\pi^\pm$ decayed in flight before the CsI calorimeter. P means that a $\pi^\pm$ punched through the muon filters. . . . .	83
A.5	The summary of the uncertainty of the background decays to $K_L \rightarrow \mu^+ \mu^- \gamma \gamma$ from the MC statistics. . . . .	84
A.6	The summary of the uncertainty from the branching ratio of the background decays. . . . .	84
A.7	Summary of the number of the events from various background source. D represented a $\pi^\pm$ decayed in flight before CsI calorimeter. P denoted that a $\pi^\pm$ punched through the muon filter. . . . .	85
A.8	Poisson probabilities to the observed background events while 0.704 background events are expected. . . . .	88

### **Abstract**

A search for  $K_L \rightarrow \pi^0 \mu^+ \mu^-$  decay is carried out as a part of E799-II experiment at Fermilab. Within the Standard Model, the  $K_L \rightarrow \pi^0 \mu^+ \mu^-$  decay is expected to include the direct CP violating processes.

We observed two events, which are consistent with 0.96 background events expected from our Monte Carlo simulation. We set an upper limit

$$Br(K_L \rightarrow \pi^0 \mu^+ \mu^-) < 4.1 \times 10^{-10}$$

at the 90% confidence level. This result represents an improvement of a factor 12 over the current limit listed by Particle Data Group.

# Chapter 1

## Introduction

Conservation laws have played an important role in physics for many years. In the domain of the quantum phenomena, three discrete transformations such as parity, charge conjugation, and time reversal are important.

“P(parity)” operation reverses sign of the coordinate, and thus the momentum of a particle without flipping its spin. “C(charge conjugation)” operation changes particles to their anti-particles. It means that the quantum numbers of a particle change their signs. “T(time reversal)” reverses the direction of time and thus the momentum and angular momentum of the particle.

In weak interactions, P and C were found to be fully violated symmetries but CP and T symmetries seemed to hold. However, J. H. Christenson, V.L.Fitch, J.W.Cronin, and R. Turlay discovered the violation of the CP symmetry in Neutral Kaon System in 1964.[1]. Since the discovery of CP violation, the origin of the CP violation has been discussed. The Standard Model which has been successful in high energy physics up to present, can accommodate the CP violating phenomena to the theory, also.

### 1.1 CP Violation in Standard Model

#### 1.1.1 Standard Model

All matter consists of elementary particles, governed by four known interactions: the gravitational, the electromagnetic, the strong, and the weak. The Standard Model is a basic theory for the three interactions; electromagnetic, weak, and strong. In this model, these three interactions are caused by the exchange of gauge bosons. The elementary particles are three generations of quarks and leptons.

#### 1.1.2 CP violation

In Standard Model, CP violation can arise naturally in the interactions of the quarks with the charged gauge bosons,  $W^\pm$ . The charged current in weak

interaction has the form

$$g[\bar{u}_j V_{ji} \gamma_\mu (1 - \gamma_5) d_i W^\mu + h.c.], \quad (1.1)$$

where  $u_j = (u, c, t)$  are up-type quarks and  $d_i = (d, s, b)$  are down type quarks.  $V$  is the  $3 \times 3$  unitary CKM(Cabibbo-Kobayashi-Maskawa) matrix which connects up-type quarks with down-type quarks:

$$V = \begin{pmatrix} V_{ud} & V_{us} & V_{ub} \\ V_{cd} & V_{cs} & V_{cb} \\ V_{td} & V_{ts} & V_{tb} \end{pmatrix}$$

A convenient parameterization of  $V$  was introduced by Maiani[2]:

$$V = \begin{pmatrix} c_1 c_2 & s_1 c_2 & s_2 e^{-i\delta} \\ -s_1 c_3 - c_1 s_2 s_3 e^{-i\delta} & c_1 c_3 - s_1 s_2 s_3 e^{i\delta} & c_2 s_3 \\ s_1 s_3 - c_1 s_2 c_3 e^{-i\delta} & -c_1 s_3 - s_1 s_2 c_3 e^{i\delta} & c_2 c_3 \end{pmatrix} \\ (c_i = \cos\theta_i, s_i = \sin\theta_i).$$

The matrix elements of  $V$  express the coupling strength at vertex of  $W$  and up-type and down-type quarks as shown in Equation 1.1. Therefore, experimental data on strange particle and B meson decay rates can determine the magnitudes of  $V_{us}$ ,  $V_{cb}$ , and  $V_{ub}$ . These magnitudes show that the mixing angles have a hierarchical structure. Wolfenstein[3] introduced a conventional parameterization of the CKM matrix by expanding in powers of  $\lambda = \sin\theta_{12}$ . To order  $\lambda^3$ , the matrix becomes

$$V = \begin{pmatrix} 1 - \frac{\lambda^2}{2} & \lambda & A\lambda^3(\rho - i\eta) \\ -\lambda & 1 - \frac{\lambda^2}{2} & A\lambda^2 \\ A\lambda^3(1 - \rho - i\eta) & -A\lambda^2 & 1 \end{pmatrix}, \quad (1.2)$$

where there are four parameters  $\lambda$ ,  $A$ ,  $\rho$ , and  $\eta$  that have to be obtained from experiments. They are determined to be  $A = 0.81 \pm 0.04$ ,  $\lambda = 0.221 \pm 0.002$ , and  $(\rho^2 + \eta^2)^{\frac{1}{2}} = 0.36 \pm 0.09$ [4].  $\rho$  and  $\eta$  have large uncertainties though the  $\lambda$  and  $A$  are well measured.

If all the matrix elements are made to be real, the Lagrangian is CP invariant. However, the matrix element containing three generations cannot eliminate  $\eta$ , and all CP violation in this model depends on  $\eta$ . In the next section, we will describe how the Standard Model explains the CP violating phenomena in neutral kaon system.

### 1.1.3 CP violation in Neutral Kaon system

#### Neutral Kaon System

$K^0(d\bar{s})$  and  $\bar{K}^0(\bar{d}s)$  mesons are strangeness eigenstates. The  $K^0$  and  $\bar{K}^0$  are CP conjugate states to each other:

$$CP | K^0 \rangle = | \bar{K}^0 \rangle \\ CP | \bar{K}^0 \rangle = | K^0 \rangle .$$

Let us define CP eigenstate to discuss CP violation. The  $K_1$  and  $K_2$  as shown below which are linear combinations of  $K^0$  and  $\bar{K}^0$ , are eigenstates of the CP transformation.

$$K_1 = \frac{1}{\sqrt{2}}(K^0 + \bar{K}^0) \quad CP |K_1\rangle = + |K_1\rangle \quad (1.3)$$

$$K_2 = \frac{1}{\sqrt{2}}(K^0 - \bar{K}^0) \quad CP |K_2\rangle = - |K_2\rangle. \quad (1.4)$$

Before the discovery of CP violation, the long lived neutral kaon( $K_L$ ) was assumed to be identical to  $K_2$ . Cronin et al. discovered  $K_L$  (“ $CP = -1$ ”)  $\rightarrow \pi^+\pi^-$  (“ $CP = +1$ ”) decay with its branching ratio  $\sim O(10^{-3})$ .

Standard Model has the following two mechanisms to introduce CP violation in neutral kaon system.

- Indirect CP violation

There is a small admixture of “ $CP = +1$ ” state,  $K_1$ , in the  $K_L$  state.

- Direct CP violation

The  $K_2$ ( $CP = -1$ ) directly decays to “ $CP = +1$ ” state.

Standard Model explains both CP violating phenomena by the imaginary phase in CKM matrix.

### Indirect CP Violation

Indirect CP violation arises from box diagrams as shown in Figure 1.1. These diagrams provide  $K^0 - \bar{K}^0$  mixing and their amplitudes include  $V_{td}$  component. Thus, the mixing is asymmetric and causes CP violation.

This mixing can introduce small contamination( $\epsilon$ ) of  $K_1$ ( $CP = +1$ ) in the  $K_L$  state dominated by  $K_2$ ( $CP = -1$ ), as:

$$\begin{aligned} |K_L\rangle &= \frac{1}{\sqrt{1+\epsilon^2}}(|K_2\rangle + \epsilon|K_1\rangle) \\ &= \frac{1}{\sqrt{2(1+\epsilon^2)}}((1+\epsilon)|K^0\rangle - (1-\epsilon)|\bar{K}^0\rangle). \end{aligned}$$

This equation implies that the state  $K_L$  consists of asymmetric mixture of the  $K^0$  and  $\bar{K}^0$ . The  $K^0$  can decay to  $\pi^-l^+\nu_l$  and  $\bar{K}^0$  can decay to  $\pi^+l^-\bar{\nu}_l$ . Therefore, we can measure the asymmetric mixture of  $K^0$  and  $\bar{K}^0$  in  $K_L$  by measuring the charge asymmetry in  $K_L \rightarrow \pi e \nu$ :

$$\begin{aligned} \delta_l &= \frac{\Gamma(\pi^-l^+\nu_l) - \Gamma(\pi^+l^-\bar{\nu}_l)}{\Gamma(\pi^-l^+\nu_l) + \Gamma(\pi^+l^-\bar{\nu}_l)} = (0.327 \pm 0.012) \times 10^{-2} [5, 6] \\ &\sim 2Re(\epsilon), \end{aligned}$$

where  $\Gamma$  is the partial decay width for the final state. This measurement confirmed the existence of indirect CP violation and the measured  $\epsilon$  is consistent with  $Br(K_L \rightarrow \pi^+\pi^-)$ .

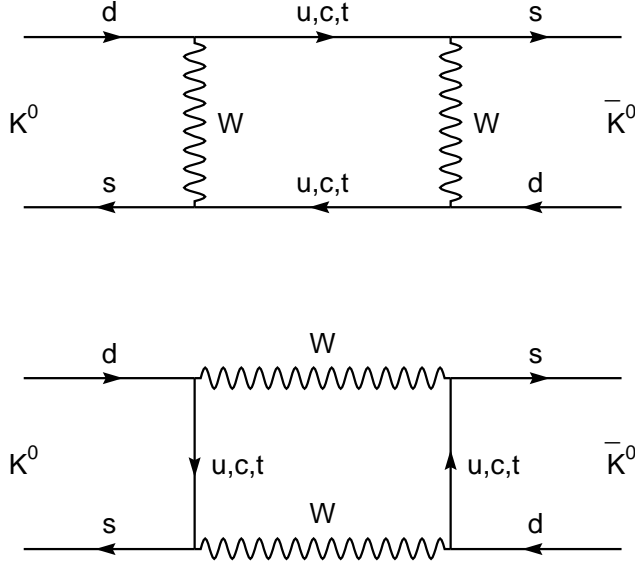


Figure 1.1: The box diagrams which are expected to provide the dominant contribution to  $K^0$ - $\bar{K}^0$  mixing.

## Direct CP Violation

Standard Model also predicts direct CP violation where CP is violated in the decay itself.

Over the past decades, a considerable number of experiments have searched for direct CP violation. Direct CP violation in  $K_L \rightarrow \pi\pi$  arises from the  $V_{td}$  component in the penguin diagram shown in Figure 1.2.

The direct CP violation has been searched for by measuring the  $Re(\epsilon'/\epsilon)$  where  $\epsilon$  means the size of the indirect CP violation, and  $\epsilon'$  means the size of the direct CP violation. The contributions from the penguin diagram were different between the final states:  $\pi^0\pi^0$ , and  $\pi^+\pi^-$ . Therefore,  $Re(\epsilon'/\epsilon)$  can be measured by taking double ratio between four decay modes as:

$$R \equiv \frac{\Gamma(K_L \rightarrow \pi^+\pi^-)/\Gamma(K_S \rightarrow \pi^+\pi^-)}{\Gamma(K_L \rightarrow \pi^0\pi^0)/\Gamma(K_S \rightarrow \pi^0\pi^0)} \simeq 1 + 6Re(\epsilon'/\epsilon).$$

If the measurement of  $Re(\epsilon'/\epsilon)$  is confirmed to be non-zero, then it will be an evidence for the direct CP violation. The most recent results are from two experiments,

**Fermilab E731**  $Re(\epsilon'/\epsilon) = (7.4 \pm 5.2(stat) \pm 2.9(sys)) \times 10^{-4}$ [7],

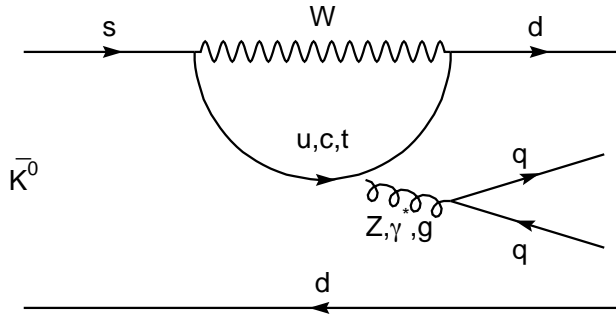


Figure 1.2: The penguin diagram which is expected to provide the direct CP violation.

**CERN NA31**  $Re(\epsilon'/\epsilon) = (23 \pm 3.6(stat) \pm 5.4(sys)) \times 10^{-4}$ [8].

The result from E731 is consistent with zero. On the other hand, the result from NA31 is  $3\sigma$  away from zero. Since these results disagree, there is no conclusion for the direct CP violation. E832 at Fermilab and NA48 at CERN are expected to measure  $Re(\epsilon'/\epsilon)$  with an accuracy of  $(1 \sim 2) \times 10^{-4}$ . The question of whether or not the  $K_2$  can decay into the two-pion final state has yet to be answered.

According to Standard Model, there is another probe to observe the direct CP violating phenomena in neutral kaon system, such as  $K_L \rightarrow \pi^0 l^+ l^-$  ( $l=e, \mu, \nu$ ). In  $K_L \rightarrow \pi\pi$  decays, the decay amplitudes are dominated by tree level diagrams. On the other hand, in  $K_L \rightarrow \pi^0 l^+ l^-$  modes, there is no contribution from tree level diagram which are CP conserving, so they can be a good probe to the direct CP violation. The Standard Model predictions of the branching ratio of these decays are  $O(10^{-12}) \sim O(10^{-11})$ . Current experimental limits of these CP-violating decays are

- $Br(K_L \rightarrow \pi^0 e^+ e^-) < 4.3 \times 10^{-9}$  (90% C.L.)[9]
- $Br(K_L \rightarrow \pi^0 \mu^+ \mu^-) < 5.1 \times 10^{-9}$  (90% C.L.)[10]
- $Br(K_L \rightarrow \pi^0 \nu \bar{\nu}) < 1.6 \times 10^{-6}$  (90% C.L.)[11]

Among the three modes,  $K_L \rightarrow \pi^0 \nu \bar{\nu}$  offers the most direct test of the Standard Model, since it does not occur without direct CP violation. However, it is far more difficult compare to the others. E799-II experiment is primarily designed to detect  $K_L \rightarrow \pi^0 e^+ e^-$ . Here, we will concentrate on the  $K_L \rightarrow \pi^0 \mu^+ \mu^-$  decay in this thesis. In considering two charged decay modes, there are two different features between them. One is the size of the CP conserving process. The CP conserving process in  $K_L \rightarrow \pi^0 e^+ e^-$  is helicity suppressed, while that in  $K_L \rightarrow \pi^0 \mu^+ \mu^-$  is allowed because of heavy  $\mu$  mass.

Another is the size of their dangerous background decay. Both  $K_L \rightarrow \pi^0 l^+ l^-$  ( $l=e, \mu$ ) decays have dangerous background decays,  $K_L \rightarrow ll\gamma\gamma$  ( $l=e, \mu$ ), which have the same final state particles as the signal. Although the branching ratio of  $K_L \rightarrow \pi^0 \mu^+ \mu^-$  is expected to be about a factor of 5 lower than that of  $K_L \rightarrow \pi^0 e^+ e^-$  because of their phase space[13], the branching ratio of  $K_L \rightarrow \mu^+ \mu^- \gamma\gamma$  is more than 10 times lower than that of  $K_L \rightarrow e^+ e^- \gamma\gamma$ . Therefore, the level of background due to  $K_L \rightarrow ll\gamma\gamma$  in  $K_L \rightarrow \pi^0 \mu^+ \mu^-$  search is expected to be lower than that in  $K_L \rightarrow \pi^0 e^+ e^-$ .

## 1.2 $K_L \rightarrow \pi^0 \mu^+ \mu^-$

In this section, we will describe more details about  $K_L \rightarrow \pi^0 \mu^+ \mu^-$ . This decay has the direct CP violating contribution and some other contributions.

### 1.2.1 Direct CP Violating Contribution

Direct CP violating contribution makes  $K_2$  which is  $CP = -1$  decay to  $\pi^0 \mu^+ \mu^-$  which is  $CP = +1$ . There are two diagrams which contribute to the direct CP violation, as illustrated in Figure 1.3. The s quark emits a W boson, and becomes an up-type quark, and then couples again with a W boson to become a d quark. The direct CP violating contribution from the diagrams come from the top quark loop. Since  $K_2$  is defined as Equation 1.4, the decay amplitude of this contribution is proportional to the difference between  $K^0$  and  $\bar{K}^0$  decay amplitudes:

$$\begin{aligned} A(K_2 \rightarrow \pi^0 \mu^+ \mu^-) &\propto A(K^0 \rightarrow \pi^0 \mu^+ \mu^-) - A(\bar{K}^0 \rightarrow \pi^0 \mu^+ \mu^-) \\ &\propto V_{td} V_{ts}^* - V_{td}^* V_{ts} \\ &\propto \text{Im}(V_{td}), \end{aligned}$$

where A is the decay amplitude. Therefore, the amplitude of this contribution is proportional to the imaginary part of  $V_{td}$ . Thus, direct CP violation can arise from the diagrams.

There are no prediction for the  $\text{Br}(K_L \rightarrow \pi^0 \mu^+ \mu^-)$ . However, pure phase space argument suggests[13] the  $\text{Br}(K_L \rightarrow \pi^0 \mu^+ \mu^-)/\text{Br}(K_L \rightarrow \pi^0 e^+ e^-) \simeq 0.2$ , so we can obtain  $\text{Br}(K_L \rightarrow \pi^0 \mu^+ \mu^-)$  by using the prediction for  $\text{Br}(K_L \rightarrow \pi^0 e^+ e^-)$ . An approximate expression for the expected rate of direct CP violating  $\text{Br}(K_L \rightarrow \pi^0 e^+ e^-)$ , is found in reference[12]:

$$\text{Br}(K_L \rightarrow \pi^0 e^+ e^-)_{\text{direct}} = 0.32 \times 10^{-10} \eta^2 A^4 I(m_t) \quad (1.5)$$

$$I(m_t) \simeq 0.73 \left( \frac{m_t^2}{m_W^2} \right)^{1.18}, \quad (1.6)$$

where  $m_t$  and  $m_W$  are the mass of the top quark and W boson. By putting the values( $A, \eta, m_t$ , and  $m_W$ ) from Particle Data Group[4], the size of this contribution to the branching ratio is expected to be  $8.2 \times 10^{-13} \sim 5.5 \times 10^{-12}$ .

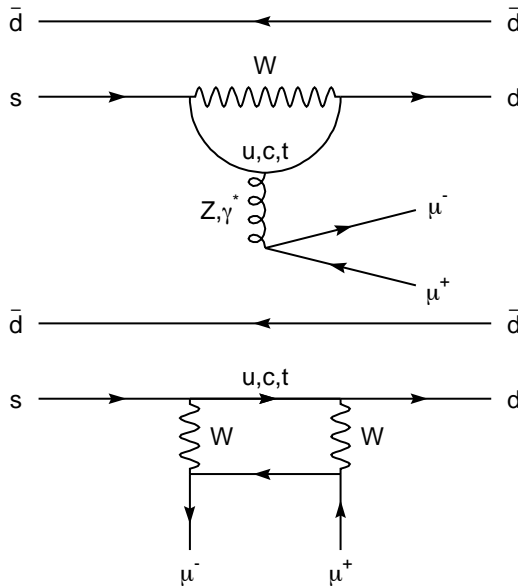


Figure 1.3: The direct CP violation. The upper figure is an electroweak penguin diagram. The lower figure is called W box diagram.

## 1.2.2 Other Contribution

As backgrounds to the direct CP violating  $K_L \rightarrow \pi^0 \mu^+ \mu^-$ , there are contributions from indirect CP violation, CP conserving decay, and  $K_L \rightarrow \mu^+ \mu^- \gamma \gamma$  in Standard Model. There are also theories which predict additional contributions to the decay.

### Indirect CP Violating Contribution

Indirect CP violating contribution comes from the small mixture of  $K_1$  in  $K_L$ , which decays  $K_1 \rightarrow \pi^0 \mu^+ \mu^-$ . The  $K_1 \rightarrow \pi^0 \gamma^* \rightarrow \pi^0 \mu^+ \mu^-$  decay itself is CP allowed.

The branching ratio of this contribution can be calculated from  $K_S \rightarrow \pi^0 \mu^+ \mu^-$  by

$$Br(K_L \rightarrow \pi^0 \mu^+ \mu^-)_{indirect} = |\epsilon|^2 \frac{\tau_{K_L}}{\tau_{K_S}} Br(K_S \rightarrow \pi^0 \mu^+ \mu^-). \quad (1.7)$$

There are no measurements of  $Br(K_S \rightarrow \pi^0 \mu^+ \mu^-)$ , so far.

However,  $K^+ \rightarrow \pi^+ \mu^+ \mu^-$  has been recently measured at BNL to be,

$$Br(K^+ \rightarrow \pi^+ \mu^+ \mu^-) = (5.0 \pm 1.0) \times 10^{-8} [14].$$

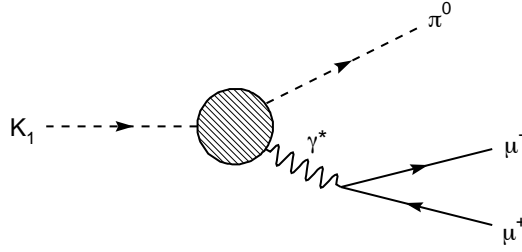


Figure 1.4: The diagram of the indirect CP violation

This measurement defines a parameter in Chiral Perturbation theory which is used to predict  $K_S \rightarrow \pi^0 \mu^+ \mu^-$ . As a result, one finds

$$Br(K_S \rightarrow \pi^0 \mu^+ \mu^-) = 6.39 \times 10^{-11}.$$

By using Equation 1.7, we can predict

$$Br(K_L \rightarrow \pi^0 \mu^+ \mu^-)_{indirect} = 1.95 \times 10^{-13}.$$

The size of this contribution is the same or smaller than that for the direct CP violating contribution.

### CP Conserving Contribution

There is also a CP conserving contribution from  $K_2 \rightarrow \pi^0 \gamma \gamma$  through the intermediate state as illustrated in Figure 1.5.

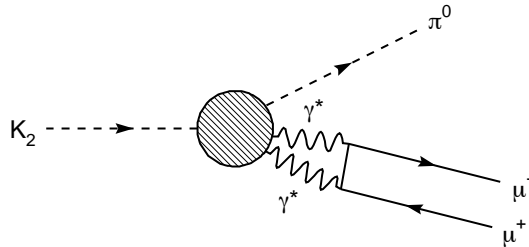


Figure 1.5: CP-conserving contribution

The  $K_L \rightarrow \pi^0 \gamma \gamma$  has been observed in experiments. The observations of  $K_L \rightarrow \pi^0 \gamma \gamma$  are consistent with Chiral Perturbation Theory( $\chi$ PT)[15] calculations. It predicted a branching ratio of  $K_L \rightarrow \pi^0 \mu^+ \mu^-$  for CP conserving contribution,

$$\begin{aligned}
B(K_L \rightarrow \pi^0 \mu^+ \mu^-)_{CP\text{-conserving}} &= 4.4 \times 10^{-13} [16] \\
&= 5 \sim 10 \times 10^{-12} [17].
\end{aligned}$$

### $K_L \rightarrow \mu^+ \mu^- \gamma \gamma$

$K_L \rightarrow \mu^+ \mu^- \gamma \gamma$  could be a serious background to  $K_L \rightarrow \pi^0 \mu^+ \mu^-$  searches.  $K_L \rightarrow \mu^+ \mu^- \gamma \gamma$  is  $K_L \rightarrow \mu^+ \mu^- \gamma$  with an internal bremsstrahlung photon. The decay products are exactly the same as  $K_L \rightarrow \pi^0 \mu^+ \mu^-$ . The only handles to reject this decay are the invariant mass of the 2 photons and kinematic distributions.

There are no measurements for  $K_L \rightarrow \mu^+ \mu^- \gamma \gamma$ , so far. Therefore, we measured  $K_L \rightarrow \mu^+ \mu^- \gamma \gamma$  as described in Appendix A, and used it to estimate the background contribution to  $K_L \rightarrow \pi^0 \mu^+ \mu^-$  process.

### 1.2.3 $K_L \rightarrow \pi^0 \mu^+ \mu^-$ in Other Theories

Standard Model can explain CP violation without new particle or new interaction. However, there are some theories which explain CP-violating phenomena with some possible new mechanisms. This section will describe such theories.

#### Superweak Theory

Wolfenstein[18] introduced Superweak Theory in 1964 to explain indirect CP violation. The theory postulates a  $\Delta S = 2$  interaction which produce  $K^0 \leftrightarrow \bar{K}^0$ . Because  $K_L$  and  $K_S$  are closely equal in mass, the superweak coupling only has to be of order  $10^{-10}$  of the normal weak coupling. In this case, the chance of observing CP violation in any other system is essentially zero.

#### Leptoquark Model

Leptoquark model assumes that there is a leptoquark which couples to a quark and a lepton pair. There are two types of models which are introduced by L. Hall and L.Randall[19]. One model assumes that the leptoquark couples to only a single helicity of quark and lepton. A coupling of the form  $\lambda_{ij} \bar{Q}_i \phi_l^c$  where  $\lambda$  is leptoquark's Yukawa coupling matrix,  $Q$  is a quark doublet, and  $l$  is a lepton singlet. This coupling explains CP violation, and causes the  $K_L \rightarrow \pi^0 l^+ l^-$  decay, where the predicted branching ratio is:

$$\begin{aligned}
B(K_L \rightarrow \pi^0 \mu^+ \mu^-) &= 5 \times 10^{10} \frac{(Im(\lambda_{12} \lambda_{22}^*))^2}{M_G^4} GeV^4 \\
\frac{(Im(\lambda_{12} \lambda_{22}^*))^2}{M_G^2} &\simeq 5 \times 10^{-12} GeV^{-2},
\end{aligned}$$

where  $M_G$  is the mass of the leptoquark. The allowed value of  $M_G$  in the model is  $100 \sim 10^6 GeV/c^2$ . The expected branching ratio is  $2.5 \times 10^{-5} \sim 2.5 \times 10^{-13}$

contribution	Branching fraction	
CP conserving	$4.4 \times 10^{-12}$	[16]
	$5 \sim 10 \times 10^{-12}$	[17]
CP violating (direct+indirect)	$0.4 \sim 13 \times 10^{-12}$	[16]
	$3.1 \sim 31 \times 10^{-13}$	[17]
all contributions	$5.4 \sim 10.2 \times 10^{-12}$	[21]

Table 1.1: Theoretical prediction for each contribution

Another model assumes that there are two leptoquarks with different U(1) charges, so that quarks and leptons can couple to one of the two types of leptoquarks. When the SU(2) is broken, the two leptoquarks will mix. Because of scalar-scalar type interaction, the  $K_L \rightarrow \pi^0 \mu^+ \mu^-$  can proceed without CP violation.

### Supersymmetric Model

Supersymmetric model was based on a generic low-energy supersymmetric extension of the Standard Model. There are additional contributions to the  $K_L \rightarrow \pi^0 l^+ l^-$  because of additional box diagrams or penguin diagrams in which supersymmetric partners are exchanged. This model provides an additional contribution for the  $K_L \rightarrow \pi^0 l^+ l^-$ . According to this model, Isidori et al.[20] calculated,

$$Br(K_L \rightarrow \pi^0 e^+ e^-) = 1 \sim 6 \times 10^{-10}.$$

Pure phase space argument suggests[13] the  $Br(K_L \rightarrow \pi^0 \mu^+ \mu^-)/Br(K_L \rightarrow \pi^0 e^+ e^-) \simeq 0.2$ . Then,

$$Br(K_L \rightarrow \pi^0 \mu^+ \mu^-) \approx 2 \sim 12 \times 10^{-11}. \quad (1.8)$$

### 1.2.4 Theoretical Predictions Summary

The theoretical predictions by Standard Model are summarized in the table 1.1. The sum of all contributions(CP conserving + CP violating) for each prediction is  $0.5 \sim 1.7 \times 10^{-11}$ .

Superweak Model predicts that there is no direct CP violating contribution. On the other hand, the leptquark model and supersymmetric model predicted extra contributions in addition to the contributions by Standard Model.

## 1.3 Summary

According to the Standard Model, the decay of  $K_L \rightarrow \pi^0 \mu^+ \mu^-$  includes the direct CP violating contribution. The current upper limit is far from the theoretical predictions. The results are limited by statistics up to present. Therefore, we searched for this interesting decay  $K_L \rightarrow \pi^0 \mu^+ \mu^-$  with a better

sensitivity. The number of  $K_L$ 's and detector acceptance were largely increased compared to the previous searches.

$K_L \rightarrow \mu^+ \mu^- \gamma \gamma$  was supposed to exist and it is a dangerous background to  $K_L \rightarrow \pi^0 \mu^+ \mu^-$ , but there are no measurements of  $K_L \rightarrow \mu^+ \mu^- \gamma \gamma$ . We observed the  $K_L \rightarrow \mu^+ \mu^- \gamma \gamma$  decay for the first time, and its analysis is described in Appendix A. Therefore, we can predict the number of  $K_L \rightarrow \mu^+ \mu^- \gamma \gamma$  in the signal region.

A confirmation with a larger branching ratio would indicate the existence of a new physics beyond the Standard Model or outside every model so far considered. Thus, the experimental result in the search for  $K_L \rightarrow \pi^0 \mu^+ \mu^-$  has an impact on the selection of the right model used to describe the CP violating phenomena.

## 1.4 Overview

This thesis describes a search for  $K_L \rightarrow \pi^0 \mu^+ \mu^-$  that we carried out at Fermilab. The detector is described in Chapter 2. The Monte Carlo simulation for the analysis of  $K_L \rightarrow \pi^0 \mu^+ \mu^-$  is described in Chapter 3. Event selection is described in Chapter 4. Chapter 5 describes the estimated background events. Chapter 6 describes the uncertainty on the sensitivity for searching  $K_L \rightarrow \pi^0 \mu^+ \mu^-$ . Chapter 7 gives the result and the discussions. Finally, Chapter 8 will conclude this thesis.

# Chapter 2

## KTeV Experiment

### 2.1 KTeV Experiment

The KTeV experiment was designed for investigating CP violating phenomena in neutral kaon system. KTeV experiment consisted of two experiments: E832 and E799-II. E832 experiment was focused on the precise measurement of  $Re(\epsilon'/\epsilon)$  with an accuracy of  $10^{-4}$ . E799-II experiment was optimized for the  $K_L$  rare decay search, especially CP violating decays. The  $K_L \rightarrow \pi^0 \mu^+ \mu^-$  was searched for in E799-II experiment. The data taking of KTeV experiment was carried out from October 1996 to September 1997. During the period, E799-II experiment took data for total of 14 weeks. Table 2.1 shows the data taking periods. The following section will describe the technique and detector elements of this experiment.

Experiment	E832	E799-II	E832	E799-II
referred name	-	Winter Run	-	Summer Run
Begin	10/24/96	1/24/97	3/24/97	7/28/97
End	12/18/96	3/23/97	7/27/97	9/5/97

Table 2.1: The period of the experiments

#### 2.1.1 $K_L$ Beam

The neutral kaons were produced by a proton beam striking a target. Fermilab Tevatron delivered a 800 GeV/c primary proton beam to the target with a typical intensity of  $3.5(4.0) \times 10^{12}$  per 23 second spill during 60 seconds cycle in summer(winter) run. A spill consisted of  $10^9$  buckets with 53MHz Radio Frequency(RF) structure. The nominal targeting angle was set to be 4.2mrad in the vertical plane to obtain a good kaon to neutron ratio. The target was 30.5cm long BeO rod with the cross section of  $3.0 \times 3.0$  ( $mm^2$ ). The 800 GeV/c proton produced secondary kaons which have an energy spectrum as shown in Figure 2.1.

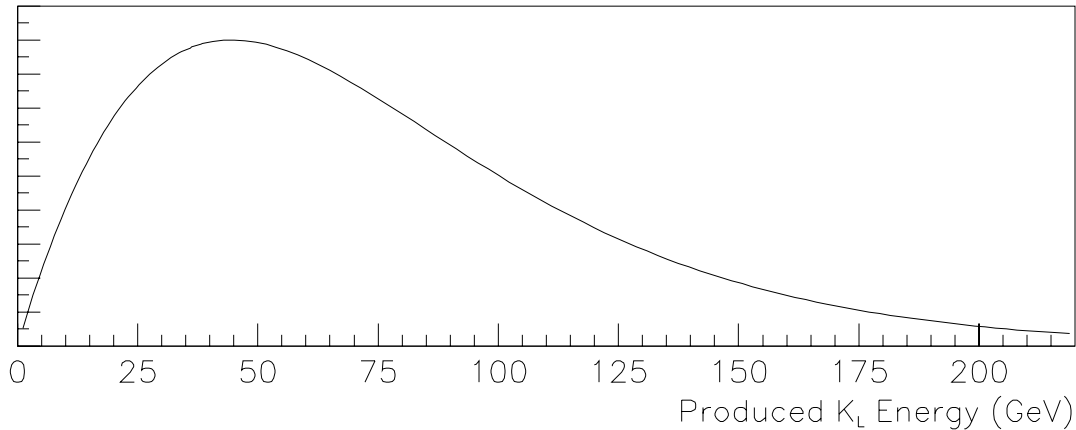


Figure 2.1: The energy spectrum of the kaon at the target

Two parallel neutral kaon beams were made by three iron collimators with two holes, and by magnets to sweep out charged particles. The position and specifications of the collimators are summarized in Table 2.2. The first two collimators made two beam streams. The defining collimator formed the beam shape. The solid angle of each beam was  $0.5 \text{ mrad} \times 0.5 \text{ mrad}$  for winter run,  $0.7 \text{ mrad} \times 0.7 \text{ mrad}$  for summer run.

name	Distance from target	Thickness	Hole size
primary collimator	20.3 m	1.0 m	1.09 cm
slab collimator	40.0 m	2.0 m	-
defining collimator(winter run)	86.3 m	2.6 m	4.4 cm
defining collimator(summer run)	86.3 m	2.6 m	5.2 cm

Table 2.2: The position and size of the collimator

The sweeping magnets were located at 2.5 m, 15 m, 24.8 m, and 89.3 m from the target. The first two magnets removed charged particles which were made by proton interaction at the target. The other magnets removed the charged particles which were made by the interaction of the secondary beam at the collimators.

A Pb absorber with the thickness of 7.5 cm was located at 18.5 m from the target in order to remove photons in the beam by converting them to electron-positron pairs to be swept away by the magnets.

For calibrating the detectors, we filtered out charged particles except for muons by putting two beamstops in the neutral beam. They were made of steel with 28.5 cm and 21.1 cm thickness and located at 46.4 m and 50.1 m from the target, respectively.

## 2.2 Detector

The detector region started at 90 m downstream of the target. Figure 2.2 is a schematic view of KTeV detector. Hereafter, the beam axis is referred to as z-axis, and  $Z=0$  is set to be the target position. The y-axis is defined to be vertical, with the positive y direction being up, and the x(horizontal) direction was defined such that the overall coordinate system was right-handed.

Each detector element will be described from upstream in the following sections.

### 2.2.1 Decay Region and Photon Veto Counter

The decay region started at 90 m downstream of the target and ended by the 1.8 m diameter vacuum window at 158.0 m. The decay region was evacuated to  $1.0 \times 10^{-6} \text{ torr}$  to minimize backgrounds due to interaction of the neutral beam with residual gas. The vacuum window was made by Kevlar and myler sandwich. The thickness of the vacuum window was estimated to be 0.0016 radiation lengths( $X_0$ ).

There were photon veto detectors in the decay region which were called Ring Counters(RC). The photon veto detectors which were located outside of the drift chambers 2-4 and CsI calorimeter were called Spectrometer Anti(SA)s and CsI Anti(CIA), respectively. The purpose of these detectors was to detect particles which escaped the CsI calorimeter. The location and dimensions of the photon veto counters are listed in Table 2.3.

One RC consisted of 16 wedge shape counters. Each wedge counter consisted of 24 layers of scintillator and lead sheet. For the first 16 layers, the lead sheets were  $0.5X_0$  thick each. For the rest of 8 layers, the lead sheet was  $1X_0$  each. The thickness of the scintillator was 2.5mm. The total radiation length of each wedge counter was  $16X_0$ . In case of SA and CIA, each counter consisted of 32 layers of scintillator(2.5mm thickness) and lead sheet( $0.5X_0$ ).

The photon veto counters were segmented as shown in Figure 2.3. In each segment of the photon veto counters, the scintillation light was collected by inserting wave length shift fibers in the scintillator and guided to a phototube.

### 2.2.2 Spectrometer

The KTeV spectrometer consisted of 4 sets of drift chambers and an analysing magnet. Its function was to measure the trajectories and momentum of the charged particles. The position and dimensions of the drift chambers and the magnet are summarized in Table 2.4.

#### Magnet

The analyzing magnet was located at 170.008m from the target. It generated a vertical field of about 2kGauss. The magnetic gap was  $2.9 \text{ m}(H) \times 2.0 \text{ m}(W) \times 3.1 \text{ m}(L)$ . The magnet gave a typical transverse momentum kick of  $205 \text{ MeV}/c$ .

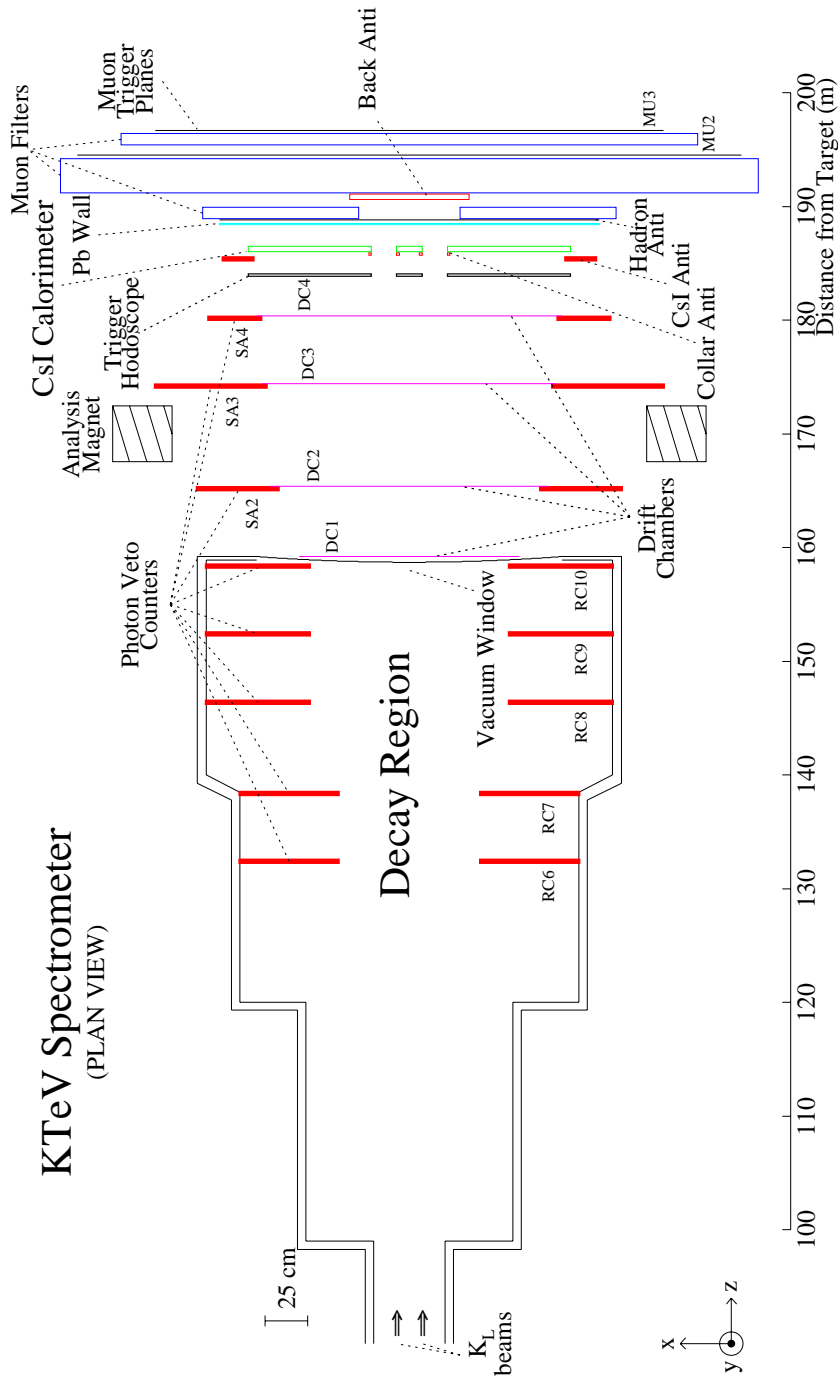


Figure 2.2: KTeV Spectrometer

name	distance from the target(m)	inner size(m×m)	outer size
RC 6	132.596	0.84 × 0.84	radius = 1.00 m
RC 7	138.598	0.84 × 0.84	radius = 1.00 m
RC 8	146.598	1.18 × 1.18	radius = 1.44 m
RC 9	152.600	1.18 × 1.18	radius = 1.44 m
RC 10	158.599	1.18 × 1.18	radius = 1.44 m
SA 2	165.166	1.540 × 1.366	2.500 m × 2.500 m
SA 3	173.985	1.692 × 1.600	3.000 m × 2.400 m
SA 4	180.018	1.754 × 1.754	2.372 m × 2.372 m
CIA	185.191	1.842 × 1.842	2.200 m × 2.200 m

Table 2.3: The position and the size of the photon veto detectors

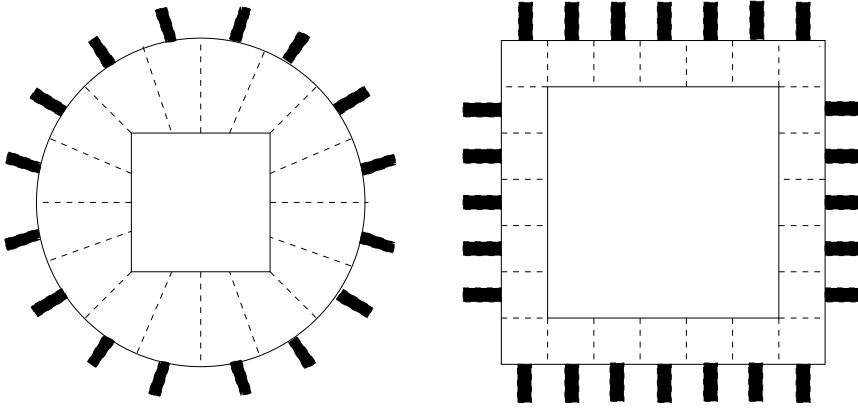


Figure 2.3: The photon veto detectors. The left figure shows a RC which was located inside the vacuum region. The right figure shows the SA and CIA.

## Drift Chamber

There were 4 sets of the drift chambers starting just downstream of the vacuum window. Each chamber had 4 planes of sense wires. Two planes were parallel to x direction, and the others were parallel to y direction as shown in Figure 2.4. The distance between sense wires in the same plane was 12.7mm. For each direction, the sense wire planes were offset by 6.35mm. The sense wire was surrounded by six field wires forming a hexagonal cell. The chamber gas consisted 49.75% of Argon, 49.75% of Ethane, and 0.5% isopropyl alcohol. The chambers were operated with the voltage of about -2500V.

The signals from sense wires were amplified with pre-amplifiers which were mounted on the chamber. The amplified signal was sent to an amplifier/discriminator card. The discriminated signal were sent to the TDC to measure the drift time.

Each chamber plane had a resolution of 100  $\mu\text{m}$ . The spectrometer's intrinsic momentum resolution was

$$(\sigma_p/p)^2 = (0.38\%)^2 + (0.016\% \times p(\text{GeV}/c))^2,$$

name	distance from the target	dimensions
DC 1	159.419 m	1.30 m $\times$ 1.30 m
DC 2	165.565 m	1.64 m $\times$ 1.44 m
Analysis Magnet	170.008 m	-
DC 3	174.589 m	1.74 m $\times$ 1.64 m
DC 4	180.486 m	1.90 m $\times$ 1.90 m

Table 2.4: The position and size of the drift chamber

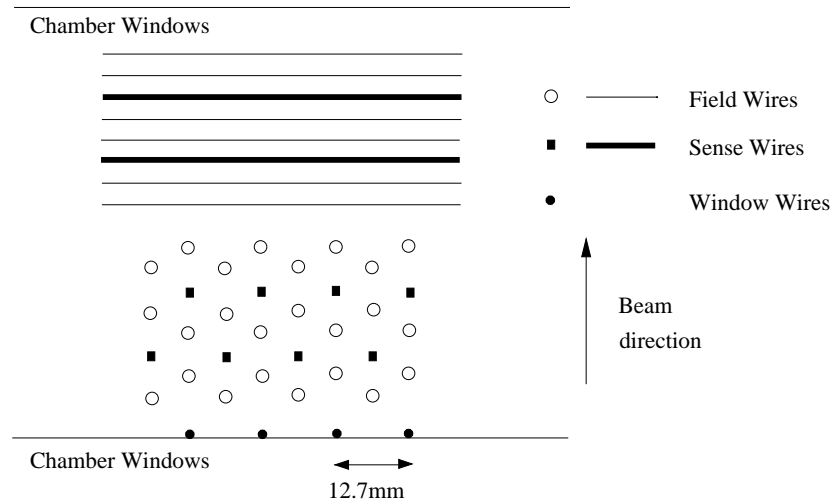


Figure 2.4: The sense and field wire geometry of the drift chamber. The field shaping wire formed a hexagonal cell with the sense wire located at the center.

where  $p$  is the momentum of a charged particle.

### 2.2.3 Trigger Hodoscopes

The main function of trigger hodoscopes was to identify events with two charged particles. The hodoscopes which were labeled 'V bank' and 'V' bank' were located at 183.903 m, 183.953 m from the target, respectively. These banks were made of 32 non-overlapping scintillator counters which have the length of 95 cm and the thickness of 0.5 cm, as shown in Figure 2.5. There were counters with three different widths: 7.8 cm, 11.87 cm, and 17.8 cm. Each scintillation counter was read out by a phototube whose output was routed to an ADC, TDC and the trigger logic.

### 2.2.4 Pure-CsI Electromagnetic Calorimeter

The main function of the CsI calorimeter was to determine the energy of incident photons over the range between 2 and 80 GeV, and the position of the photon and charged particles. The pure-CsI calorimeter was located at 186 m downstream from the target.

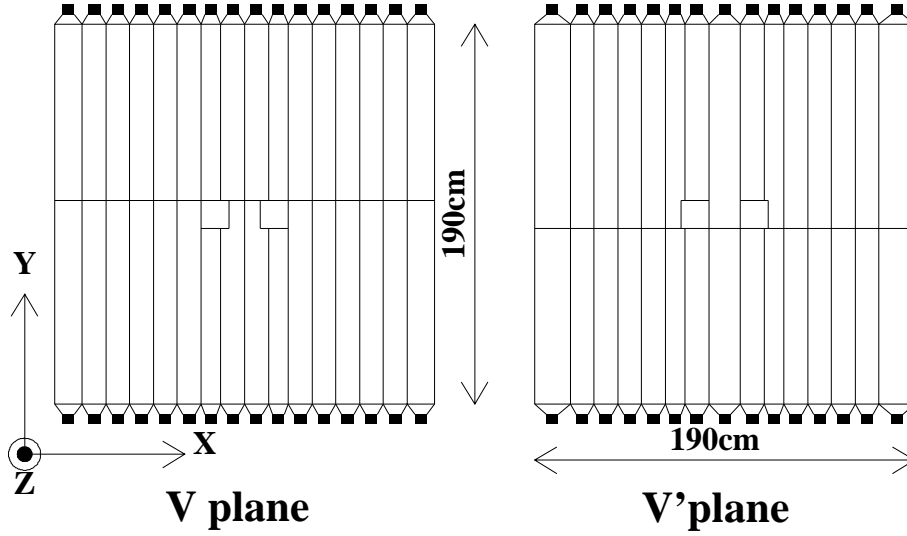


Figure 2.5: Schematic view of Trigger Hodoscopes(V, V' bank).

As shown in Figure 2.6, the energy resolution of this calorimeter was

$$\sigma_E/E = 0.6\% \oplus 0.6\%/\sqrt{E}(\text{GeV}). \quad (2.1)$$

Each part of this calorimeter is described in the next sections.

### Pure-CsI Crystal

This calorimeter consisted of 3100 pure CsI crystals. The length of the crystals was 50 cm(=27 Xo) which was optimized to get a good energy resolution. The overall size is 190 cm  $\times$  190 cm  $\times$  50 cm. There are two beam holes whose size was 15 cm  $\times$  15 cm and center positions were at  $x=\pm 15$ cm. A total of 2232 2.5 cm  $\times$  2.5 cm crystal are used for the inner section which covered 120 cm  $\times$  120 cm area. The outside area was covered by 868 blocks of 5 cm  $\times$  5 cm crystals. Each crystal was wrapped by 13  $\mu$ m thick mylar to contain scintillation light within individual crystal.

### Phototube

Phototubes were attached to the downstream face of each crystal to measure the scintillation light output. For the large crystals, 1.5 inch Hamamatsu R5330 phototubes were used. For the small crystals, 3/4 inch Hamamatsu R5364 phototubes were used. The nonlinearity of all the phototubes are within 0.5% with the gain of 5000 at the 15 mA output current which corresponds to  $10^6$  photoelectrons.

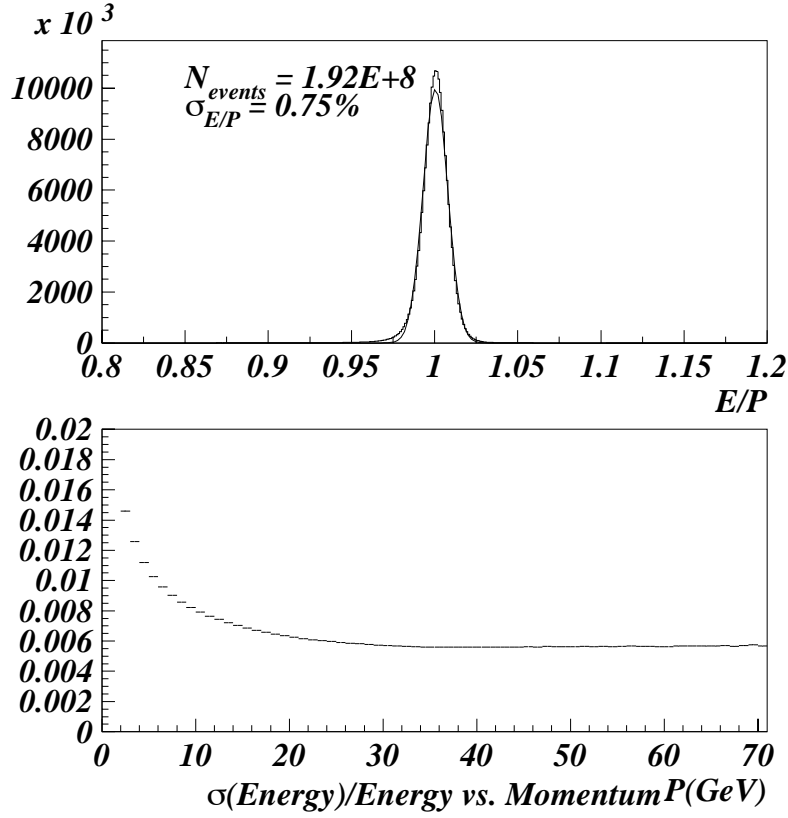


Figure 2.6: The upper plot shows the  $E/P$  distribution for electrons in  $K_L \rightarrow \pi e \nu$ , where  $E$  denotes an measured energy by the calorimeter, and  $P$  represents a measured momentum by the spectrometer. The lower plot shows the intrinsic energy resolution of the calorimeter as a function of electron momentum.

### Digital Photomultiplier Tube base

The main purposes of the Digital Photomultiplier Tube base(DPMT) were to achieve a wide dynamic range(a few MeV to 60 GeV) and to achieve the dead time free read out system. The DPMT was operated at 53 MHz corresponding to the accelerator RF(19 ns clock cycle) to obtain the time profile of energy deposit so that we can reject out of time accidental photons.

DPMT consisted of a high voltage divider and 3 chips: the charge-integrating and encoding chip(QIE), the flash-ADC(FADC) and the data buffer clocking(DBC) chip. The QIE chip divided the input current( $I$ ) into 9 binary weighted ranges( $I/2, I/4, I/8, \dots, I/512$ ). The input current is integrated onto 8 1pF capacitors (one for each range) which is then converted to a voltage. Only one capacitor voltage is transmitted to the FADC. FADC digitizes the signal of the input current for each clock cycle and DBC hold 32 clock cycles of the data.

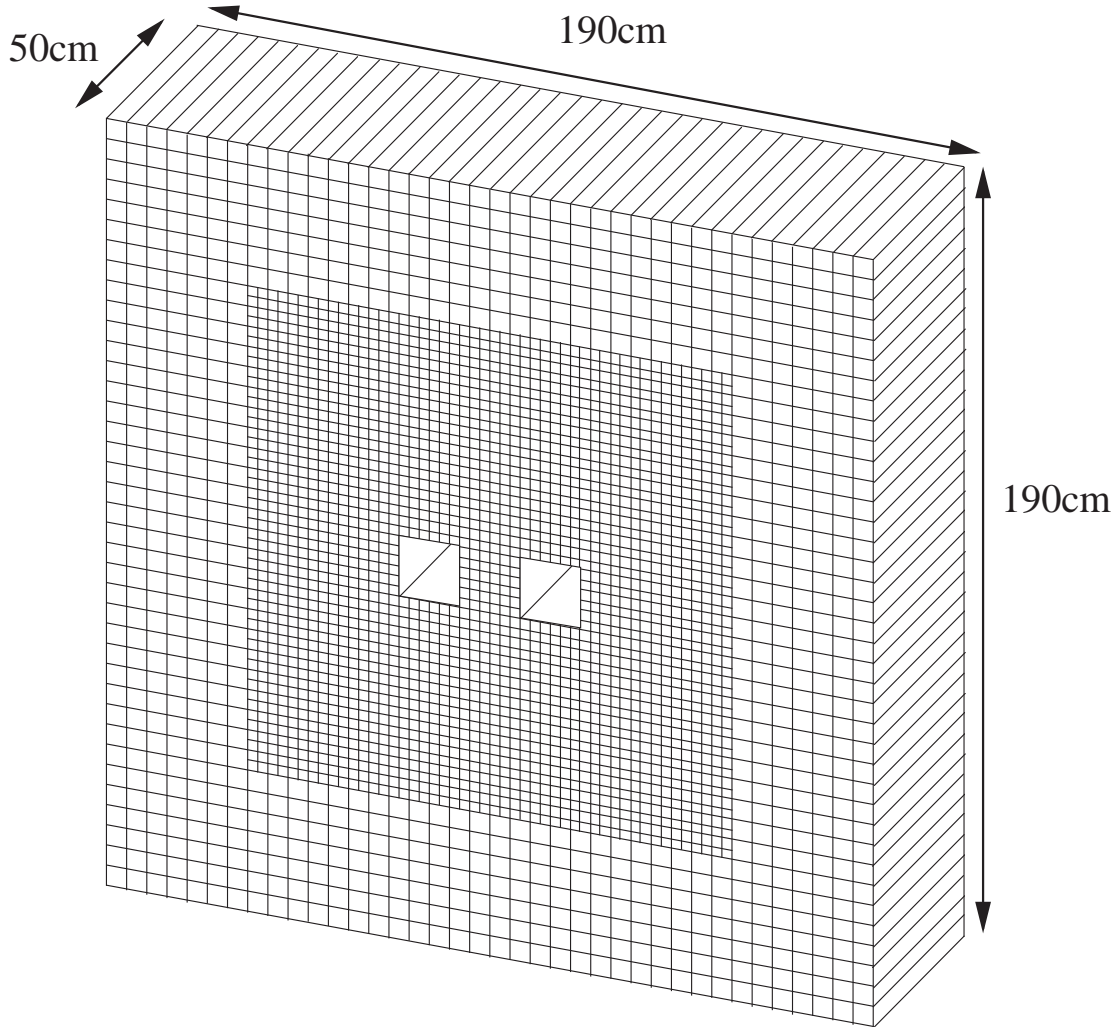


Figure 2.7: Pure-CsI Electromagnetic Calorimeter

### 2.2.5 Muon System

The purpose of the muon system is to identify muons among the charged particles. The muon system was located downstream of the CsI calorimeter. The muon system consisted of shields (Pb wall, three Iron shields) and three scintillation banks (MU2, MU3x, MU3y). The dimensions and positions of each element of the muon system are summarized in Table 2.5. All hadrons made hadron showers in the shields. Only muons with momentum above  $7\text{GeV}/c$  could pass the shields.

#### MU2 bank and MU3 banks

The MU2 bank was located at  $194.827\text{m}$  from the target, which was downstream of  $4\text{m}$  of iron. Its purpose was to veto muons. The bank consisted of 56  $150\text{cm} \times 15\text{cm} \times 1.5\text{cm}$  counters which overlapped by  $1\text{cm}$  with adjacent

name(Material)	distance from target	Thickness	cross section
Pb wall (Pb)	188.531 m	10.0 cm	2.43 m×2.43 m
MU1 filter (Fe)	189.092 m	104.2 cm	2.432 m×2.432 m
MU2 filter (Fe)	191.741 m	303.8 cm	4.26 m×3.4 m
MU3 filter (Fe)	195.287 m	102.5 cm	3.493 m×3.60 m
MU2	194.827 m	1.5	3.93×2.99
MU3y	196.362 m	1.5	3.00×3.00
MU3x	196.396 m	1.5	3.00×3.00

Table 2.5: The shields and banks in the Mu system

counters. MU3x and MU3y banks consisted of 40  $150\text{cm} \times 15\text{cm} \times 1.5\text{cm}$  counters and they were located at 196.362m and 196.396 m from the target, respectively. The counters in MU3 banks were not overlapped because the purpose of the MU3 banks was to count the number of muons. The distance between the last iron filter and the MU3 banks was minimized to 1cm to reduce fake hits due to  $\delta$ -rays. A phototube was mounted on each counter. The signal from the phototube was sent to ADC, TDC, and the trigger logic.

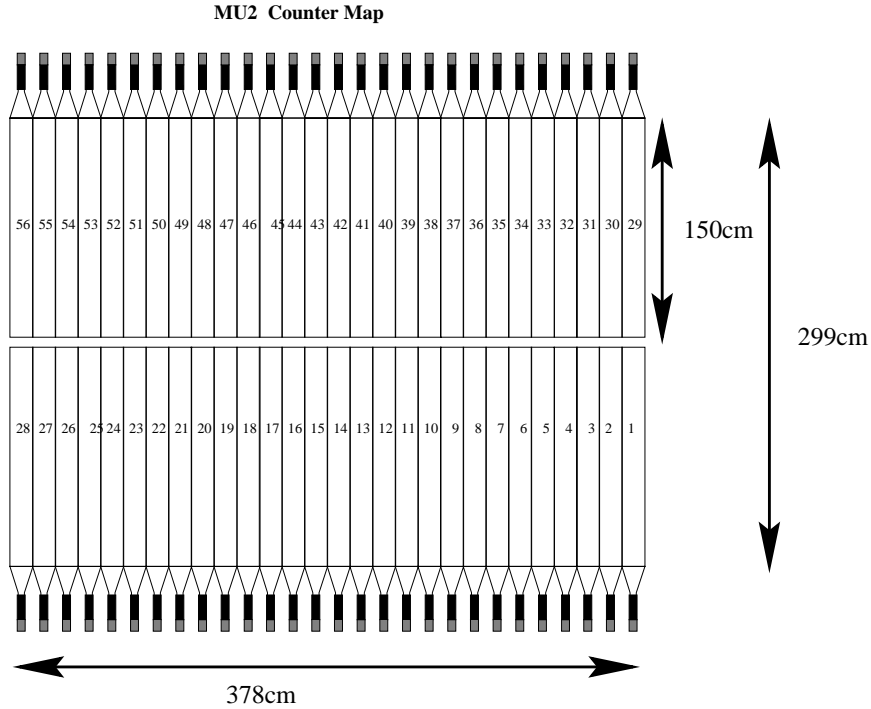


Figure 2.8: The MU2 bank.

Trigger Symbol	meaning
Level 1 trigger	
2V	at least 2 hits in one of the v(v') banks. The other bank have at least 1 hit.
DC12	1 or more hits in x view of drift chamber(DC) 1 and 2 or more hits in each x and y view of DC 2.
2MU3	at least 2 hits in one of the MU3 banks. The other bank have at least one hit.
<i>PHV</i>	No segments have more than 500 MeV in RC, and 400 MeV in SA and CIA.
Level 2 trigger	
2HCY	2 or more hits in every y view of drift chambers by Hit counting module.

Table 2.6: Summary of the Trigger condition Symbols

## 2.3 Trigger

The trigger system of KTeV experiment consisted of 3 stages. The first two stages consisted of NIM logic or electronic circuits. At the third stage of trigger, we used UNIX machines to reconstruct events and to apply cuts by software. Each stage of trigger is described in the following section.

### 2.3.1 Level 1 and Level 2 trigger

We used two types of triggers for  $K_L \rightarrow \pi^0 \mu^+ \mu^-$  analysis. One trigger is called “ $K_L \rightarrow \pi^0 \mu^+ \mu^-$  trigger” which is used for taking the events which have 2 muon-like charged tracks. Another trigger is called “ $K_L \rightarrow \pi^0 \pi^+ \pi^-$  trigger” which is for collecting events which have 2 tracks including  $K_L \rightarrow \pi^0 \pi^+ \pi^-$ .

The first level trigger(Level 1 trigger) was based only on information from the NIM logic. The information provided a decision every 19ns RF cycle with no dead time. Table 2.6 lists symbols and their meanings of the Level 1 trigger sources which were used for  $K_L \rightarrow \pi^0 \mu^+ \mu^-$  analysis.

Level 1 trigger generated ADC gates and TDC timing signals. At the same time, the Level 2 trigger processors started processing. The Level 2 trigger processors are described in the following subsections.

**HCC** Hardware Cluster counter(HCC) processor counts the number of the isolated groups of the crystals which have an energy deposit more than 1 GeV, with a pattern recognition processor. The counting process took 2  $\mu$ s.

**Hit Counting** This module counted the number of hits within 205ns of the event in y view of all the drift chambers. If there are adjacent two hits, we counted them as one hit.

The trigger condition for each trigger is listed below.

$$K_L \rightarrow \pi^0 \mu^+ \mu^- \text{ trigger: } 2V \cdot DC12 \cdot 2HCY \cdot 2MU3 \cdot \overline{PHV} \cdot HCC\_GE1$$

$$K_L \rightarrow \pi^0 \pi^+ \pi^- \text{ trigger: } 2V \cdot DC12 \cdot 2HCY$$

The trigger conditions, “ $2V \cdot DC12 \cdot 2HCY$ ” are common to both triggers, to require two track candidates. 2V means at least 2 hits in one of the v(v’) banks and the other bank have at least 1 hit. DC12 requires 1 or more hits in paddles of 16 sense wire in x view of drift chamber(DC) 1 and 2 or more hits in the paddles in each x and y view of DC 2. 2HCY requires 2 hits in each y plane of all DCs.  $K_L \rightarrow \pi^0 \mu^+ \mu^-$  trigger has additional conditions,  $2MU3 \cdot \overline{PHV} \cdot HCC\_GE1$  2MU3 represents 2 or more hits in each MU3 bank.  $\overline{PHV}$  requires that the energy deposit in each photon veto segment is less than 500 MeV in RC and less than 400 MeV in SA and CIA. HCC\_GE1 requires at least 1 HCC cluster.

### 2.3.2 Level 3 trigger and Data Acquisition System

Figure 2.10 shows the overall structure of the KTeV data acquisition system. The information of various detectors came in parallel through six data streams(as shown by vertical lines in Figure 2.10) to a matrix of buffer memories, and was written in the memories in the same plane. There were four planes(horizontal lines) in the system, of which three planes were used for Level 3 triggering and writing the events, and one plane was used for monitoring/calibration during the data taking. The total memory size was 4.6GBytes, large enough to store one spill (20sec) worth of events.

The Unix machines in different planes worked almost independently. The pieces of events in the same plane were read into the shared memory on the Unix machine. Each Unix machine had eight 200 MHz R4400 CPU’s, and they processed their own events in parallel.

As the Level 3 trigger, events were selected by the reconstructed information. The Level 3 requirement for the triggers are listed below.

- $K_L \rightarrow \pi^0 \mu^+ \mu^-$  trigger
  - 2 track candidates with a vertex
  - Each reconstructed track candidate points to an energy cluster
  - $1 < \text{The energy of the pointed energy cluster(GeV)} < 5$
- $K_L \rightarrow \pi^0 \pi^+ \pi^-$  trigger
  - 2 track candidates with a vertex

Only the events which satisfied the requirements, were written to DLT tapes. Every Unix machine had three DLT tape drives, and logged data in parallel.

## 2.4 Accidental Trigger

In order to put the accidental activity into Monte Carlo simulation, we overlaid the data taken by “accidental trigger” to the Monte Carlo events. The “accidental trigger” data was collected simultaneously with the  $K_L \rightarrow \pi^0 \mu^+ \mu^-$  data taking. The accidental trigger was designed to collect events which were uncorrelated with kaon decays, while the trigger rate was proportional to the incident proton flux at the target. The counter which consisted of three scintillation counters and Hamamatsu R1398 PMTs were placed at an angle of 90 degrees from the beam direction and at 1.8m from the target. The target was shielded with iron which have  $0.635\text{cm} \times 0.635\text{cm}$  hole. Coincidence of the three counters formed Accidental trigger.

## 2.5 Data Taking

### 2.5.1 Physics Run

As described in Section 2.1, the data taking of E799-II was carried out in two periods. The difference between winter and summer runs are summarized in Table 2.7.

	Winter Run	Summer Run
Run Number	8245-8913	10458-10970
Proton Beam Intensity(#proton/spill)	4.0E12	3.5E12
Beam size at the CsI calorimeter	10cm×10cm	12cm×12cm
$K_L \rightarrow \pi^0 \mu^+ \mu^-$ triggered Events	1.17E8	9.66E7
$K_L \rightarrow \pi^0 \pi^+ \pi^-$ triggered Events	2.29E8	1.54E8

Table 2.7: The condition difference of the periods.

The triggered events were written to about 500 DLT tapes (1/2 inch magnetic tape) where each tape can hold about 1.5 million events( about 12GB).

## 2.6 $K_L \rightarrow \pi^0 \mu^+ \mu^-$ Data Set

For the  $K_L \rightarrow \pi^0 \mu^+ \mu^-$  analysis, we made a data set which only contained the  $K_L \rightarrow \pi^0 \mu^+ \mu^-$  trigger events and  $K_L \rightarrow \pi^0 \pi^+ \pi^-$  trigger events.  $K_L \rightarrow \pi^0 \pi^+ \pi^-$  trigger events were prescaled because there are so many triggered events. The prescale factor for  $K_L \rightarrow \pi^0 \pi^+ \pi^-$  trigger events was 8166 for run8425-8913, and 7000 for other runs.

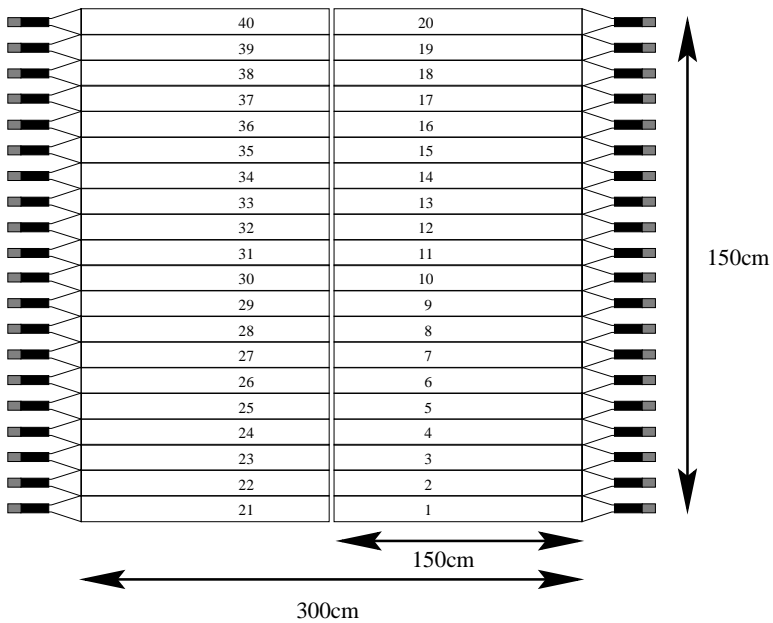
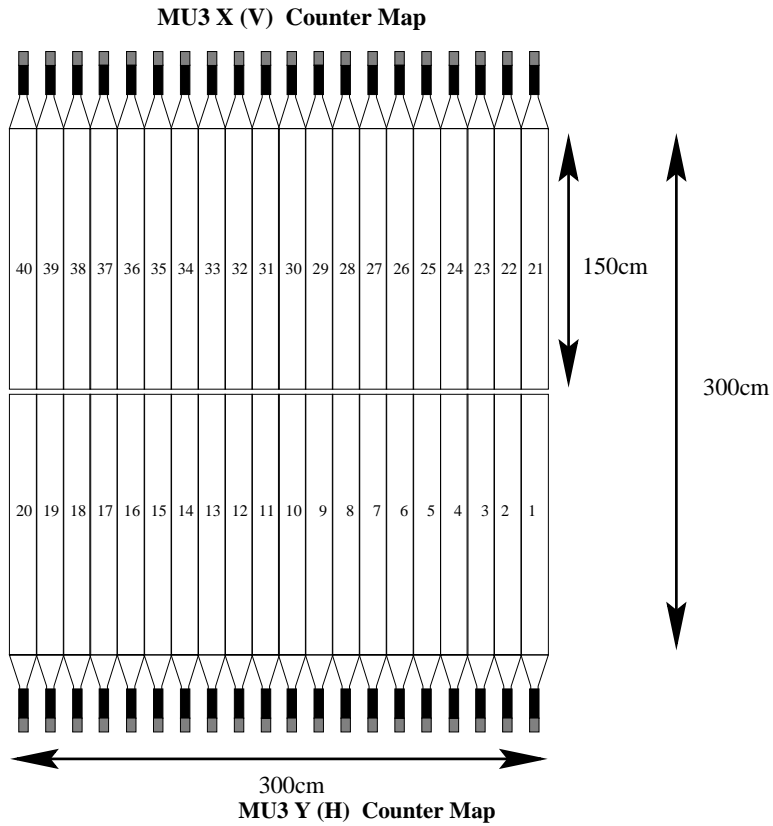


Figure 2.9: The upper figure shows MU3x bank. The lower figure illustrates MU3y bank.

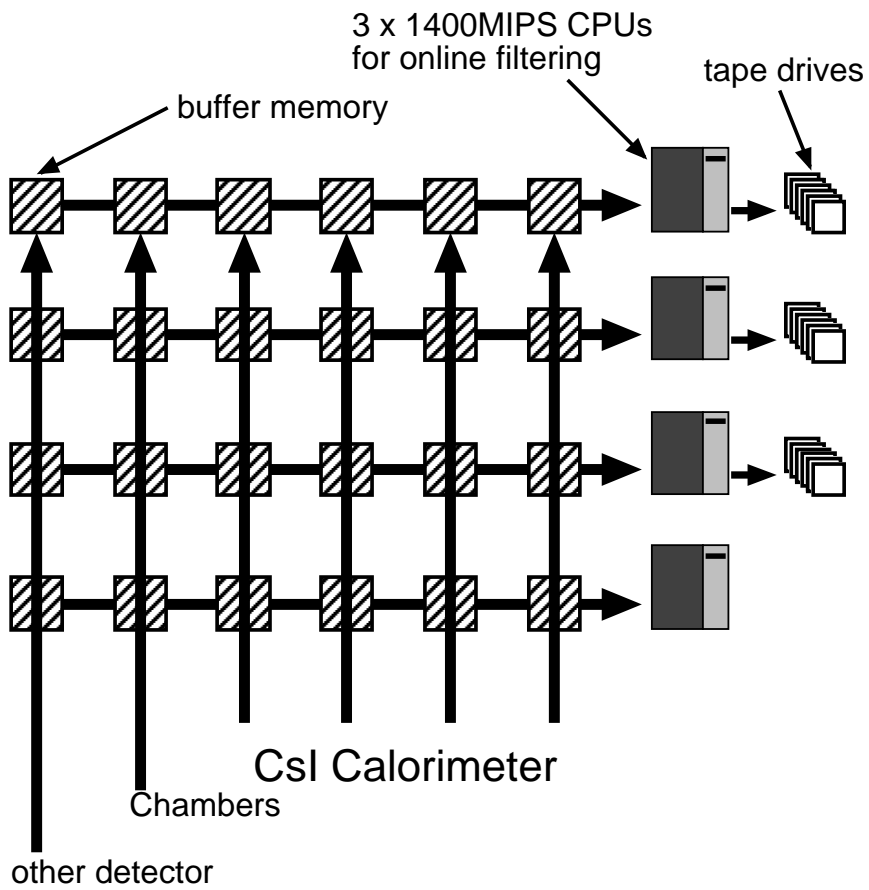


Figure 2.10: KTeV Data Acquisition System

# Chapter 3

## Monte Carlo Simulation

The main purpose of Monte Carlo simulation(MC) is to calculate the detector acceptances for  $K_L \rightarrow \pi^0 \mu^+ \mu^-$  and  $K_L \rightarrow \pi^0 \pi^+ \pi^-$ , needed for measuring the branching ratio. Another purposes of MC are to understand the characteristics of the background decays, to determine a set of cuts to select signal and reject background, and to estimate how many background events are expected in the signal region.

This chapter will describe how the KTeV Monte Carlo treated  $K_L$  beam production,  $K_L$  decay,  $\mu$  scattering,  $\mu$  misidentification, and the response of the detectors.

### 3.1 Production of $K_L$ Beam

The MC starts with the generation of neutral kaons according to the production spectrum. The spectrum has not been measured directly, so we instead utilized the Malensek parameterization[22] of the  $K^+$  and  $K^-$  production spectrum for protons incident on a beryllium target. In the parameterization, the number of kaons with momentum  $p$  into a solid angle  $d\Omega$  at a polar angle  $\theta$  was

$$\frac{d^2 N}{dp d\Omega} = \frac{B}{400} x \frac{(1-x)^A (1+5e^{-Dx})}{(1+p_t^2/M^2)^4} , \quad (3.1)$$

where,  $x$  denotes the ratio of the produced particle momentum( $p$ ) to the beam energy( $E_B$ ),  $x = p/E_B$ , and  $p_t$  represents the transverse momentum of the produced particle relative to the incident beam direction.  $B$ ,  $A$ ,  $D$ , and  $M^2$  were determined from the experimental data obtained by 400 GeV/c proton beam(Table 3.1). Both  $p$  and  $p_t$  have a unit of GeV/c.

If we define  $\sigma_{ud}$  as a production probability for a  $u\bar{u}$  or a  $d\bar{d}$  pair, and  $\sigma_s$  as that for an  $s\bar{s}$  pair,  $K^+$  production probability,  $\sigma(K^+)$ , would be proportional to  $2\sigma_s + \sigma_{ud}\sigma_s$  because the kaon could be produced by using either of the valence  $u$  quarks of the proton, or with a  $u$  quark from the sea. From the same arguments, we can get the following relation:

$$\sigma(K^+) \sim 2\sigma_s + \sigma_{ud}\sigma_s ,$$

	$A$	$B$	$M^2$	$D$
$K^+$	2.924	14.15	1.164	19.98
$K^-$	6.107	12.33	1.098	17.78

Table 3.1: The parameters used by Malensek [22].

$$\begin{aligned}
\sigma(K^-) &\sim \sigma_{ud}\sigma_s, \\
\sigma(K^0) &\sim \sigma_s + \sigma_{ud}\sigma_s = \frac{\sigma(K^+) + \sigma(K^-)}{2}, \\
\sigma(\bar{K}^0) &\sim \sigma_{ud}\sigma_s = \sigma(K^-).
\end{aligned}$$

Based on Equation 3.1 and the above relations between neutral kaons and charged kaons, we tentatively extracted the production probabilities for  $K^0$  and  $\bar{K}^0$ . In order to simulate correctly, the correction factor  $\xi(p)$  was obtained by measuring kaon momentum by  $K_L \rightarrow \pi^+\pi^-$  events in the real data. The measured correction factor,  $\xi(p)$  was:

$$\xi(p) = 1 + 1.0655x - 0.55337x^2 + 0.060033x^3, \quad (3.2)$$

where  $x = p / 100(\text{GeV}/c)$ , was multiplied to the generation probabilities as

$$\frac{d^2N}{dpd\Omega}(K^0) = \frac{1}{2} \left[ \frac{d^2N}{dpd\Omega}(K^+) + \frac{d^2N}{dpd\Omega}(K^-) \right] \times \xi(p), \quad (3.3)$$

$$\frac{d^2N}{dpd\Omega}(\bar{K}^0) = \frac{d^2N}{dpd\Omega}(K^-) \times \xi(p). \quad (3.4)$$

The kaon energy distribution produced with this correction is shown in Figure 2.1. Based on Equation 3.3, the MC produced  $K^0$ 's or  $\bar{K}^0$ 's at the target.\* The momentum of the decayed kaon was chosen between 20 GeV/c and 220 GeV/c. The decay position was selected between 90 m and 160 m from the target with the decay probability dependent on its lifetime and energy. The generated  $K_L$  propagated to the decay point. If the  $K_L$  hits a collimator, the event was lost and MC generated a next event.

## 3.2 $K_L$ Decay

After  $K_L$  decayed, the daughter products were propagated from the decay point.

This section describes the generation methods for the decays which were used in this analysis, including normalization and background(See Section 4.1 for details.) decay modes.

---

\*We checked the difference of the energy spectrum by comparing the data and MC with  $K_L \rightarrow \pi^+\pi^-$ .

### 3.2.1 $K_L \rightarrow \pi^0 \mu^+ \mu^-$

This decay modes were generated with a flat phase space. The  $\pi^0$ 's were immediately forced to decay into  $2\gamma$ 's at the  $K_L$  decay position.

### 3.2.2 $K_L \rightarrow \pi^0 \pi^+ \pi^-$

The decay rate of  $K_L \rightarrow \pi^0 \pi^+ \pi^-$  dependent on the configurations of the momentum of the three pions. This dependence is called the Dalitz plot distribution and it may be written as [4]

$$|M(X, Y)|^2 = 1 + 0.67Y + 0.079Y^2 + 0.0X + 0.0098X^2, \quad (3.5)$$

$$X = \frac{s_2 - s_1}{m_{\pi^+}^2}, Y = \frac{s_3 - s_0}{m_{\pi^+}^2} \quad (3.6)$$

$$s_i = (P_K - P_i)^2, s_0 = \frac{1}{3}\Sigma s_i \quad (3.7)$$

where  $M(X, Y)$  is the matrix element,  $P_K$  is the kaon four momentum vector,  $m_i$  and  $P_i$  are the mass and four momentum vector of the  $i$ th pion, and  $i=1, 2, 3$  corresponds to the  $\pi^+$ ,  $\pi^0$ , and  $\pi^-$ . Momentum of three pions were therefore generated according to the Dalitz plot distribution in the rest frame of the neutral kaon. The  $\pi^0$ 's were immediately forced to decay into  $2\gamma$ 's at the  $K_L$  decay position.

### 3.2.3 $K_L \rightarrow \mu^+ \mu^- \gamma, K_L \rightarrow \mu^+ \mu^- \gamma \gamma$

$K_L \rightarrow \mu^+ \mu^- \gamma$  is muonic Dalitz decay. The differential decay spectrum of the Dalitz decay is defined by the Kroll-Wada formula[23],

$$\frac{d\Gamma}{dx} = \frac{2\alpha}{3} |f(x)|^2 \frac{(1-x)^3}{x} \left(1 + \frac{2M_{\mu\mu}^2}{xM_{K_L}^2}\right) \left(1 - \frac{4M_{\mu\mu}^2}{xM_{K_L}^2}\right)^{1/2}, \quad (3.8)$$

where  $x = M_{\mu\mu}^2/M_{K_L}^2$ , and  $f(x)$  is the form factor. The form factor was set to 1.0 in our MC.

$K_L \rightarrow \mu^+ \mu^- \gamma \gamma$  is a muonic Dalitz decay with an internal bremsstrahlung photon. The decay spectrum is defined by the Equation 3.8 with a radiative correction. For  $K_L \rightarrow \pi^0 \mu^+ \mu^-$  study, we generated  $K_L \rightarrow \mu^+ \mu^- \gamma \gamma$  with a 5 MeV infrared cutoff in the center of mass frame.

### 3.2.4 $K_L \rightarrow \pi^\pm \mu^\mp \nu(\bar{\nu})$

The semileptonic decay  $K_L \rightarrow \pi^\pm \mu^\mp \nu(\bar{\nu})(K_{\mu 3})$  is one of the most significant backgrounds in the search for  $K_L \rightarrow \pi^0 \mu^+ \mu^-$ . This decay will become a background to  $K_L \rightarrow \pi^0 \mu^+ \mu^-$ , if  $\pi^\pm$  is misidentified as a muon and there were two accidental photons.

$K_{\mu 3}$  was generated according to the semi-leptonic matrix element which is a pure vector form with a linear  $q^2$  interaction[24], where  $q^2$  is the momentum transfer squared between the kaon and the pion.

### 3.3 Tracing of Decay Products

The daughter particles from kaon decays were propagated through detector till they reach the CsI calorimeter. Muons were further propagated till they reach MU3 bank. Particles were terminated if particles go outside of the detector or hit the photon veto counters.

Charged particles passing through material in the detector between the vacuum region and the calorimeter could change its flight direction by the Coulomb multiple scattering. Long tail in the scattering distribution by single scattering was well reproduced, also. The muon scattering angle in the muon system will be described in Section 3.3.1.  $\pi^\pm$ s decayed in flight with its lifetime and energy. If  $\pi^\pm$  did not decay, it stopped at the CsI calorimeter in our MC. However, a small fraction of the pions can make a hit in MU3 banks. We will describe how to simulate such a case in Section 3.4.2.

The Monte Carlo simulation handled the photon conversion at the material for the energy above 0.1 GeV. The conversion probability was computed as  $(1 - e^{-\frac{7}{9}X})$  where  $X$  denotes the amount of material in terms of radiation length. The energy spectrum of electron-positron pair was determined by Bethe-Heitler formula. For the opening angle of electron and positron, we used an algorithm found in EGS4 shower simulation package [25, 26].

#### 3.3.1 Muon Scattering in Muon System

Muons were deflected by multiple scattering in the muon system. The scattering angle is very important, because the acceptance of  $K_L \rightarrow \pi^0 \mu^+ \mu^-$  heavily depends on it. In order to simulate the scattering correctly, we measured the width of the scattering angle as a function of the muon momentum by using data from a special run. (See details in Appendix B.) When muons reached the CsI calorimeter, we smeared the track angle by the Gaussian distribution with the measured sigma.

### 3.4 $\pi^\pm$ in Monte Carlo Simulation

Some of the  $K_L$  decays which include  $\pi^\pm$  become background to  $K_L \rightarrow \pi^0 \mu^+ \mu^-$  when  $\pi^\pm$  is identified as muon. If the energy deposit by a charged particle is consistent with Minimum Ionizing Particle(MIP) and there is a hit in MU3 bank, we identified the charged particle as muon. There are two possibilities that  $\pi^\pm$  is identified as muon. When  $\pi^\pm$  decayed in flight before the CsI calorimeter, the  $\mu^\pm$  from the decay could hit the MU3 banks. MU3 banks can also have a hit if  $\pi^\pm$  passed the CsI calorimeter as MIP and a particle in the shower reached MU3 banks. In order to reduce the CPU time for event generation, we used special methods for these cases as described below.

### 3.4.1 $\pi^\pm$ Decay

Because the lifetime of the charged pion is  $2.8 \times 10^{-8}$ sec, about 2% of  $\pi^\pm$  decay to muon upstream of the CsI calorimeter.

When we generated the MC events with  $\pi^\pm$  decay, we forced pions to decay. First, the Z position of the charged pion decay was chosen based on  $\pi^\pm$  energy and position of the parent  $K_L$ . The pion decayed to muon after it propagated to the calculated decay point. After that point, the daughter muon was propagated to MU3 bank. We assigned the probability of  $\pi^\pm$  to decay, between  $K_L$  decay position and the CsI calorimeter, as an event weight. In this analysis, this event weight was accumulated to calculate the effective number of events.

### 3.4.2 $\pi^\pm$ Punch Through Muon System

In our MC,  $\pi^\pm$  stopped its propagation at the CsI calorimeter as we described in Section 3.3. About 26% of  $\pi^\pm$  in  $K_L \rightarrow \pi^0\pi^+\pi^-$  passed the CsI calorimeter without making a hadron shower. While most of these  $\pi^\pm$  made a hadron shower and stopped in the muon shields, about 0.2% of them made a hit in MU3 bank. These hits were due to  $\pi^\pm$  decay within or downstream of the CsI calorimeter, and particles made by a hadron shower in the muon shields. In this thesis, we will call both of these cases as “ $\pi^\pm$  punch through”.

Before simulating the  $\pi^\pm$  punch through effect, we first estimated its probability by using GEANT simulation[27]. The configuration which we used in GEANT simulation had only the CsI calorimeter and the muon system. Charged pions were generated at the front face of CsI Calorimeter. Let us define the  $\pi^\pm$  punch through probability( $P_{PT}$ ) as the probability that the energy deposit in the CsI calorimeter by a  $\pi^\pm$  is less than 1GeV, and MU3 bank has a hit. Figure 3.1 shows the  $P_{PT}$  as a function of  $\pi^\pm$  momentum. We fit the  $P_{PT}$  dependence to a liner function.

When we simulate events with  $\pi^\pm$  punch through, we forced the punch through, and assigned an weight:

$$Event\ Weight = P_{PT} \times P_{no\_decay}, \quad (3.9)$$

for each such  $\pi^\pm$  where  $P_{no\_decay}$  is the probability that  $\pi^\pm$  reached CsI calorimeter without decaying. The tracing a  $\pi^\pm$  in the detector for this case is treated same as muon.

### 3.4.3 Summary of $\pi^\pm$ misidentification simulation

If the decay products of parent  $K_L$  included more than one charged pions, the event weight of the decay was the product of all the event weights.

In order to check the consistency between MC and data for  $\pi^\pm$  misidentification, we used  $\pi^\pm$  in  $K_L \rightarrow \pi e \nu$  decays.

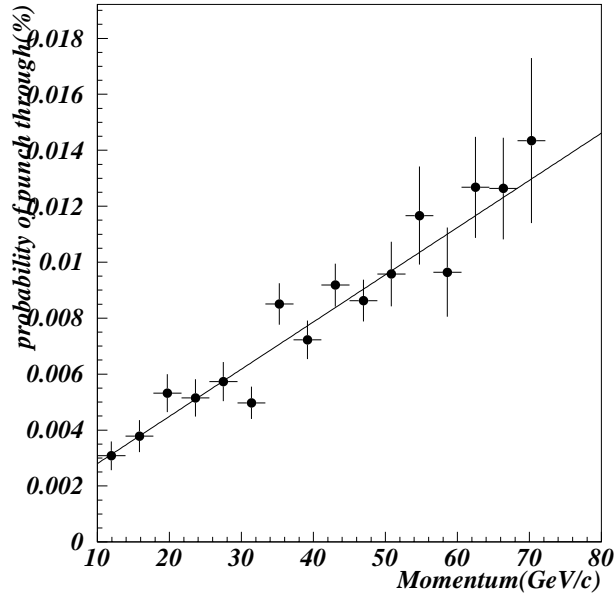


Figure 3.1: The  $\pi^\pm$  punch through probability as a function of  $\pi^\pm$  momentum, obtained by GEANT simulation. The line shows the result from the linear fit.

Figure 3.2 shows the probability that  $\pi^\pm$  is identified as a muon, as a function of  $\pi^\pm$  momentum. The solid line shows the probability due to  $\pi^\pm$  decay and accidental effect. The solid line shows the sum of the dashed line and the  $\pi^\pm$  punch through probability. The dots show the probability that  $\pi^\pm$  in  $K_L \rightarrow \pi e \nu$  data sample satisfied the requirement for muon identification.

There is a discrepancy between data and our MC in the low momentum region. This effect will be corrected for in Chapter 5.

## 3.5 Detector Response

### 3.5.1 Photon Veto Counters

When a photon or an electron hit one of the photon veto counters, the energy deposit was determined using calibration constants and the energy of the incident particle. The deposited energy was smeared by Gaussian distribution whose width was derived from data.

Charged particles except for electrons were treated as MIP, and their energy deposit was smeared by Gaussian. The width and mean of energy deposit were determined from another set of calibration constants which were derived by using muons in data.

If the smeared energy deposit was above trigger threshold of the counter,

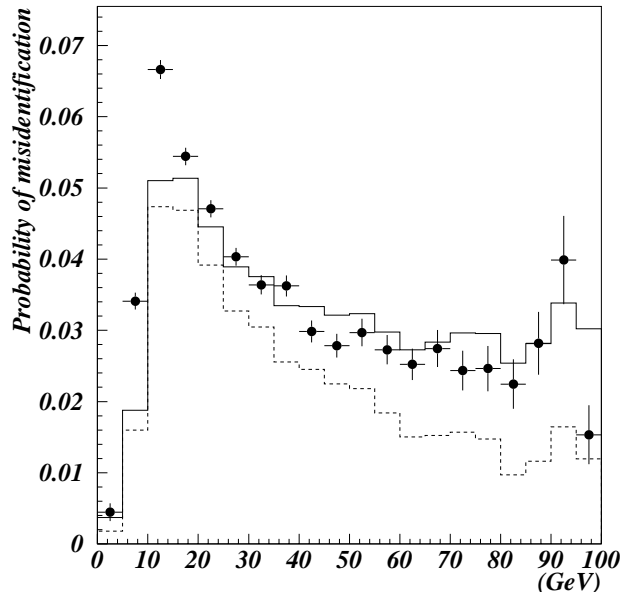


Figure 3.2: The probability that  $\pi^\pm$  is identified as muon for MC(solid line) and data(dot) as a function of  $\pi^\pm$  momentum. The dot shows the probability of the misidentification of the  $\pi^\pm$  in  $K_L \rightarrow \pi e \nu$  data. The dashed line shows the probability of misidentifying by  $\pi^\pm$  decay in MC. The solid line shows the sum of the dashed line and Figure 3.1.

the particle's hit was recognized at the Level 1 trigger. Finally, the energy deposit was digitized to ADC counts based on the gain of the each counter which had been calibrated with muons.

### 3.5.2 Drift Chamber

When a charged particle passed each drift chamber, the distance from the particle position to the closest wire in each plane was converted to a drift time, based on the calibration constants. The drift time was smeared based on the calibration results, and was recorded as TDC counts. The inefficiency of the drift chamber was simulated by ignoring the hit information according to the inefficiency of each plane.

The  $\delta$ -ray emission in the chamber gas was simulated in the following manner. When a charged particle passed through a material, a  $\delta$ -ray was emitted perpendicular to the parent particle trajectory with the probability  $P$ .  $P$  is defined by

$$P = 154(\text{keVcm}^2/\text{g}) \times \frac{Z}{A} \times d(\text{g/cm}^3) \times L(\text{cm}) \times \frac{1}{E(\text{keV})},$$

where  $L$  is the length of the material,  $Z$  is Atomic Number,  $A$  is Atomic Mass,

$d$  is the density of material, and  $E$  is the particle energy.

### 3.5.3 CsI Calorimeter

#### Crystal

When a photon or an electron reached the CsI calorimeter, it produced an electromagnetic shower. In order to model the electromagnetic shower, a collection of shower shapes(shower library) was made by electron sample in  $K_{e3}$  decays. The showers were binned in 6 energy bins covering 2~64GeV, and six size of the position bins:0.2mm×0.2mm ~ 0.7mm×0.7mm. Each electron sample of shower library contained energy deposits in 2cm thick slices(along Z direction) in 13 × 13 2.5 cm crystals around the impact crystal. The 5.0 cm crystal was treated as four 2.5 cm crystals. There was similar library for charged pions which was made by Geant simulation. For each photon or electron, its shower mean depth was calculated by

$$D(m) = A + 0.018 \times \ln E(\text{GeV}), \quad (3.10)$$

where D is the shower mean depth, A is 0.12 for photon, 0.11 for electron, E is the energy of the particle. The transverse position of the particle was calculated at the shower mean depth. A sample of shower was picked up based on the energy of the particle and the transverse position.

Once a shower sample was picked from the shower library, the energy scale was normalized to original energy of the particle incident to the CsI calorimeter.

The energy deposit by muons was derived from Landau distribution[28, 29] based on  $dE/dx$  in the 50cm long CsI.

#### DPMT

The CsI time spectrum was modeled with three exponential decays. Pure-CsI crystal has two fast components with time constants of roughly 10 and 40 nsec, having roughly equal areas, and a slow time component with a time constant of order 1  $\mu$ sec, having 10-20 % of the total area. The CsI time spectrum was formed with all the parameters of the three exponential decays which were obtained in advance.

Because the DPMT operation was synchronizing with accelerator RF, time jitter in the CsI signal with respect to the RF was also simulated. The time jitter was modeled as a Gaussian, with a sigma of 0.6 nsec[30], and was applied for all crystals.

The energy in each slice was smeared to simulate fluctuations from photostatistics. The number of photoelectrons per GeV for each crystal(typically 20 photoelectrons per MeV), was measured in advance, and used to smear the energy in each slice as  $\sigma(E) = (E/N_{p.e.})^{\frac{1}{2}}$  where  $N_{p.e.}$  is the number of photo-electrons per GeV.

Finally, MC simulated QIE. The constants for QIE(slope and intercepts for each capacitor, range, and crystal, the errors in slopes and offsets, the pedestals for each capacitor and range) were measured in advance. The digitization were performed in each RF period for each crystal. At the same time, the HCC was simulated by tabulating those crystals whose energy was above the threshold(typically 1GeV) and performing the cluster counting algorithm.

### **3.5.4 Trigger Hodoscopes and Muon Counters**

When a charged particle passed the scintillation banks, the hit information of the trigger hodoscope was saved after simulating for the inefficiency. The inefficiencies of the trigger hodoscopes were measured from the data.

In the simulation, MU3 banks were assumed to be 100% efficient and have no gaps between counters. These effects will be estimated in Chapter 4.6.2.

## **3.6 Accidental Activity**

The effect of the accidental activities in the detector, due to accidental particles and noise was also implemented in MC. In order to apply the accidental effects to MC, we overlayed the accidental data to the MC events after digitization. ADC counts were simply summed together, latch bits were ORed, and only the first hit in TDC reading was kept.

# Chapter 4

## Event Selection

The main purpose of this chapter is to decide the cuts for selecting  $K_L \rightarrow \pi^0 \mu^+ \mu^-$  by analyzing signal and background Monte Carlo(MC) events.

At first, we will describe the backgrounds to  $K_L \rightarrow \pi^0 \mu^+ \mu^-$ . Next, we will describe the reconstruction of the events and decide the selection cuts by looking at the MC events. Finally, we will describe the analysis for normalization mode and calculate the sensitivity.

### 4.1 Backgrounds to $K_L \rightarrow \pi^0 \mu^+ \mu^-$

In this section, we will describe the characteristic of the backgrounds to  $K_L \rightarrow \pi^0 \mu^+ \mu^-$  and the strategy for rejecting them. Table 4.1 summarizes the backgrounds to  $K_L \rightarrow \pi^0 \mu^+ \mu^-$ . There are two kinds of background decays: the  $K_L$  decays including two muons, and the  $K_L$  decays including  $\pi^\pm$  which was misidentified as muon.  $\gamma_{acc}$  represents the accidental photon.

mode	Branching Ratio
$K_L \rightarrow \mu^+ \mu^- \gamma + \gamma_{acc}$	$3.23 \times 10^{-7}$
$K_L \rightarrow \mu^+ \mu^- \gamma \gamma$	$1.55 \times 10^{-9}$
$K_L \rightarrow \pi^0 \pi^+ \pi^-$	0.123
$K_L \rightarrow \pi^\pm \mu^\mp \nu(\bar{\nu}) + 2\gamma_{acc}$	0.273
$K_L \rightarrow \pi^+ \pi^- + 2\gamma_{acc}$	$2.03 \times 10^{-3}$
$K_L \rightarrow \pi^+ \pi^- \gamma + \gamma_{acc}$	$4.61 \times 10^{-5}$
$K_L \rightarrow \pi^0 \pi^\pm \mu^\mp \nu$	$5.88 \times 10^{-5}$

Table 4.1: Backgrounds to  $K_L \rightarrow \pi^0 \mu^+ \mu^-$  with their branching ratio. Branching ratio of  $K_L \rightarrow \mu^+ \mu^- \gamma \gamma$  was calculated in Appendix A.  $\gamma_{acc}$  means the accidental photon. The infrared cutoff for  $K_L \rightarrow \mu^+ \mu^- \gamma \gamma$  analysis is set to 10 MeV in the center of mass system.

#### 4.1.1 $K_L \rightarrow \mu^+\mu^-\gamma\gamma$ , $K_L \rightarrow \mu^+\mu^-\gamma + \gamma_{acc}$

$K_L \rightarrow \mu^+\mu^-\gamma\gamma$  decay is  $K_L \rightarrow \mu^+\mu^-\gamma$  with an internal bremsstrahlung photon. The decay products of  $K_L \rightarrow \mu^+\mu^-\gamma\gamma$  are exactly the same as those of  $K_L \rightarrow \pi^0\mu^+\mu^-$ , and the reconstructed invariant mass( $M_{\mu^+\mu^-\gamma\gamma}$ ) peaks at the kaon mass. Therefore,  $K_L \rightarrow \mu^+\mu^-\gamma\gamma$  is the most dangerous background to  $K_L \rightarrow \pi^0\mu^+\mu^-$ . The  $K_L \rightarrow \mu^+\mu^-\gamma\gamma$  has never been observed in experiments, and it is very important to know the branching ratio of  $K_L \rightarrow \mu^+\mu^-\gamma\gamma$ . As described in Appendix A, we observed the decay for the first time, and measured its branching ratio

$$BR(K_L \rightarrow \mu^+\mu^-\gamma\gamma, E^* \geq 10 MeV) = [1.55 \pm 0.74(stat) \pm 0.11(sys.)] \times 10^{-9},$$

where  $E^*$  is the photon energy in the center of kaon mass. This decay mode was rejected based on the kinematic variables: the mass of the two photons( $M_{\gamma\gamma}$ ) and the mass of the two muons( $M_{\mu\mu}$ ). In case of the  $K_L \rightarrow \pi^0\mu^+\mu^-$ ,  $M_{\mu\mu}$  is limited at  $(M_K - M_{\pi^0})$ , whereas the high side tail of  $M_{\mu\mu}$  of  $K_L \rightarrow \mu^+\mu^-\gamma\gamma$  extends beyond this limit.

$K_L \rightarrow \mu^+\mu^-\gamma + \gamma_{acc}$  is a muonic dalitz decay with an accidental photon. The probability of having 1 accidental photon was 1.8% on average in our experiment. The reconstructed kaon mass is larger than the kaon mass, so that this decay is not a severe background. The cuts for rejecting  $K_L \rightarrow \mu^+\mu^-\gamma\gamma$  are effective for this decay, also.

#### 4.1.2 Kaon Decays including $\pi^\pm$

Some of the kaon decays which include  $\pi^\pm$  have large branching ratios as shown in Table 4.1. When a  $\pi^\pm$  is misidentified as muon, those decays can be backgrounds to  $K_L \rightarrow \pi^0\mu^+\mu^-$ . The misidentification can happen in the following cases.

- $\pi^\pm \rightarrow \mu^\pm + \nu(\bar{\nu})$   
The lifetime of the  $\pi^\pm$  is  $2.6 \times 10^{-8}$ s. For example, 2% of the charged pions in  $K_L \rightarrow \pi^0\pi^+\pi^-$  decay to muon in flight before reaching the CsI calorimeter. The muon which comes from  $\pi^\pm$  decay can hit MU3 bank if the muon has more than 7(GeV/c).  
When a  $\pi^\pm$  decays in flight between the drift chamber DC1 and DC4, its trajectory is bent, so 4 hit points in the drift chambers will not be consistent with hits by a single track. If  $\pi^\pm$  decays upstream of the DC 2, a good charged vertex may not be found.
- $\pi^\pm$  punch through  
As described in Chapter 3,  $\pi^\pm$  can sometimes punch through the muon system and hit MU3 banks. In this case, charged track is not bent, so correct trajectories and vertex are found.

When we studied the background decay modes with  $\pi^\pm$ , we generated MC for each case. If the decay includes two  $\pi^\pm$ , we generated MC with each combination of the misidentification process.

There are two major methods to reduce backgrounds with  $\pi^\pm$ . One is to apply tight cuts on kinematic variables such as  $M_{\pi^0\mu^+\mu^-}$ , since the  $\pi^\pm - \mu^\pm$  mass difference will shift the distributions. The other is to apply tight cuts on track and vertex reconstruction.

$$K_L \rightarrow \pi^0\pi^+\pi^-$$

The branching ratio of this decay is 12.56%. When both  $\pi^\pm$ s were misidentified as muons, this decay can become a background to  $K_L \rightarrow \pi^0\mu^+\mu^-$ . The reconstructed invariant mass ( $M_{\pi^0\mu^+\mu^-}$ ) of  $K_L \rightarrow \pi^0\pi^+\pi^-$  background events is peaked around  $450\text{MeV}/c^2$ . The events which include decayed  $\pi^\pm$  have wider  $M_{\pi^0\mu^+\mu^-}$  distribution than those which include punch through  $\pi^\pm$  due to track misreconstruction. Therefore, this decay is a dangerous background when both  $\pi^\pm$  decay in flight before hitting the CsI calorimeter.

$$K_L \rightarrow \pi^\pm\mu^\mp\nu(\bar{\nu}) + 2\gamma_{acc}$$

The branching ratio of this decay is 27.3%. This decay will become a background to  $K_L \rightarrow \pi^0\mu^+\mu^-$ , if  $\pi^\pm$  is misidentified as a muon and there were two accidental photons. The probability of having two accidental photons was 0.0071% on average.

Although there is a missing momentum by  $\nu$ , two accidental photons can make the  $M_{\pi^0\mu^+\mu^-}$  close to the kaon mass. Therefore, this decay is also a dangerous background.

$$K_L \rightarrow \pi^0\pi^\pm\mu^\mp\nu$$

This decay has never been observed. We estimated the branching ratio of this decay from following equation.

$$\begin{aligned} BR(K_L \rightarrow \pi^0\pi^\pm\mu^\mp\nu) &= \frac{\Gamma(K^+)}{\Gamma(K_L)} \times BR(K^+ \rightarrow \pi^+\pi^-\mu^+\nu) \\ &= 5.88 \times 10^{-5} \end{aligned} \tag{4.1}$$

This decay includes  $\pi^0$  and a muon so that this decay is a dangerous background, despite its small branching ratio.

## 4.2 Policy of $K_L \rightarrow \pi^0\mu^+\mu^-$ Analysis

We will describe our event selection in the following sections. The event selection consists of three parts. First, we reconstruct events from the detector

information. Second, we require two muons and two photons by particle identification. Finally, we select  $K_L \rightarrow \pi^0 \mu^+ \mu^-$  by cutting on calculated kinematic variables while rejecting the remaining background events.

When there are a few remaining events after the selection, one could introduce a bias by tightening the cuts to reject them. This could remove signal events, and a wrong confidence level will be assigned to the upper limit of the branching ratio. This dangerous bias should be avoided. Therefore, we determined the analysis cuts by using signal and background events generated by MC. We used the data for checking the agreement between MC events and data. In order to avoid any possible biases, we masked the events in the signal region until we finalized all the requirements. The masked region is defined as:

- $492 < M_K (MeV/c^2) < 504$  and
- $P_T^2 < 100 (MeV/c)^2$

where  $M_K$  is the reconstructed invariant mass of  $\pi^0 \mu^+ \mu^-$ , and  $P_T$  is a component of  $\pi^0 \mu^+ \mu^-$  momentum transverse to the initial  $K_L$  direction.

After we decide the requirements, we will estimate how many background events are expected in the signal region. We will discuss the validity of background estimation in the next chapter.

## 4.3 Event Reconstruction

### 4.3.1 Cluster Finding

We used two algorithms for finding energy clusters in the CsI calorimeter.

One algorithm is called HCC clustering. First, it looks for a crystal which has maximum energy among adjacent crystals that were recognized to have more than 1GeV energy deposit by the Hardware Cluster Counter(Level 2 trigger processor). Such a crystal with the maximum energy is called a seed of a HCC cluster. A cluster was made of  $7 \times 7$  crystals centered around the seed crystal for  $2.5\text{cm} \times 2.5\text{cm}$  crystals. For  $5.0\text{cm} \times 5.0\text{cm}$  crystals, the cluster was made of  $3 \times 3$  crystals. If a cluster seed is close to the boundary between  $5\text{cm}$  and  $2.5\text{cm}$  crystals, four small crystals were treated as one large crystal. An energy cluster which was found by this algorithm was called ‘‘HCC cluster’’.

Another algorithm is called ‘‘software clustering’’. The software clustering forms clusters by searching for a crystal whose energy is above 0.1 GeV and has the maximum energy among the neighbors. The software clustering algorithm searches for seeds only among crystals which have not already been included in a hardware cluster. The same number of crystals as HCC cluster were used to form a cluster. A cluster whose energy was greater than 250 MeV was accepted as a ‘‘software cluster’’. The energy of the cluster was calculated by summing energy of all the the crystals which formed a cluster.

Because most of energy cluster of photons and electrons have at least one crystal which have more than 1GeV. Therefore, the HCC clustering can identify the photon energy cluster. On the other hand, the software clustering algorithm is for finding clusters whose have nothing to do with HCC clusters.

Particle position at the calorimeter was extracted from the energy ratio between the central and adjacent rows or columns. The relation between the hit position and the energy was derived from electron samples in  $K_L \rightarrow \pi e \nu$  decays whose momentum and positions were well measured by the spectrometer. The resulting resolution in position was estimated to be roughly 1 mm for 15 GeV photons.

After finding clusters and calculating their energies and positions, some corrections were made for the clusters. Clusters which are adjacent to the beam hole or the calorimeter edge do not have all the  $7 \times 7$  or  $3 \times 3$  crystals to sum the energies. The energy for each missing block is calculated from the measured position of the cluster, and added to the cluster energy. Finally, the total energy of the cluster was corrected for the energy leakage outside of  $7 \times 7$  small crystals and  $3 \times 3$  large crystals, back of those crystals, and energy loss in the wrapping materials. Based on a study using GEANT, the fraction of the missing energy is independent of the energy of the incident particle, and depends only on the size of crystals. The correction constants were  $1.0/0.9599(=1.042)$  for  $7 \times 7$  small crystals, and  $1.0/0.9441(=1.059)$  for  $3 \times 3$  large crystals(also for boundary region of large and small crystals), respectively.

### 4.3.2 Finding Track Candidates

In this section, we will describe the algorithm for finding trajectories of the charged particle which passed the drift chambers.

As described in Section 2.2.2, TDC counts of the hit sense wire were recorded in data. The drift time which was calculated by the TDC counts was translated to a distance from sense wire to the closest point of the charged particle trajectory.

Each trajectory produced a pair of hits in the offset planes in the same view. The sum of the two drift distances(SOD) of the hit pair should be equal to the distance between the two sense wires(0.635 cm). Figure 4.1 shows the distribution of the SOD after subtracting the 0.635 cm offset. We regard SOD whose range is between 0.535cm and 0.735cm for drift chamber 1 and 2 (between 0.485cm and 0.785cm for drift chamber 3 and 4) as good SOD.

Next, we look for a set of good SOD pairs which lie along a straight line in Y view. For each combination of a chamber 1 pair and a chamber 4 pair, the track position is projected to chamber 2 and 3, and those chambers are checked for pairs which lie within 1cm. Once 4 such pairs have been found, they were fit to a straight line.

There are two steps for finding tracks in x view. First, we found tracks in each upstream and downstream of the magnet. We selected combinations of good SOD pairs whose angle between them and the Z axis is less than

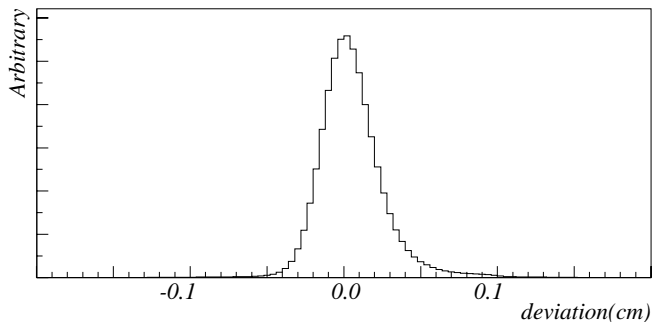


Figure 4.1: The deviation of sum of drift distance from the offset of 6.35 mm.

75.0 mrad(150mrad) for upstream(downstream).

Next, we looked for good combinations of the upstream and downstream x track candidates by requiring the distance between the candidates at the center of the magnet to be less than 1 mm. The downstream x track candidate should point a hit in V or V' bank. For each view, we required that there are 2 or more track candidates.

Finally, we looked for the right combination of x and y track among the candidates by requiring that the tracks have a “matched cluster” which means the distance between the projected position of the track and cluster is less than 7.0 cm. We calculated the momentum of the charged particles by using a known momentum kick and track information in x view.

### 4.3.3 Vertex Finding

We looked for tracks which originated from a common vertex. In each x and y view, we projected each pair of the track candidates into the decay region. We calculated the Z position of the intersection and its error due to resolution effects. If the ranges of the allowed Z position of the intersection were overlapped, we regard the track candidates as tracks originating from a common vertex. The vertex Z position was calculated by:

$$Z_{vertex} = \frac{Z_x \times \delta_{\theta_x}^2 + Z_y \times \delta_{\theta_y}^2}{\delta_{\theta_x}^2 + \delta_{\theta_y}^2},$$

where  $Z_{x(y)}$  is the Z vertex found in x(y) view,  $\delta_{\theta_{x(y)}}$  is the opening angle of the two tracks in x(y) view. To calculate the x and y positions of the vertex, we projected the two upstream tracks to  $Z_{vertex}$  and took the average of the each projected track position.

At last, we fit the eight space points on the upstream chambers to determine the vertex point and the slopes of the tracks. The chi-square of the fit was called  $\chi_{vertex}^2$ . Another chisquare( $\chi_{offset}^2$ ) for the track offset at the center of the magnet was calculated for the vertex candidate. We chose the best vertex

candidate by calculating a new variable which combines  $\chi_{vertex}^2$ ,  $\chi_{offset}^2$ , and the number of bad SOD pairs and single hits.

For the best vertex, we required the following conditions. (See Figure 4.2.)

- $\chi_{vertex}^2 < 10$ (shown in Figure 4.2)
- There are only two tracks(No extra tracks)
- $100 < Z_{Vertex}(m) < 158$
- Projected position of the vertex from the target to the CsI calorimeter is within 7.5cm from the center of the beam hole.

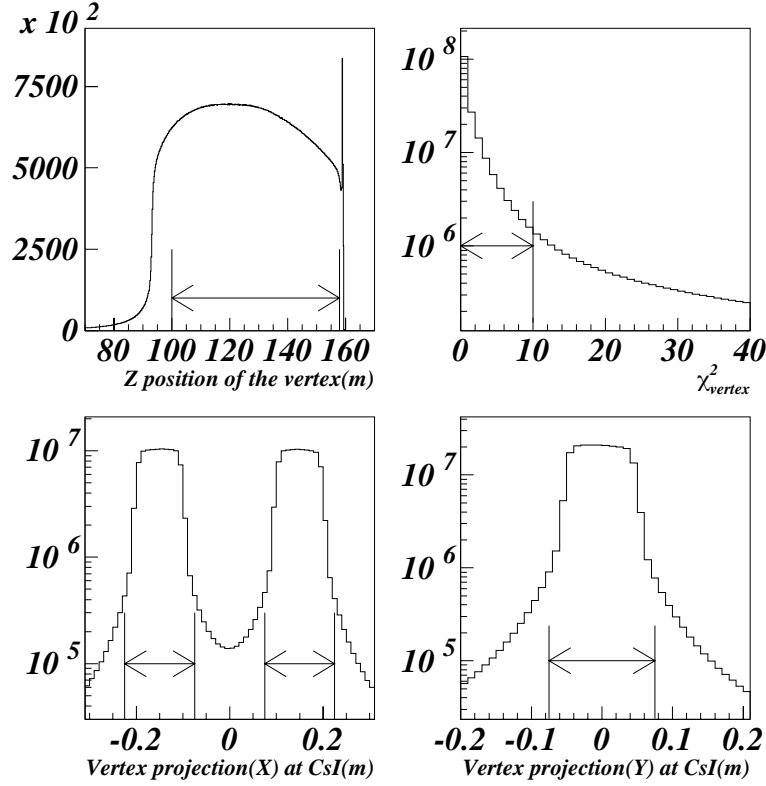


Figure 4.2: The distributions for the vertex variables for the  $K_L \rightarrow \pi^0 \mu^+ \mu^-$  after the vertex reconstruction. The top left plot shows the Z distribution of the reconstructed vertex. The top right plot shows the  $\chi_{vertex}^2$  distribution. The bottom plots shows the projected position of the vertex from the target to the CsI calorimeter. The bottom left(right) plot shows the X(Y) distribution of the projection. The arrows in the plots show our requirements for the vertex.

The last two cuts were applied to avoid accepting events which were made by the beam interaction with detector material( collimator and vacuum window).

#### 4.3.4 Photon Veto

The  $K_L \rightarrow \pi^0 \mu^+ \mu^-$  trigger required no hits in the photon veto at the Level 1 trigger. On the other hand, the  $K_L \rightarrow \pi^0 \pi^+ \pi^-$  trigger did not require photon veto. We required the photon energy measured by ADC of the RC, SA, CIA to be less than 0.3GeV for both triggers.

### 4.4 Particle Identification

In this section, we will require the two muons and two photons in the event.

#### 4.4.1 $\mu$ identification

As shown in Figure 4.3, muons deposit their energy by ionization in the CsI calorimeter. On the other hand, electrons deposit most of their energies in the CsI calorimeter by generating electromagnetic shower. About 74% of  $\pi^\pm$ s make hadron showers and deposit part of their energy in the CsI calorimeter. The distribution of energy deposit in the CsI calorimeter by muon is shown in Figure 4.3. We required the cluster energy to be less than 1GeV.

There are 5m thick iron and 10cm thick Pb wall( 30.4 interaction lengths total) between MU3 banks and the CsI calorimeter, to stop charged pions. To pass through the muon system, the momentum of muon has to be more than 7GeV/c.

To confirm the threshold, we used Muon runs with magnet on to check the efficiency for detecting muons. In the Muon run, we inserted two beam stops which were made of steel with 28.5cm and 21.1cm thickness at 46.4m and 50.1m downstream of the target. Therefore, only muons penetrated to the KTeV detector. We selected events which have one reconstructed track which deposited less than 1 GeV in the CsI calorimeter. The extrapolated position of the reconstructed track should be 20cm away from the edge of the MU3 bank. We calculated the efficiency of MU3 bank for detecting  $\mu$  as

$$Efficiency = \frac{\#MU3}{\#\mu},$$

where  $\#\mu$  means the number of the selected  $\mu$  track sample, and  $\#MU3$  means the number of events which has one or more intime TDC hits in MU3 counters. Figure 4.4 shows the efficiency as a function of muon momentum. We required the muon momentum to be greater than 10(GeV/c) to get more than 98% efficiency.

Figure 4.5 shows the momentum distribution of  $\mu$  in the  $K_L \rightarrow \pi^0 \mu^+ \mu^-$  MC. The fraction of muons which have more then 100(GeV/c) is about 0.1%.

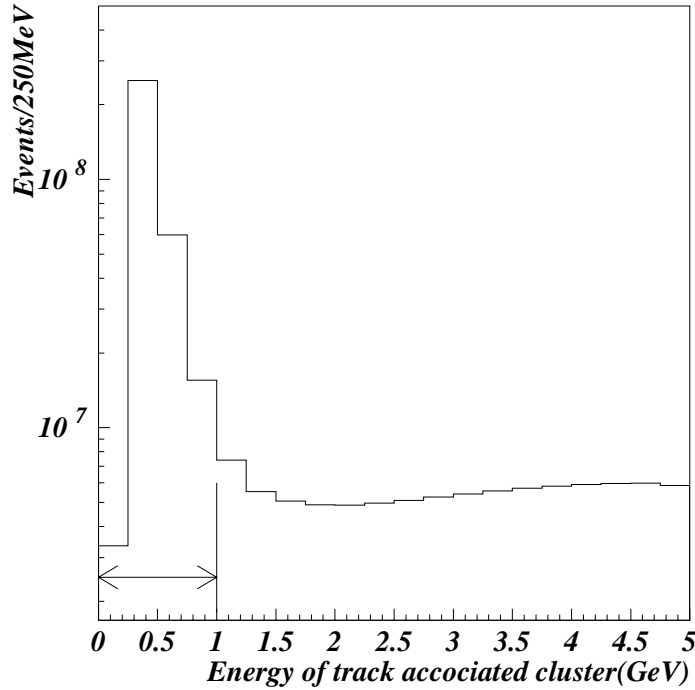


Figure 4.3: The energy distribution of the cluster associated with a track at CsI calorimeter for  $K_L \rightarrow \pi^0 \mu^+ \mu^-$  trigger events.

Therefore, the maximum momentum of the muon was set to  $100(\text{GeV}/c)$  to reduce background events which include decayed  $\pi^\pm$  with mismeasured momentum.

Level 1 trigger required 2 or more hits in each MU3 bank. If a muon emits a delta ray at the downstream surface of the steel just upstream of MU3, MU3 bank can have hits in neighboring counters. In analysis, we counted the number of isolated hits to neglect the delta ray hits. Figure 4.6 shows the number of isolated hits in each MU3 bank. We required two intimate hits in each MU3 bank.

#### 4.4.2 Gamma identification

We required that there are 2 HCC clusters which were not pointed by the tracks. We regard these clusters as photon.

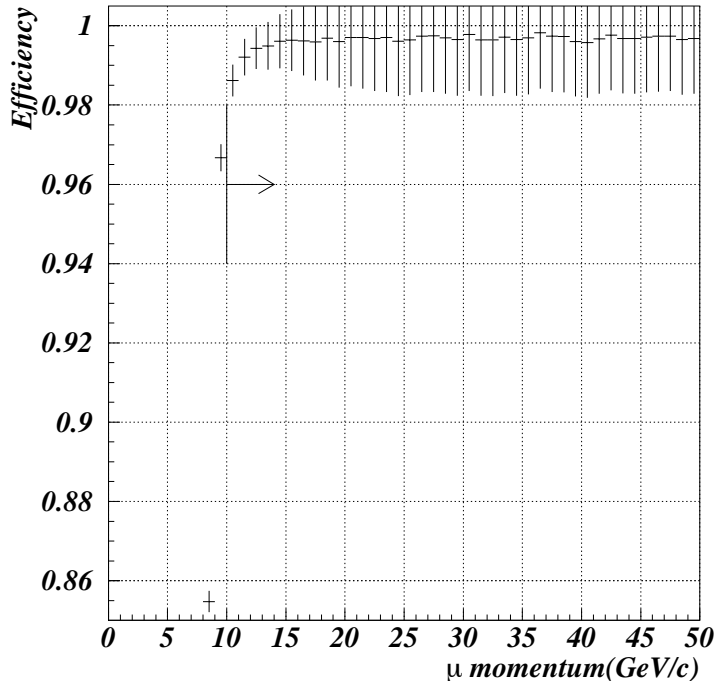


Figure 4.4: The efficiency for detecting muons by MU3x bank as a function of its momentum. We required more than 10GeV/c for muon momentum as shown by arrow in the plot.

## 4.5 Kinematic cuts

### 4.5.1 $\pi^0$ mass

In order to select events with a  $\pi^0$ , we calculated the invariant mass of the 2 photons by assuming that they came from the charged vertex. The square of the invariant mass is defined by

$$\begin{aligned}
 M_{\gamma\gamma}^2 &= 2E_1E_2(1 - \cos\theta_{12}) \\
 &\simeq E_1E_2\left(\frac{r_{12}}{Z}\right)^2,
 \end{aligned}
 \tag{4.2}$$

in a small angle approximation where  $E_{1,2}$  means the photon energies,  $\theta_{12}$  represents the opening angle between the two photons,  $r_{12}$  represents the distance between two photons, and  $Z$  represents the distance between the vertex and the CsI calorimeter.

Figure 4.7 shows a plot of the  $M_{\gamma\gamma}$  distribution for  $K_L \rightarrow \pi^0\mu^+\mu^-$  MC events. We required the  $M_{\gamma\gamma}$  to be within  $\pm 3 \text{ MeV}/c^2 (2\sigma)$  of the nominal  $\pi^0$  mass. This cut keeps 93.7% of signal and rejects 99.5% of  $K_L \rightarrow \pi^\pm\mu^\mp\nu(\bar{\nu})$  and 97.1% of  $K_L \rightarrow \mu^+\mu^-\gamma\gamma$ .

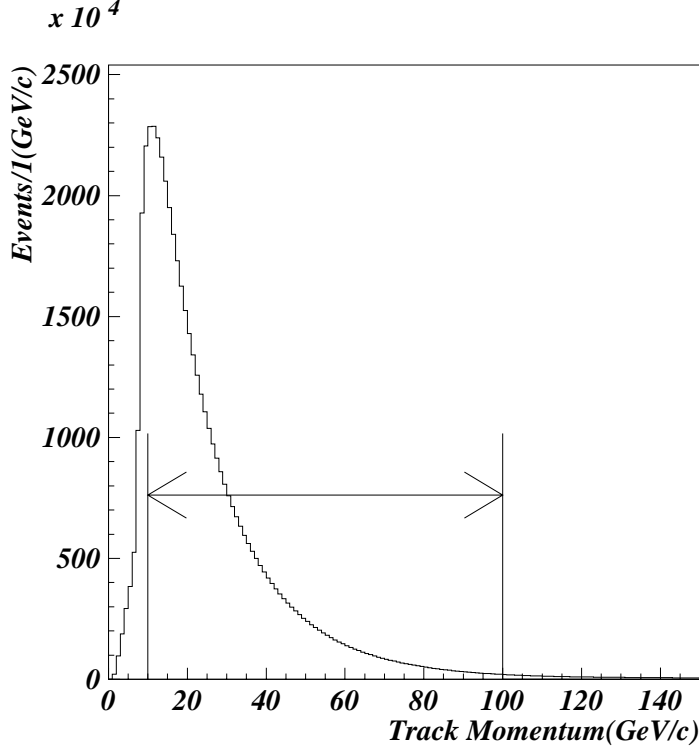


Figure 4.5: The  $\mu$  momentum distribution of the  $K_L \rightarrow \pi^0 \mu^+ \mu^-$  for the  $K_L \rightarrow \pi^0 \mu^+ \mu^-$  trigger events after the event reconstruction. We required the momentum to be greater than  $10 \text{ GeV}/c$  and less than  $100 \text{ GeV}/c$  as shown by arrow in the plot.

### 4.5.2 Invariant Mass of the Charged Tracks ( $M_{\mu\mu}$ )

$M_{\mu\mu}$  is the invariant mass of the charged tracks assuming that they are muons. In case of the  $K_L \rightarrow \pi^0 \mu^+ \mu^-$ ,  $M_{\mu\mu}$  is limited by  $M_K - M_{\pi^0}$  whereas in  $K_L \rightarrow \mu^+ \mu^- \gamma \gamma$  and  $K_L \rightarrow \pi^\pm \mu^\mp \nu(\bar{\nu}) + 2\gamma_{acc}$   $M_{\mu\mu}$  has a high side tail above  $M_K - M_{\pi^0}$ . We required  $M_{\mu\mu}$  to be less than  $350 \text{ MeV}/c^2$  as shown in Figure 4.8. This cut kept 93.7% of the signal while rejecting 23.5% of  $K_L \rightarrow \mu^+ \mu^- \gamma \gamma$  and 49.5% of  $K_L \rightarrow \pi^\pm \mu^\mp \nu(\bar{\nu}) + 2\gamma_{acc}$ .

### 4.5.3 Missing longitudinal momentum parameter ( $P_{\pi^0}^2$ )

In order to confirm that the two photons came from  $\pi^0 \rightarrow \gamma \gamma$  decay in the  $K_L \rightarrow \pi^0 \mu^+ \mu^-$ , we calculated the square of the longitudinal momentum of  $\pi^0$  in the  $\mu\mu$ -center of mass frame; ( $P_{\pi^0}^2$ ). The  $P_{\pi^0}^2$  was given by

$$P_{\pi^0}^2 = \frac{(M_K^2 - M_{\mu\mu}^2 - M_{\pi^0}^2)^2 - 4M_{\mu\mu}^2 M_{\pi^0}^2 - 4M_K^2 P_{T\mu\mu}^2}{4(P_{T\mu\mu}^2 + M_{\mu\mu}^2)}, \quad (4.3)$$

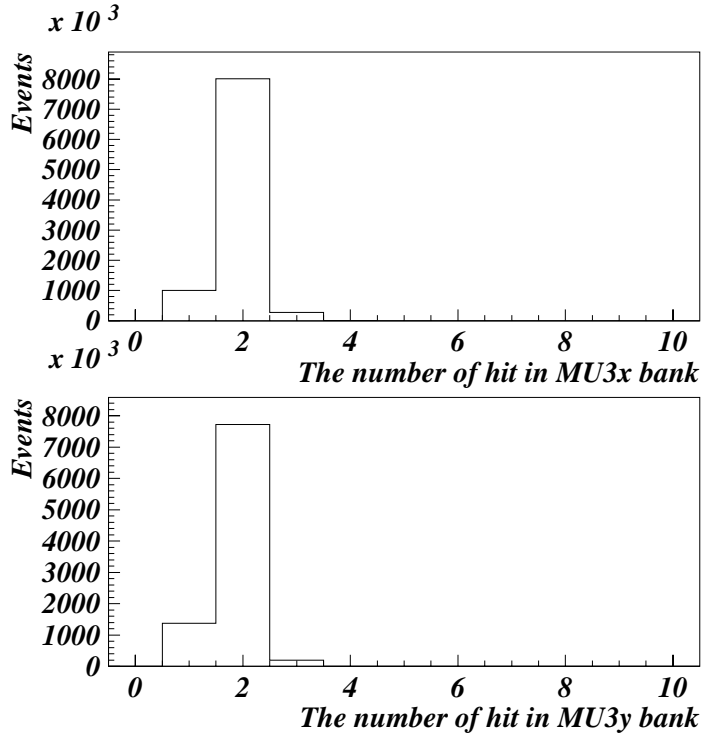


Figure 4.6: The upper(lower) plot shows the number of isolated hits in the MU3X(MU3Y) bank for the  $K_L \rightarrow \pi^0 \mu^+ \mu^-$  trigger data after the event reconstruction.

where  $M_K$  is the kaon mass,  $M_{\mu\mu}$  is the invariant mass of the two muons, the  $P_{T\mu\mu}$  is the transverse momentum of the two tracks, and  $M_{\pi^0}$  is the  $\pi^0$  mass. Note that only tracking information is used to obtain  $P_{\pi^0}^2$ .

The Figure 4.9 shows the  $P_{\pi^0}^2$  distribution of  $K_L \rightarrow \pi^0 \mu^+ \mu^-$ ,  $K_L \rightarrow \mu^+ \mu^- \gamma \gamma$ ,  $K_L \rightarrow \pi^0 \pi^+ \pi^-$  MC events, normalized by the area. For the  $K_L \rightarrow \pi^0 \mu^+ \mu^-$  events,  $P_{\pi^0}^2$  is larger than 0 with some resolution smearing.  $K_L \rightarrow \pi^\pm \mu^\mp \nu(\bar{\nu})$  are peaked below 0. In case of  $K_L \rightarrow \pi^0 \pi^+ \pi^-$ , the peak of  $P_{\pi^0}^2$  is shifted from that of  $K_L \rightarrow \pi^0 \mu^+ \mu^-$  because of the mass difference between  $\pi^\pm$  and  $\mu^\pm$ .

We required  $P_{\pi^0}^2$  to be between  $-0.01(\text{GeV}/c)^2$  and  $0.1(\text{GeV}/c)^2$ . This cut keeps 89.2% of signal and rejects 73% of  $K_L \rightarrow \pi^\pm \mu^\mp \nu(\bar{\nu}) + 2\gamma_{acc}$ , and 95% of  $K_L \rightarrow \pi^0 \pi^+ \pi^-$ .

#### 4.5.4 $P_T^2$ and Kaon Invariant Mass

In order to select events from  $K_L$ , we required the invariant mass of  $\gamma\gamma\mu\mu$  to be within  $\pm 6 \text{ MeV}/c^2$  ( $2.5\sigma$ ) of the nominal kaon mass as shown in Figure 4.10. The invariant mass is calculated by summing the four vectors of the two muons and two photons. The efficiency of this cut for  $K_L \rightarrow \pi^0 \mu^+ \mu^-$  is 97.7%.

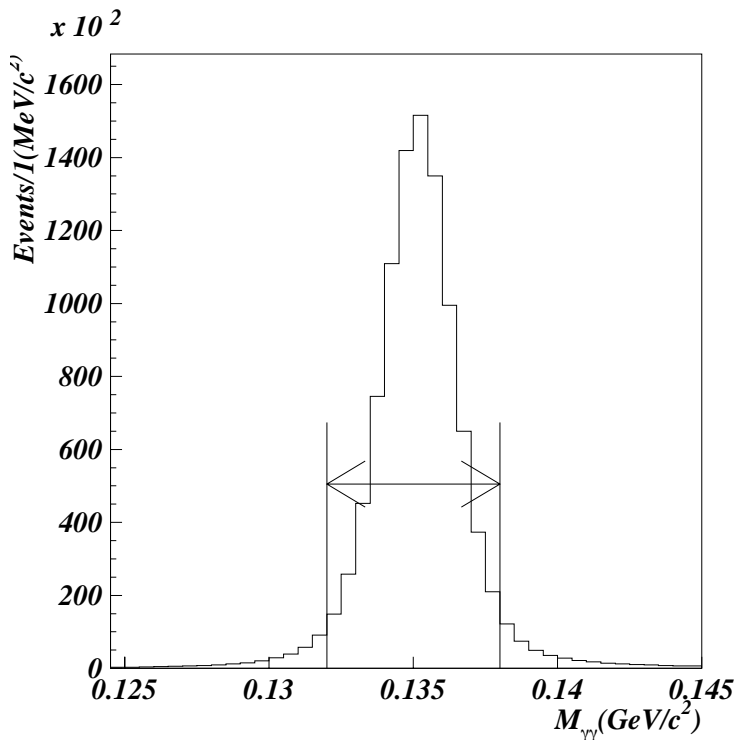


Figure 4.7: The  $\pi^0$  distribution of the  $K_L \rightarrow \pi^0 \mu^+ \mu^-$  MC after the event reconstruction. The arrow in the plot shows our requirement ( $132 < M_{\gamma\gamma} \text{ MeV}/c^2 < 138$ ).

By requiring a momentum conservation in the plane transverse to the  $K_L$  direction, we can reject background events which have missing or misidentified particles. The  $K_L$  direction was defined as the vector from the target to the decay vertex.  $P_T$  is the component of  $\pi^0 \mu^+ \mu^-$  momentum perpendicular to a vector from the target to the reconstructed decay vertex. The  $P_T^2$  of  $K_L \rightarrow \pi^0 \mu^+ \mu^-$  MC events is peaked at zero as shown in Figure 4.10. Therefore,  $P_T^2$  is required to be less than  $100(\text{MeV}/c)^2$ . The efficiency of this cut for  $K_L \rightarrow \pi^0 \mu^+ \mu^-$  is 92.0%.

## 4.6 Acceptance Correction

### 4.6.1 Energy deposit by muon

The muon energy deposit in the material was different between MC and data. This difference can affect the acceptance because the requirement on the energy deposit in the CsI calorimeter is very tight. Figure 4.11 shows the energy deposit measured in muon run and in MC. MC simulated the muon energy deposit as described in Chapter 3. The fraction of events which had an energy

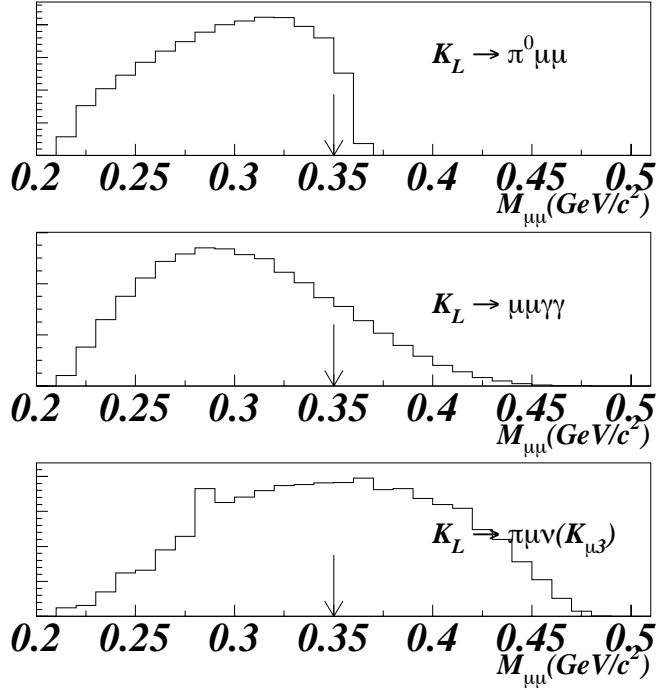


Figure 4.8:  $M_{\mu\mu}$  distribution for each decay after the  $\pi^0$  mass cut. The upper plot shows distribution of  $K_L \rightarrow \pi^0 \mu^+ \mu^-$ . The middle plot shows the distribution of the  $K_L \rightarrow \mu^+ \mu^- \gamma \gamma$ . The lower plot shows the distribution of the  $K_L \rightarrow \pi^\pm \mu^\mp \nu(\bar{\nu})$ . We required  $M_{\mu\mu} < 0.35 \text{ GeV}/c^2$  as indicated by the arrow.

deposit less than 1 GeV in the CsI calorimeter was 98.3% for the muon run, and 96.7% for muons generated in MC. We corrected the acceptance for the signal with 2 muons by  $(98.3 - 96.7) \times 2 = 3.3\%$ .

#### 4.6.2 MU3 bank efficiency

The efficiency of the MU3 bank hardware trigger was over 99.97% [31].

As shown in Figure 4.4, MU3 bank has some inefficiency even above 10 GeV/c. This is due to counter gaps between each counter of the MU3 bank. Figure 4.12 shows the efficiency of MU3 as a function of the extrapolated position of the reconstructed track at MU3 bank for tracks with momentum larger than 40 GeV/c in the muon run. The efficiency drops at each gap between counters. The average efficiency of MU3 banks for muons between 40 GeV/c and 100 GeV/c is 99.4%. Since MC did not include gaps between the counters, we corrected the acceptance by 1.2%.

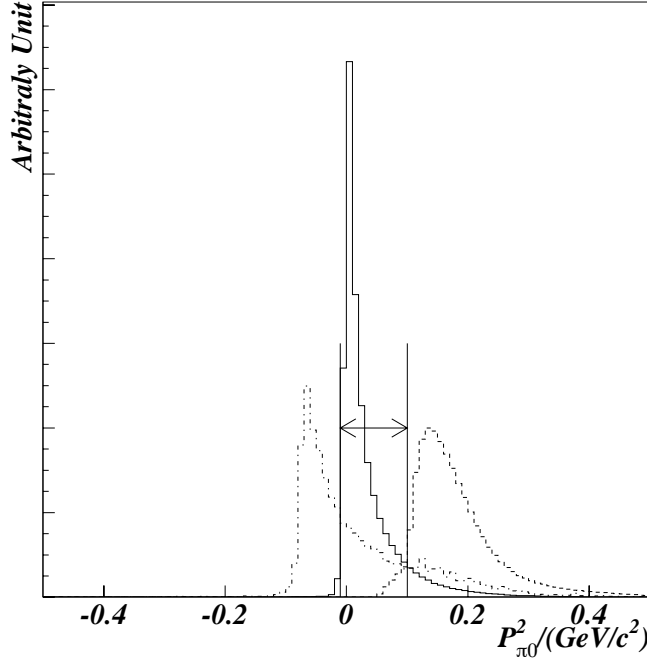


Figure 4.9: The  $P_{\pi^0}^2$  distribution after  $M_{\mu\mu}$  cut for  $K_L \rightarrow \pi^0 \mu^+ \mu^-$  (solid line),  $K_L \rightarrow \pi^0 \pi^+ \pi^-$  (dashed line),  $K_L \rightarrow \pi^\pm \mu^\mp \nu(\bar{\nu})$  (dotted line), and  $K_L \rightarrow \mu^+ \mu^- \gamma\gamma$  (dot-dash line) as normalized by area.

## 4.7 Analysis of the $K_L \rightarrow \pi^0 \pi^+ \pi^-$

We used  $K_L \rightarrow \pi^0 \pi^+ \pi^-$  decay as a normalization mode, because the only difference from the  $K_L \rightarrow \pi^0 \mu^+ \mu^-$  is the charged particles. In order to cancel systematic errors, most of the requirements for  $K_L \rightarrow \pi^0 \pi^+ \pi^-$  were set the same as  $K_L \rightarrow \pi^0 \mu^+ \mu^-$ . Here, we list the differences from the  $K_L \rightarrow \pi^0 \mu^+ \mu^-$  analysis.

- When calculating the kinematic variables,  $\pi^\pm$  mass was used for the charged particle.
- We required the energy measured by the calorimeter divided the momentum (EOP) to be less than 0.9 to reject electrons and select  $\pi^\pm$ .
- We did not require hits in the Mu3 banks.
- We did not cut on  $P_{\pi^0}^2$  for  $K_L \rightarrow \pi^0 \pi^+ \pi^-$ . The other requirements for kinematic variables (kaon mass,  $\pi^0$ , and  $P_T^2$ ) are the same as  $\pi^0 \mu^+ \mu^-$ .

For most of the variables, the MC distribution agreed with data distribution as shown in Figure 4.13. Figure 4.14 shows the reconstructed  $\pi^0$  mass and the

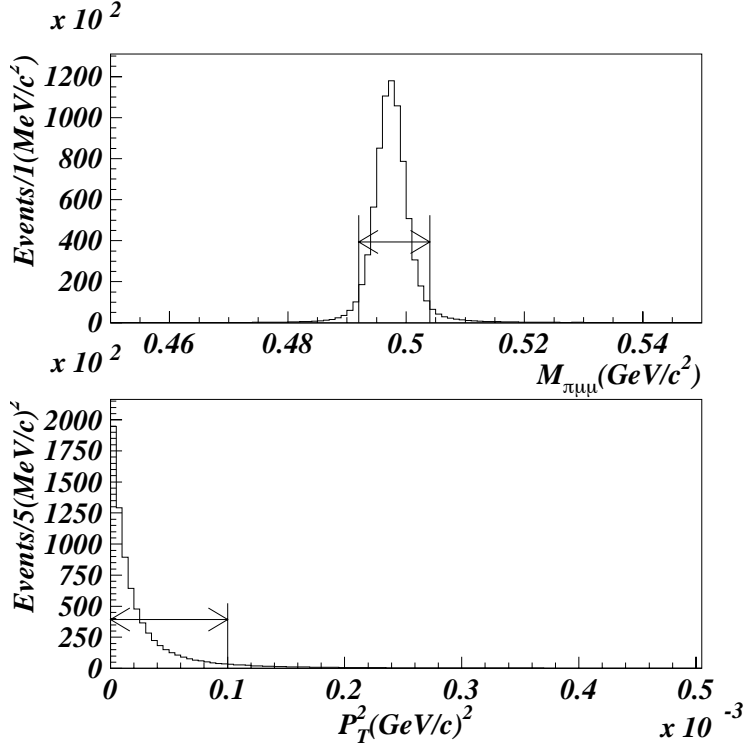


Figure 4.10: The upper plot shows the reconstructed  $\pi^0\mu^+\mu^-$  mass distribution. The lower plot shows  $P_T^2$  of  $K_L \rightarrow \pi^0\mu^+\mu^-$  MC events after the event reconstruction. The arrow in these plots shows our requirement. ( $492 < M_{\pi^0\mu^+\mu^-} \text{ MeV}/c^2 < 504$ ,  $P_T^2 < 100(\text{MeV}/c)^2$ )

distribution of the  $\chi_{vertex}^2$ . The  $\pi^0$  distribution of MC is shifted and wider than data.

The detector acceptance for  $K_L \rightarrow \pi^0\pi^+\pi^-$  is calculated to be 8.08%. The background to the normalization sample is negligible. Using the number of observed events (= 377919), prescale factor, the acceptance, and  $\text{BR}(K_L \rightarrow \pi^0\pi^+\pi^-)$ , the number of  $K_L$  which decayed between 90m and 160m from the target and have primary energy between 20GeV and 220GeV is found to be 2.68E11.

## 4.8 Sensitivity for $K_L \rightarrow \pi^0\mu^+\mu^-$

Table 4.2 is a list of the analysis cuts described in previous sections and the efficiencies for the  $K_L \rightarrow \pi^0\mu^+\mu^-$  MC events at each stage. The acceptance for the  $K_L \rightarrow \pi^0\mu^+\mu^-$  after the corrections is 5.0%.

The sensitivity for  $K_L \rightarrow \pi^0\mu^+\mu^-$  in this experiment was defined by the

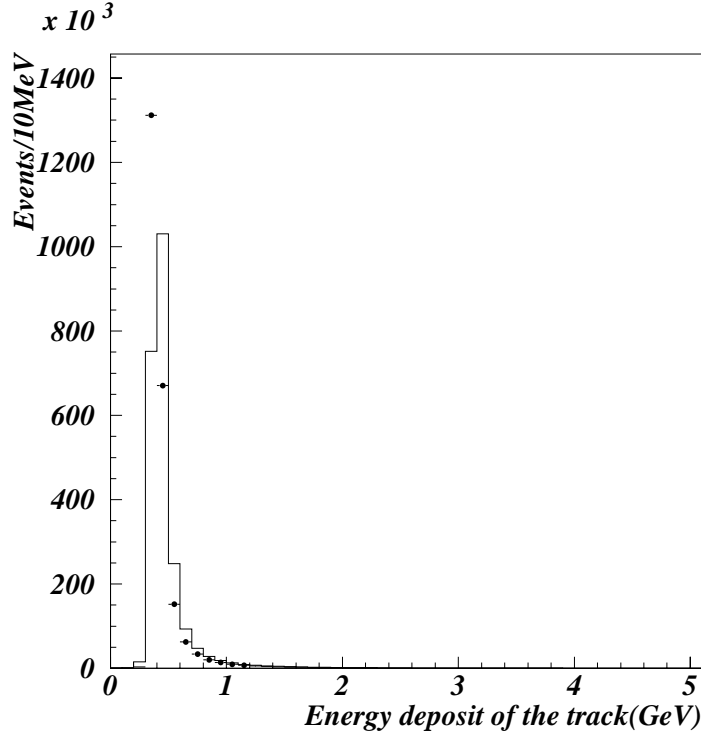


Figure 4.11: The muon energy deposit in the CsI calorimeter. The solid line(dot) shows the energy deposit by muon in MC sample(data).

single event sensitivity expressed as

$$SES(K_L \rightarrow \pi^0 \mu^+ \mu^-) = \frac{1}{Flux \times A(K_L \rightarrow \pi^0 \mu^+ \mu^-)}, \quad (4.4)$$

where  $Flux$  is the number of  $K_L$  decays which was calculated by counting  $K_L \rightarrow \pi^0 \pi^+ \pi^-$  event, and  $A(K_L \rightarrow \pi^0 \mu^+ \mu^-)$  is the acceptance for the  $K_L \rightarrow \pi^0 \mu^+ \mu^-$  event. Our single event sensitivity is

$$S.E.S.(K_L \rightarrow \pi^0 \mu^+ \mu^-) = 7.46 \times 10^{-11}.$$

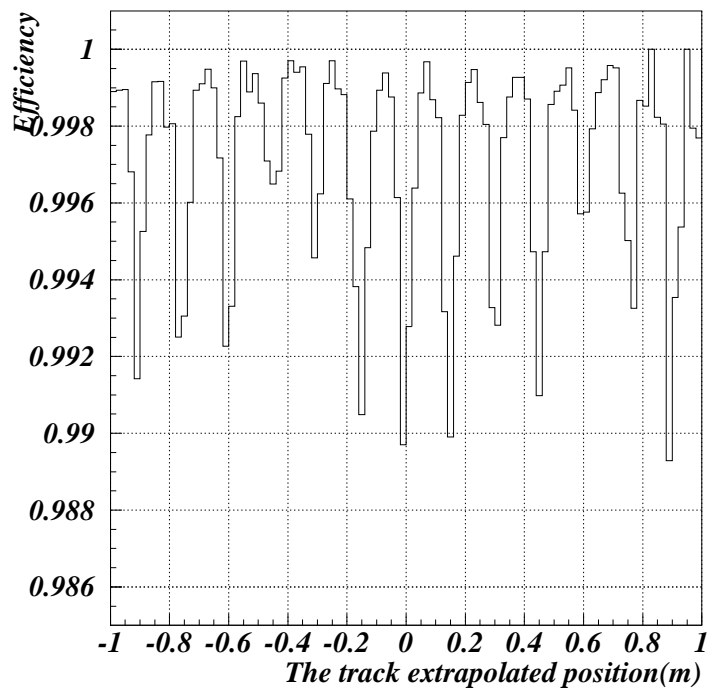


Figure 4.12: The detection efficiency of MU3 bank for muons as a function of the extrapolated track position at MU3x bank. The muons were selected to have momentum to be greater than  $40\text{GeV}/c$ .

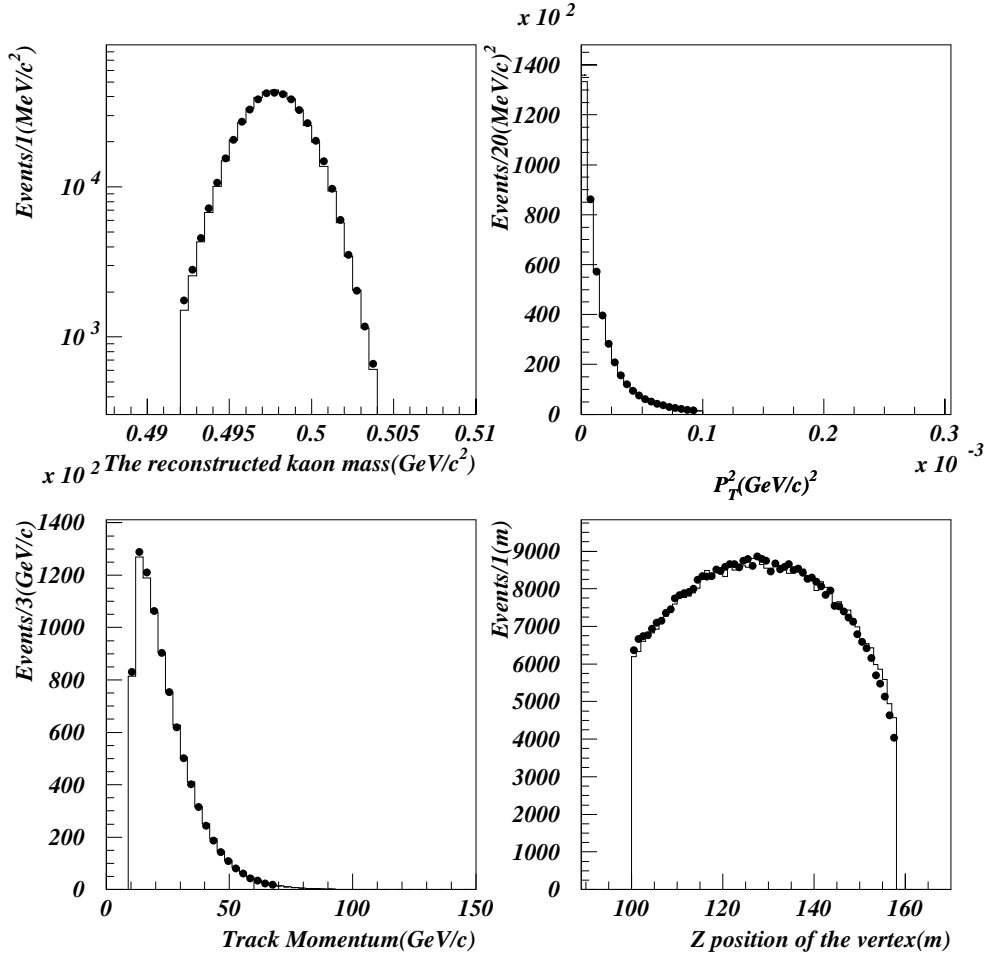


Figure 4.13: The top left(right) plot shows the kaon mass( $P_T^2$ ) distribution of  $K_L \rightarrow \pi^0 \pi^+ \pi^-$  MC events and data after all cuts. The bottom left plot shows the momentum distribution of the track in the  $K_L \rightarrow \pi^0 \pi^+ \pi^-$  events. The bottom right plot shows the vertex z position. Dots represent the distribution of the observed events. Open histogram shows that of MC events. The MC distribution was normalized by the measured number of decayed  $K_L$ .

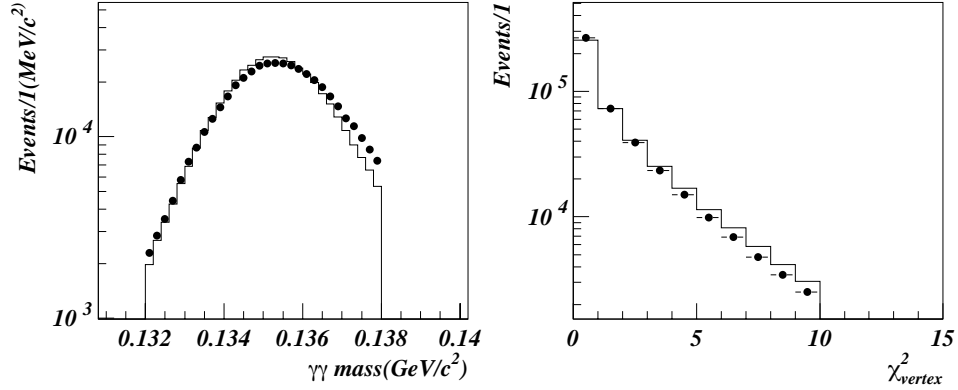


Figure 4.14: The left plot shows  $\gamma\gamma$  mass distribution of data(dot) and MC(open histogram) of the accepted  $K_L \rightarrow \pi^0\pi^+\pi^-$  events as normalization. The right plot shows  $\chi_{vertex}^2$  distribution of data(dot) and MC(open histogram).

Cut	$K_L \rightarrow \pi^0\mu^+\mu^-$ MC
Level 1,2	24.8%
Level 3	80.6%
Event Reconstruction	68.7%
no Veto hits in RC,SA,CIA	98.5%
Muon energy	93.5%
2 photon cluster	72.4%
Muon momentum	75.0%
$\pi^0$ mass	95.2%
$M_{\mu\mu}$	93.7%
$P_{\pi^0}^2$	89.2%
$P_T^2$	92.0%
Kaon mass	97.7%
Kaon momentum	100.0%
energy deposit correction	+3.3%
MU3 efficiency correction	-1.2%
Acceptance for $K_L \rightarrow \pi^0\mu^+\mu^-$	5.0%

Table 4.2: Analysis cuts and efficiencies for  $K_L \rightarrow \pi^0\mu^+\mu^-$ .

# Chapter 5

## Background Estimation

Before analyzing the masked region, we will describe the correction for the estimated number of background events in the signal region and the consistency between data and background MC.

### 5.1 Number of Background Events

We analyzed all the background decay modes as described in Chapter 4. Table 5.1 summarizes the number of expected background events for each background decay. The total number of expected background events is 0.93. The largest background is  $K_L \rightarrow \mu^+ \mu^- \gamma \gamma$ .\*

decay mode	option	#events
$K_L \rightarrow \mu^+ \mu^- \gamma \gamma$		0.463
$K_L \rightarrow \mu^+ \mu^- \gamma$		<0.0110
$K_L \rightarrow \pi^0 \pi^+ \pi^-$	DD	0.236
$K_L \rightarrow \pi^0 \pi^+ \pi^-$	DP	0.00557
$K_L \rightarrow \pi^0 \pi^+ \pi^-$	PP	0.00684
$K_L \rightarrow \pi^\pm \mu^\mp \nu(\bar{\nu})$	D	0.156
$K_L \rightarrow \pi^\pm \mu^\mp \nu(\bar{\nu})$	P	0.0543
$K_L \rightarrow \pi^0 \pi^\pm \mu^\mp \nu$	D	0.00825
$K_L \rightarrow \pi^0 \pi^\pm \mu^\mp \nu$	P	<0.0413
$K_L \rightarrow \pi^+ \pi^- \gamma$	all	negligible
$K_L \rightarrow \pi^+ \pi^-$	all	negligible
Total		0.930

Table 5.1: Summary of the expected number of events from various background sources. D represents a  $\pi^\pm$  decayed in flight before CsI calorimeter. P denotes that a  $\pi^\pm$  punched through the muon filter.

---

\*For calculating the expected number of  $K_L \rightarrow \mu^+ \mu^- \gamma \gamma$  events, we used  $\text{Br}(K_L \rightarrow \mu^+ \mu^- \gamma \gamma, E^* > 10 \text{MeV}) = (1.55 \pm 0.75) \times 10^{-9}$  which was measured in Appendix A.

## 5.2 Correction for Background Estimation

As described in Chapter 3, we generated the background decays which include  $\pi^\pm$  by using two special techniques to simulate  $\pi^\pm$  decay and  $\pi^\pm$  punch through. However, as shown in Figure 3.2, the  $\pi^\pm$  which were generated by MC have a smaller probability of being misidentified as muons. This discrepancy can underestimate the number of background events in the signal region. In order to correct for the effect of this discrepancy, the event weight of the  $\pi^\pm$  in the momentum range 10-15(15-20)GeV/c was increased by 17%(6.48%) for each  $\pi^\pm$ . Only the remaining background events of  $K_L \rightarrow \pi^0 \pi^+ \pi^-$  and  $K_L \rightarrow \pi^\pm \mu^\mp \nu(\bar{\nu})$  decays had  $\pi^\pm$  with the momentum below 20 GeV/c. The size of the correction for each background is summarized in Table 5.2.

mode	option	Size of the Correction(%)
$K_L \rightarrow \pi^0 \pi^+ \pi^-$	DD	+ 6.70
$K_L \rightarrow \pi^0 \pi^+ \pi^-$	DP	+ 17.2
$K_L \rightarrow \pi^0 \pi^+ \pi^-$	PP	+ 6.48
$K_L \rightarrow \pi^\pm \mu^\mp \nu(\bar{\nu})$	D	+2.9
$K_L \rightarrow \pi^\pm \mu^\mp \nu(\bar{\nu})$	P	+13.3

Table 5.2: The summary of the correction for the misidentification. D represented a  $\pi^\pm$  decayed in flight before CsI calorimeter. P meant that a  $\pi^\pm$  punched through the muon filters.

## 5.3 Uncertainty of Background Estimation

The estimated number of background events was a product of three components: the number of decayed parent particles, branching ratio, and acceptance. This section will describe the contributions from each component to the uncertainties in the background estimation.

### 5.3.1 Branching Ratio

The Particle Data Group's[4] branching ratios were used to estimate the number of the background events in the signal region. We used our measured branching ratio;  $Br(K_L \rightarrow \mu^+ \mu^- \gamma \gamma, E^* > 10 MeV) = (1.55 \pm 0.75) \times 10^{-9}$ , as described in Appendix A. Table 5.3 lists the uncertainties in the branching ratios for all the background decays. We assigned the uncertainty in the branching ratio of  $K^+ \rightarrow \pi^+ \pi^- \mu^+ \nu$  to the uncertainty in the branching ratio for  $K_L \rightarrow \pi^0 \pi^\pm \mu^\mp \nu$ .

mode	Uncertainty(%)
$K_L \rightarrow \mu^+ \mu^- \gamma \gamma$	48.2
$K_L \rightarrow \pi^0 \pi^+ \pi^-$	1.59
$K_L \rightarrow \pi^\pm \mu^\mp \nu(\bar{\nu})$	0.920
$K_L \rightarrow \pi^0 \pi^\pm \mu^\mp \nu$	64.2

Table 5.3: The summary of the uncertainties in the branching ratio of the background decays.

### 5.3.2 Monte Carlo Statistics

Another important systematic error comes from the statistics of the MC events.  $K_L \rightarrow \mu^+ \mu^- \gamma \gamma$  and all decay modes which include  $\pi^\pm$  were generated with the weight ( $w_i$ ) for event by event. In a case that each event has its own weight, the effective number of events is formulated as:

$$n_{eff} = \frac{T^2}{\delta^2} = (\sum w_i)^2 / \sum w_j^2,$$

where  $T$  is the number of accepted events and  $\delta$  is the related error to  $T$ [32]. The statistics error of the generated events,  $\delta/T = \sqrt{\sum w^2} / \sum w$ , was taken as the systematic error of the MC events. The statistical uncertainty for accepted events in the final analysis is summarized in Table 5.4.

mode	option	#Accepted events	Uncertainty(%)
$K_L \rightarrow \mu^+ \mu^- \gamma \gamma$		1582	1.98%
$K_L \rightarrow \pi^0 \pi^+ \pi^-$	DD	7	47.2%
$K_L \rightarrow \pi^0 \pi^+ \pi^-$	DP	1	100%
$K_L \rightarrow \pi^0 \pi^+ \pi^-$	PP	1	100%
$K_L \rightarrow \pi^\pm \mu^\mp \nu(\bar{\nu})$	D	3	62.5%
$K_L \rightarrow \pi^\pm \mu^\mp \nu(\bar{\nu})$	P	3	58.1%
$K_L \rightarrow \pi^0 \pi^\pm \mu^\mp \nu$	D	1	100%

Table 5.4: The summary of the uncertainties from MC statistics for the background decays to  $K_L \rightarrow \pi^0 \mu^+ \mu^-$ . D represented a  $\pi^\pm$  decayed in flight before the CsI calorimeter. P meant that a  $\pi^\pm$  punched through the muon filters.

### 5.3.3 Statistical error on the number of $K_L$ decays

The statistical error which is related to the number of  $K_L$  decays come from the number of observed  $K_L \rightarrow \pi^0 \pi^+ \pi^-$  events and the number of accepted  $K_L \rightarrow \pi^0 \pi^+ \pi^-$  MC events which was used to calculate its acceptance.

The number of observed  $K_L \rightarrow \pi^0 \pi^+ \pi^-$  for the normalization is 377919. The number of observed  $K_L \rightarrow \pi^0 \pi^+ \pi^-$  led to an uncertainty of 0.163% and

the number of the accepted  $K_L \rightarrow \pi^0 \pi^+ \pi^-$  MC events led to an error of 0.150%. The quadratic sum of the two sources is 0.222%.

### 5.3.4 Summary of Background Estimation

The number of background events in the signal region estimated by MC was  $0.96 \pm 0.34$  after the correction as listed in Table 5.5. The biggest contribution came from  $K_L \rightarrow \mu^+ \mu^- \gamma \gamma$  decay.

decay mode	option	$\frac{\#MC\text{events}}{\text{decayed } K_L}$	#events
$K_L \rightarrow \mu^+ \mu^- \gamma \gamma$		2.4E4	$0.463 \pm 0.222$
$K_L \rightarrow \mu^+ \mu^- \gamma + \gamma_{acc}$		85.2	$< 0.0230 (90\% \text{ C.L.})$
$K_L \rightarrow \pi^0 \pi^+ \pi^-$	DD	17.9	$0.252 \pm 0.0952$
$K_L \rightarrow \pi^0 \pi^+ \pi^-$	DP	94.1	$0.00653 \pm 0.00653$
$K_L \rightarrow \pi^0 \pi^+ \pi^-$	PP	94.8	$0.00728 \pm 0.00728$
$K_L \rightarrow \pi^\pm \mu^\mp \nu(\bar{\nu}) + 2\gamma_{acc}$	D	27.7	$0.161 \pm 0.0928$
$K_L \rightarrow \pi^\pm \mu^\mp \nu(\bar{\nu}) + 2\gamma_{acc}$	P	52.0	$0.0634 \pm 0.0366$
$K_L \rightarrow \pi^0 \pi^\pm \mu^\mp \nu$	D	220	$0.00934 \pm 0.00981$
$K_L \rightarrow \pi^0 \pi^\pm \mu^\mp \nu$	P	242	$< 0.0949 (90\% \text{ C.L.})$
$K_L \rightarrow \pi^+ \pi^- \gamma + \gamma_{acc}$	all	989	negligible
$K_L \rightarrow \pi^+ \pi^- + 2\gamma_{acc}$	all	1268	negligible
Total			$0.96 \pm 0.34$

Table 5.5: Summary of the number of the events from various background sources with their uncertainties after the correction. D represented a  $\pi^\pm$  decayed in flight before the CsI calorimeter. P represented a  $\pi^\pm$  punched through the muon filter.

## 5.4 Consistency between Data and MC

We estimated the number of background events which passed all the  $K_L \rightarrow \pi^0 \mu^+ \mu^-$  requirements. In order to confirm our understanding of the background, we will compare the background MC events and data.

### 5.4.1 Comparison of the Shape of the Distribution.

Figure 5.1 shows kinematic variables of the background MC and masked data. In these distributions, the number of MC events was absolutely normalized by the measured number of  $K_L$  decays. Any discrepancy in the distributions between data and MC would suggest an existence of an unknown background source and/or a wrong estimation of the background level.

In Figure 5.1 (A), the reconstructed kaon mass distribution in the masked data is compared with MC. The requirement for this plot include all the requirements for  $K_L \rightarrow \pi^0 \mu^+ \mu^-$  except for the kaon mass. The peak in  $0.48 >$

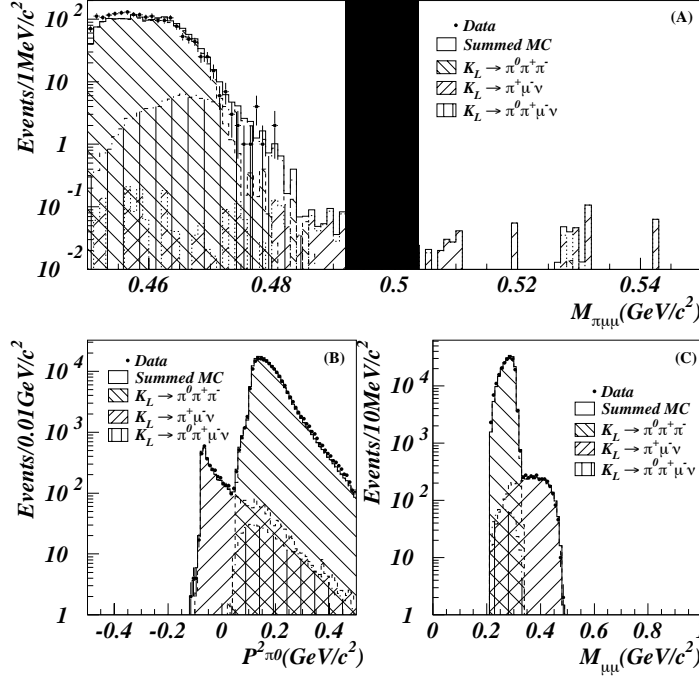


Figure 5.1: The plot (A) shows the kaon mass distribution with all requirements except for kaon mass. The plot (B) shows the  $P_{\pi^0}^2$  distribution without kinematic requirements. The plot (C) shows  $M_{\mu\mu}$  distribution after the particle identification. The dots represent data, open histogram represent the summed MC.

$M_{\pi^0\mu^+\mu^-}$  consists of  $K_L \rightarrow \pi^0\pi^+\pi^-$ ,  $K_L \rightarrow \pi^0\pi^\pm\mu^\mp\nu$ , and  $K_L \rightarrow \pi^\pm\mu^\mp\nu(\bar{\nu})$ . The entire shape is in a good agreement.

Figure 5.1(B) and (C) show the  $P_{\pi^0}^2$  and  $M_{\mu\mu}$  distribution of the masked data and summed MC, respectively, without kinematic requirements. In Figure 5.1(B), the peak at  $P_{\pi^0}^2 = -0.09(0.2)(GeV/c)^2$  consists of  $K_L \rightarrow \pi^\pm\mu^\mp\nu(\bar{\nu})(K_L \rightarrow \pi^0\pi^+\pi^-)$ . In Figure 5.1(C), the distribution around  $0.4GeV/c^2$  consists of  $K_L \rightarrow \pi^\pm\mu^\mp\nu(\bar{\nu})$  and the peak at  $M_{\mu\mu} = 0.3GeV/c^2$  consists of  $K_L \rightarrow \pi^\pm\mu^\mp\nu(\bar{\nu})$ ,  $K_L \rightarrow \pi^0\pi^+\pi^-$ , and  $K_L \rightarrow \pi^0\pi^\pm\mu^\mp\nu$ . Most of the  $K_L \rightarrow \pi^0\mu^+\mu^-$  trigger events were  $K_L \rightarrow \pi^\pm\mu^\mp\nu(\bar{\nu})$  and  $K_L \rightarrow \pi^0\pi^+\pi^-$  with mis-identified  $\pi^\pm$ . The agreement between data and MC in Figure 5.1(B) and (C) shows that backgrounds from  $K_L \rightarrow \pi^\pm\mu^\mp\nu(\bar{\nu})$  and  $K_L \rightarrow \pi^0\pi^+\pi^-$  are reproduced well.

## 5.4.2 Comparisons in Side Bands

In the previous section, we showed our understanding for the sources of backgrounds. In this section, we will compare the number of background events in

the side band region in the reconstructed mass and  $P_T^2$  distributions between data and MC.

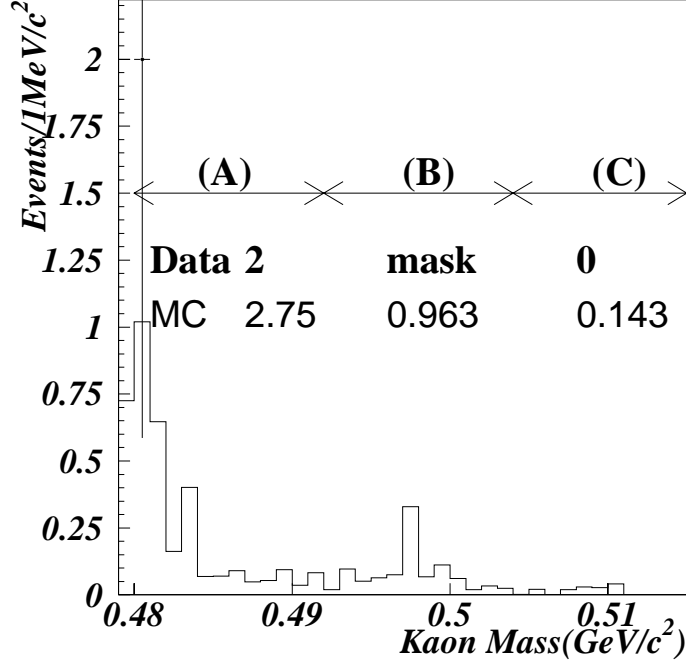


Figure 5.2: The kaon mass distribution in the  $P_T^2 < 100(\text{MeV}/c)^2$  region. The dot indicates the data. The open histogram represents the summed MC.

Figure 5.2 shows the reconstructed kaon mass distribution with all the cuts except for kaon mass cut. In the region (A) ( $0.48 < M_{\pi^0\mu^+\mu^-} (\text{GeV}/c^2) < 0.492$ ), there are 2 events in data, while MC predicted  $2.75 \pm 0.73$  events. These events are dominated by  $K_L \rightarrow \pi^0\pi^+\pi^-$  and  $K_L \rightarrow \pi^0\pi^\pm\mu^\mp\nu$ . In region (C) ( $0.504 < M_{\pi^0\mu^+\mu^-} (\text{GeV}/c^2) < 0.515$ ), there are no events left in data, while MC predicted  $0.14 \pm 0.081$  events, all from  $K_L \rightarrow \pi^\pm\mu^\mp\nu(\bar{\nu}) + 2\gamma_{acc}$ . In both regions (A) and (C), the observed number of events are consistent with background MC. The region (B) is the signal region for the  $K_L \rightarrow \pi^0\mu^+\mu^-$ , and events in data are still being masked. The peak in background MC is due to  $K_L \rightarrow \mu^+\mu^-\gamma\gamma$ .

Figure 5.3 shows the  $P_T^2$  distribution with all the cuts except for  $P_T^2$  cut. There are 2 events in region (B) ( $0.0001 < P_T^2 (\text{GeV}/c)^2 < 0.0005$ ) and (C) ( $0.0005 < P_T^2 (\text{GeV}/c)^2 < 0.001$ ), respectively. The MC predicts consistent number of background events;  $2.56 \pm 1.53$  events in region (B) and  $2.80 \pm 2.59$  events in region (C). The events in region (B) and (C) are dominated by  $K_L \rightarrow \pi^0\pi^+\pi^-$  and  $K_L \rightarrow \pi^\pm\mu^\mp\nu(\bar{\nu}) + 2\gamma_{acc}$ , and these background are predicted to have  $0.963 \pm 0.335$  events in the signal region (A) ( $P_T^2 < 0.0001$ ). In addition, we expect  $0.463 \pm 0.222$  events from  $K_L \rightarrow \mu^+\mu^-\gamma\gamma$  decay, which are peaked at  $P_T^2 = 0$ .

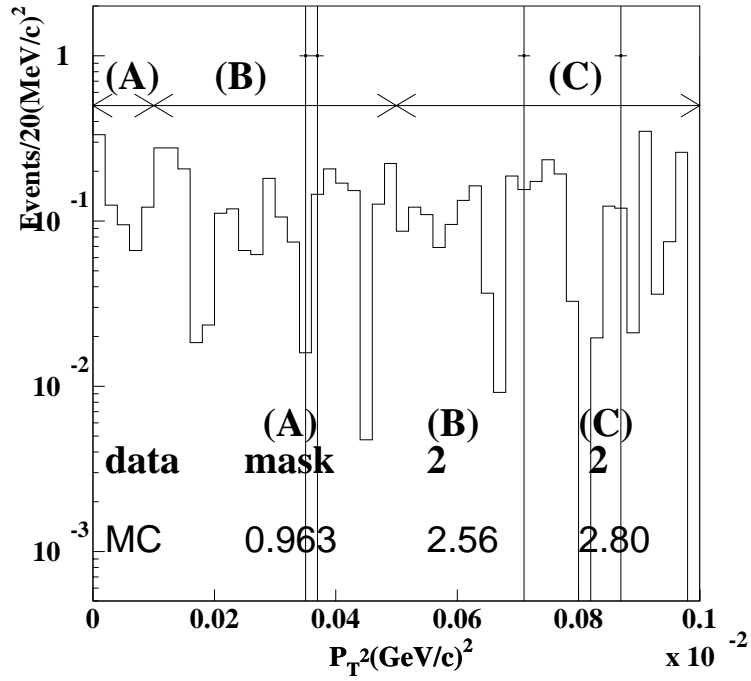


Figure 5.3: The  $P_T^2$  distribution in the kaon mass region. The dots indicate data. The open histogram represents the summed MC.

### 5.4.3 Summary

We conclude that the sources of background are well understood, and the shape of each source is correctly reproduced in MC. The number of background events in the side band region are well reproduced.

# Chapter 6

## Systematic Uncertainties on the Sensitivity

We will describe the systematic uncertainties on the single event sensitivity in this section. The uncertainty can come from the branching ratio, the statistical uncertainty, energy and momentum measurement, the  $\pi^0$  and  $\chi^2_{vertex}$  distributions, the chamber inefficiency, the particle identification, and the trigger difference.

### 6.1 Branching Ratio

The number of the kaon decays in the fiducial area was derived from the number of observed  $K_L \rightarrow \pi^0\pi^+\pi^-$  decays. The calculation used the branching ratio of  $K_L \rightarrow \pi^0\pi^+\pi^-$  by the Particle Data Group[4], which has an uncertainty of 1.59% of itself.

### 6.2 Statistical Uncertainty

We observed 377919  $K_L \rightarrow \pi^0\pi^+\pi^-$  events after all the cuts. This gives a statistical uncertainty on the single event sensitivity of 0.150%. There are uncertainties from the number of generated MC events which were used to calculate the acceptance of  $K_L \rightarrow \pi^0\mu^+\mu^-$  and its normalization decay,  $K_L \rightarrow \pi^0\pi^+\pi^-$ . These uncertainties, summarized in Table 6.1, were included into the systematic uncertainty.

	#generated MC events	Acceptance	Stat. Error
$K_L \rightarrow \pi^0\mu^+\mu^-$	$7.51 \times 10^6$	$4.90 \pm 0.00806\%$	0.165%
$K_L \rightarrow \pi^0\pi^+\pi^-$	$5.42 \times 10^6$	$8.15 \pm 0.0124\%$	0.152%

Table 6.1: Systematic uncertainty from the number of generated MC.

## 6.3 Energy Measurement

There are discrepancies between the expected performance and the actual performance of the CsI calorimeter. The energy measurement by the CsI calorimeter was used to identify particles and to calculate the kinematic variables such as an invariant mass. Therefore, a mismeasurement of energy with the CsI calorimeter may shift an acceptance ratio which is defined by

$$Acceptance\ Ratio = \frac{A(K_L \rightarrow \pi^0 \mu^+ \mu^-)}{A(K_L \rightarrow \pi^0 \pi^+ \pi^-)}, \quad (6.1)$$

where  $A(K_L \rightarrow \pi^0 \mu^+ \mu^-)$  and  $A(K_L \rightarrow \pi^0 \pi^+ \pi^-)$  are acceptance of  $K_L \rightarrow \pi^0 \mu^+ \mu^-$  and  $K_L \rightarrow \pi^0 \pi^+ \pi^-$ , respectively.

MC change	Acceptance ratio variation
Cluster Energy shifted by 0.7%	+3.294%
Cluster Energy smeared by 0.3%	-0.206%
Inner crystal Energy shifted by 1.0%	+0.0364%
Inner crystal Energy smeared by 0.9%	-0.178%

Table 6.2: Summary of systematic error studies on the energy measurement.

Table 6.2 lists various changes that were made on Monte Carlo events, and the effect that these changes had on the acceptance ratio. The magnitude of intentional shift or smearing were determined from data by investigating the  $E/p$  distribution obtained run-by-run. Approximately, the maximum variation found in the data was used for the artificial tweaking. By adding each error in a quadrature, the total uncertainty due to the energy measurement in the acceptance ratio was determined to be 3.30%.

## 6.4 Momentum measurement

A misunderstanding of the momentum measurement can also introduce an error in the acceptance ratio.

In order to find out how well we understand the momentum measurement, we used  $K_L \rightarrow \pi^+ \pi^-$ , because its mass reconstruction only uses the spectrometer information. The observed  $K_L \rightarrow \pi^+ \pi^-$  had a mass of  $497.59\text{ MeV}/c^2$  with a width of  $2.635\text{ MeV}/c^2$ , where Monte Carlo events had the mass of  $497.64\text{ MeV}/c^2$  with a width of  $2.383\text{ MeV}/c^2$ . Therefore, shifts in the acceptance ratio were calculated by changing the momentum and the resolution of Monte Carlo events to match the data  $\pi^+ \pi^-$  mass distribution. Table 6.3 summarizes study results. We assigned the quadratic sum of acceptance ratio shifts, 1.12%, as the uncertainty in the acceptance ratio due to the momentum measurement.

MC change	Acceptance Ratio variation
Momentum scale shifted by 0.30%	-0.727%
Momentum resolution smeared by 0.53%	+0.852%

Table 6.3: Summary of systematic uncertainties on the momentum measurement.

## 6.5 $\chi_{vertex}^2$ and $\pi^0$ mass

The discrepancy of  $\chi_{vertex}^2$  and  $\pi^0$  mass distributions between data and MC, as shown in Figure 4.14, could change the acceptance ratio.

The  $\chi_{vertex}^2$  was calculated at the vertex finding. The right plot in Figure 4.14 shows the  $\chi_{vertex}^2$  distributions for the  $K_L \rightarrow \pi^0\pi^+\pi^-$  for data and Monte Carlo. We required  $\chi_{vertex}^2 < 10$  in both  $K_L \rightarrow \pi^0\mu^+\mu^-$  and  $K_L \rightarrow \pi^0\pi^+\pi^-$  analyses. The mismatch in  $\chi_{vertex}^2$  distribution between data and MC shows that we overestimate the acceptance for  $K_L \rightarrow \pi^0\pi^+\pi^-$ . This effect almost cancels between the signal and normalization mode, since  $\chi_{vertex}^2$  distribution are similar between them. The  $\chi_{vertex}^2$  width of  $K_L \rightarrow \pi^0\pi^+\pi^-$  MC is 12% wider than data. Therefore, we scaled the  $\chi_{vertex}^2$  value by 12% before the cut, and found that the acceptance ratio changes by -0.217%.

The  $\pi^0$  mass was calculated by using the vertex position and photon energies. The left plot in Figure 4.14 shows the  $\pi^0$  mass ( $M_{\gamma\gamma}$ ) distribution for the  $K_L \rightarrow \pi^0\pi^+\pi^-$ . We required  $132 < M_{\gamma\gamma}(MeV/c^2) < 138$  in both  $K_L \rightarrow \pi^0\mu^+\mu^-$  and  $K_L \rightarrow \pi^0\pi^+\pi^-$  analyses. We shifted  $M_{\gamma\gamma}$  by 0.15  $MeV/c^2$  and smeared the width by 0.4% to match the shapes and found that the acceptance ratio changes by +0.483%.

## 6.6 Inefficiency of Drift Chamber

Our MC simulated the inefficiency of the drift chamber by randomly neglecting the chamber hits. The inefficiency in all region except for beam region agreed with data. However, the region where neutral beam passed through had extra 5% inefficiency. The SOD distribution have a long tail in the region because the gain in the beam region was lower than that in the other region. However, the long tail was not well reproduced in MC. The tracking efficiency was sensitive to the SOD distribution by the requirement on the SOD in the tracking algorithm. Figure 6.1 shows the illumination of the tracks at the first drift chamber. There is a large difference in the beam regions ( $-0.1m \sim -0.2m$ ,  $0.1m \sim 0.2m$ ). The small discrepancy in the Z distribution of the  $K_L \rightarrow \pi^0\pi^+\pi^-$  between data and MC at 150-160m shown in Figure 4.13 is explained by having two tracks in this beam region.

In order to estimate the uncertainty from this inefficiency, we added extra 5% inefficiency to the wires in the beam region for the upstream chambers in MC, and found that the acceptance ratio changed by +0.149%.

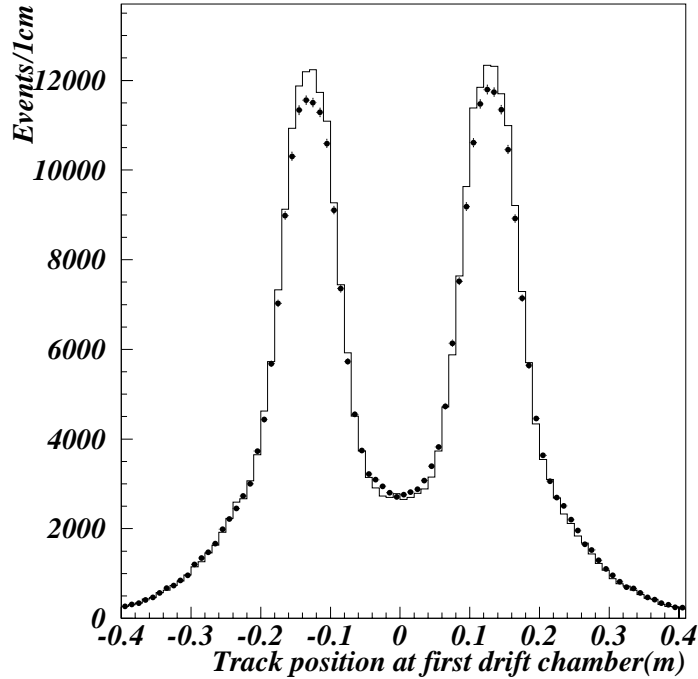


Figure 6.1: The illumination of the tracks at the first drift chamber.

## 6.7 Particle Identification

The charged particles in the final states are different between  $K_L \rightarrow \pi^0 \mu^+ \mu^-$  and  $K_L \rightarrow \pi^0 \pi^+ \pi^-$ . The difference in the analyses for the two decay modes was a particle identification. In order to know the effect of the difference, we calculated the number of kaon decays by analyzing  $K_L \rightarrow \pi^\pm \mu^\mp \nu(\bar{\nu})$  events which have one muon, and compared the number with that by  $K_L \rightarrow \pi^0 \pi^+ \pi^-$  which has only  $\pi^\pm$ . The analysis for  $K_L \rightarrow \pi^\pm \mu^\mp \nu(\bar{\nu})$  included muon identification which was used for  $K_L \rightarrow \pi^0 \mu^+ \mu^-$  analysis. The calculated number of kaon decays was 2.10% lower than the number based on  $K_L \rightarrow \pi^0 \pi^+ \pi^-$ . We assigned an uncertainty in the acceptance ratio due to the particle identification as 4.20%, because  $K_L \rightarrow \pi^0 \mu^+ \mu^-$  decay has two muons.

## 6.8 Different trigger Uncertainty

We used different triggers for the signal and normalization analysis. In order to find any possible bias due to trigger difference, we applied all the Level 1,2,3 requirements for the  $K_L \rightarrow \pi^0 \mu^+ \mu^-$  trigger on the  $K_L \rightarrow \pi^0 \pi^+ \pi^-$  trigger events. The number of  $K_L \rightarrow \pi^0 \pi^+ \pi^-$  trigger events after Level 1,2,3 requirements and a correction for a prescale factor, and the number of  $K_L \rightarrow \pi^0 \mu^+ \mu^-$

trigger events differed by 0.802%.

## 6.9 Summary

Table 6.4 summarizes all the systematic uncertainties on the single event sensitivity. Each uncertainty have less than 10% uncertainty. By summing each uncertainty quadratically, we obtained the overall uncertainty of 5.77%.

Source of Uncertainty	(%)
BR( $K_L \rightarrow \pi^0 \pi^+ \pi^-$ )	1.59
Energy measurement	3.30
Momentum measurement	1.12
$\chi^2_{vertex}$	0.217
$\pi^0$ mass	0.483
chamber inefficiency	0.149
Particle identification	4.20
trigger difference	0.802
Total Systematic uncertainty	5.77

Table 6.4: The systematic error on the single event sensitivity from each source.

# Chapter 7

## Result and Discussion

We described the requirements for selecting  $K_L \rightarrow \pi^0 \mu^+ \mu^-$  and estimation of the number of the background events in the signal region. In this chapter, we will open the masked region and present our result on the branching ratio.

### 7.1 Criteria for claiming the observation of $K_L \rightarrow \pi^0 \mu^+ \mu^-$

Before opening the masked region, we should decide the criteria for claiming a signal. Based on the background studies described in Chapter 5, we expect  $0.96 \pm 0.34$  background events in the masked region ( $0.492 < M_{\pi^0 \mu^+ \mu^-} \text{ GeV}/c^2 < 0.504$ ,  $P_T^2 (\text{MeV}/c)^2 < 100$ ). Table 7.1 shows the Poisson distribution of the number of background events we expect to see.

#Expected Events	Poisson Prob.
0	0.398
1	0.367
2	0.169
3	0.0520
4	0.0120
5	0.00221
6	0.000339

Table 7.1: Poisson distribution of the expected number of background events while 0.96 events are expected.

Usually, we require more than  $3\sigma$  significance to claim a new discovery. This means that the probability of making an error should be less than 0.3%, based on the Gaussian distribution. In our case, this corresponds to the probability of observing 5 or more events. Therefore, if we find 5 or more events in the signal region, we will claim the discovery of  $K_L \rightarrow \pi^0 \mu^+ \mu^-$ .

## 7.2 Analysis of data in the Masked Region

We have been analyzing data by masking events in the signal region to avoid any possible bias. Let us now analyze the data inside the masked region.

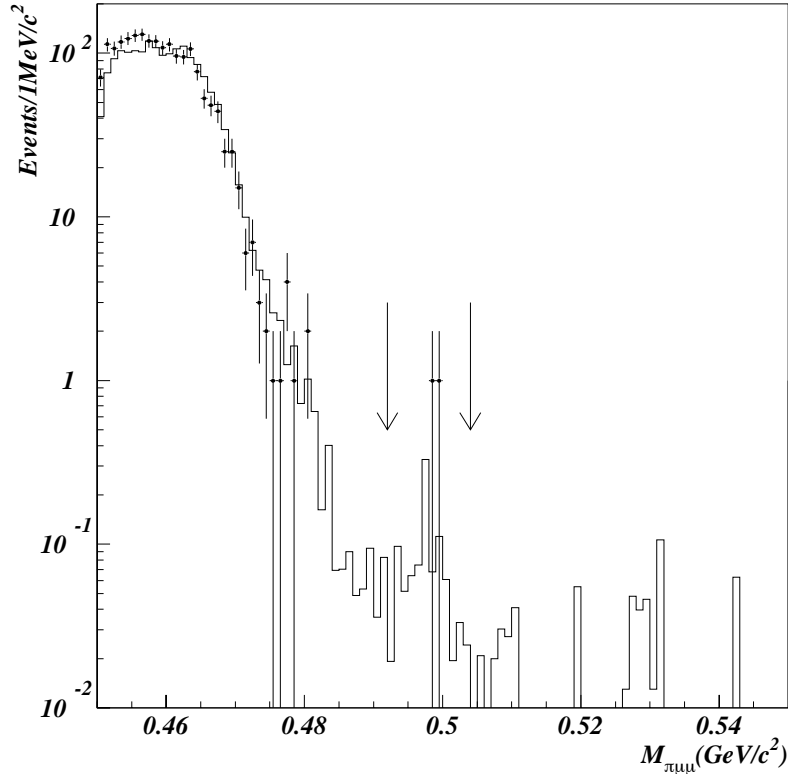


Figure 7.1: The reconstructed  $\pi^0\mu^+\mu^-$  mass distribution with all the cuts except for the mass cut. There are two events in the masked region. Dots are data. Open histogram is sum of all background MC events.

Figure 7.1 shows the reconstructed kaon mass distribution with all the cuts except for the kaon mass cut. There are two events in the signal region.

## 7.3 Result

In Chapter 6, we determined the single event sensitivity of  $K_L \rightarrow \pi^0\mu^+\mu^-$  in this experiment to be

$$SES(K_L \rightarrow \pi^0\mu^+\mu^-) = [7.5 \pm 0.011(stat.) \pm 0.43(sys.)] \times 10^{-11}.$$

In Section 5, we estimated that there are  $0.96 \pm 0.34$  background events in the signal region. As discussed in Section 7.1, we need at least 5 events to claim a discovery of  $K_L \rightarrow \pi^0\mu^+\mu^-$ .

We observed 2 events in the masked region. These 2 events are not significant excess for the discovery. We regard the observation as consistent with background estimation. Accordingly, we calculated the upper limit of the branching ratio by multiplying 5.32 to the SES based on Poisson probability,

$$BR(K_L \rightarrow \pi^0 \mu^+ \mu^-) < 4.1 \times 10^{-10} (90\% C.L.).$$

This result represents an improvement of a factor 12 over the current limit of  $Br(K_L \rightarrow \pi^0 \mu^+ \mu^-) < 5.1 \times 10^{-9} (90\% C.L.[10])$ .

## 7.4 Discussions

In this section, we discuss the new result and the future perspective for the search for  $K_L \rightarrow \pi^0 \mu^+ \mu^-$ .

### 7.4.1 Theory

We concluded that the  $Br(K_L \rightarrow \pi^0 \mu^+ \mu^-)$  is less than  $4.1 \times 10^{-10}$  at the 90% confidence level. We could not confirm the existence of the direct CP violation. Our result is consistent with Standard Model, because we did not observe the evidence beyond the Standard Model prediction.

Because the evidence for the direct CP violation was not found, we cannot rule out the Superweak Model. Therefore, this model is still consistent with experiments. Superweak model predicts that there is no contribution from direct CP violation. Therefore, the prediction for the  $Br(K_L \rightarrow \pi^0 \mu^+ \mu^-)$  by superweak model is smaller than Standard Model. Therefore, it is difficult to confirm superweak model. Superweak can survive until a discovery of direct CP violation.

The Leptoquark Model and the Supersymmetric Model predict extra contributions in addition to the contribution by the Standard Model. The prediction of leptoquark Model depends on the mass of the leptoquark. According to Equation 1.8, we excluded leptoquark in the mass( $M_G$ ) region:

$$M_G < 2.5 \times 10^4 GeV/c^2, \quad (7.1)$$

while the allowed value of  $M_G$  in the model is  $100 \sim 10^6 GeV/c^2$ . The supersymmetric model could make the branching ratio about 10 times larger than the prediction by Standard Model\*. Our limit is close to its prediction, but our sensitivity was not low enough for detecting the supersymmetric contribution.

### 7.4.2 Future Perspective of Searching for $K_L \rightarrow \pi^0 \mu^+ \mu^-$

There is no evidence for  $K_L \rightarrow \pi^0 \mu^+ \mu^-$  as described in this thesis. The origin of the CP violation is still one of the mysteries in high energy physics.

---

\*The prediction is only for  $K_L \rightarrow \pi^0 e^+ e^-$ . We assumed that the branching ration of  $K_L \rightarrow \pi^0 \mu^+ \mu^-$  is 1/5 of that of  $K_L \rightarrow \pi^0 e^+ e^-$ [13].

The experimental attempt will continue until the origin of the CP violation is understood. Therefore, the search for  $K_L \rightarrow \pi^0 \mu^+ \mu^-$  should be continued.

Let us consider the future perspective of search for  $K_L \rightarrow \pi^0 \mu^+ \mu^-$ .

### Further Background Rejection

The biggest contribution come from kaon decays which include  $\pi^\pm$  decays, and  $K_L \rightarrow \mu^+ \mu^- \gamma \gamma$ .

In order to reject the kaon decays which include  $\pi^\pm$  decays, tight requirements for finding tracks and vertex are effective. If there are extra drift chambers in upstream and downstream of the analysis magnet, it is effective to reject the decayed  $\pi^\pm$ , also.

Although we observed 5  $K_L \rightarrow \mu^+ \mu^- \gamma \gamma$  events for the first time as described in Appendix A, we cannot confirm the detail characteristics of this decay because of its limited statistics. High statistic study of this decay is necessary for finding effective rejection cuts.

### The number of $K_L$ necessary to see $K_L \rightarrow \pi^0 \mu^+ \mu^-$

In order to discover the  $K_L \rightarrow \pi^0 \mu^+ \mu^-$  decay, the number of the signal events must be significant by more than  $3\sigma$  above the background. In this section, we will assume that the all the background sources are well understood and that the number of the background events is large enough so that the fluctuation can be treated as a Gaussian. This assumption leads to the following relation:

$$N_S > 3\sqrt{N_S + N_{BG}} \quad (7.2)$$

$$N_S = \#K_L \times Br(K_L \rightarrow \pi^0 \mu^+ \mu^-) \times \epsilon_{\pi^0 \mu^+ \mu^-} \quad (7.3)$$

$$N_{BG} = \#K_L \times Prob_{bg}, \quad (7.4)$$

where  $N_S$  is the number of observed  $K_L \rightarrow \pi^0 \mu^+ \mu^-$ ,  $\#K_L$  is the number of  $K_L$  decays,  $N_{bg}$  is the number of observed background events,  $\epsilon_{\pi^0 \mu^+ \mu^-}$  is the detector acceptance for  $K_L \rightarrow \pi^0 \mu^+ \mu^-$ , and  $Prob_{bg}$  is the probability of a  $K_L$  to generate a background event, respectively. (If we use the same condition as in KTeV experiment, we can assume  $\epsilon_{\pi^0 \mu^+ \mu^-} = 0.05$ ,  $Prob_{bg} = 3.3 \times 10^{-12}$ .)

Let us assume the following predicted numbers as described in Chapter 1,

$$\begin{aligned} Br(K_L \rightarrow \pi^0 \mu^+ \mu^-)_{CP\_conserve} &= 4.4 \times 10^{-12} \\ Br(K_L \rightarrow \pi^0 \mu^+ \mu^-)_{indirect} &= 2.0 \times 10^{-13}. \end{aligned} \quad (7.5)$$

To be conservative, the contribution of the direct CP violation is neglected at this time. By using Equation 7.2, we need more than  $6.0 \times 10^{14}$   $K_L$  decays to discover the  $K_L \rightarrow \pi^0 \mu^+ \mu^-$  decay. This corresponds to about 2200 times the  $K_L$  decays in KTeV experiment. If the effective cuts to reject  $K_L \rightarrow \mu^+ \mu^- \gamma \gamma$  with a high statistics study, it will decrease the minimum number of  $K_L$  decays to find  $K_L \rightarrow \pi^0 \mu^+ \mu^-$ .

If we regard the indirect CP violating and CP conserving contributions as background, we can calculate the number of  $K_L$  decays required to detect the direct CP violation. At this time, we can assume  $Prob_{bg} = 7.9 \times 10^{-12}$ . For confirming the direct CP violating  $K_L \rightarrow \pi^0 \mu^+ \mu^-$  with the branching ratio of  $1.0 \times 10^{-12}$ , we need more than  $1.4 \times 10^{15}$   $K_L$  decays.

Fermilab is planning KAMI experiment which is the next generation of KTeV experiment. KAMI plans to observe  $5.6 \times 10^{13}$  kaon decays for searching the direct CP violating phenomena. However, it is still a factor of 10 lower than the sensitivity to detect  $K_L \rightarrow \pi^0 \mu^+ \mu^-$ .

# Chapter 8

## Conclusion

We searched for the decay  $K_L \rightarrow \pi^0 \mu^+ \mu^-$  in this thesis.

We observed two events, while 0.96 background events are expected by Monte Carlo simulation. Therefore, we set an upper limit on the branching ratio to be

$$Br(K_L \rightarrow \pi^0 \mu^+ \mu^-) < 4.1 \times 10^{-10}$$

at the 90% confidence level. This represents an improvement of a factor 12 over the current limit listed by PDG.

Our experiment could not find the existence of the direct CP violation. However, the limit is consistent with Standard Model. While Supersymmetry Model and Leptoquark Model predicted to have extra contributions in addition to the contributions from Standard Model, our search cannot find the evidence for them.

# Appendix A

## $K_L \rightarrow \mu^+ \mu^- \gamma \gamma$ Analysis

The main purpose of this chapter is to search and measure the branching ratio of  $K_L \rightarrow \mu^+ \mu^- \gamma \gamma$ .  $K_L \rightarrow \mu^+ \mu^- \gamma \gamma$  is the most dangerous background but has never been observed.

First, we describe the backgrounds to  $K_L \rightarrow \mu^+ \mu^- \gamma \gamma$ . Next, we describe the requirements for  $K_L \rightarrow \mu^+ \mu^- \gamma \gamma$  and the consistency between data and MC events. Furthermore, we describe the systematic error on the single event sensitivity. Finally, we calculate the branching ratio of  $K_L \rightarrow \mu^+ \mu^- \gamma \gamma$ . For this analysis, we used the same data sample and MC events as  $K_L \rightarrow \pi^0 \mu^+ \mu^-$ .

### A.1 Backgrounds to $K_L \rightarrow \mu^+ \mu^- \gamma \gamma$

Table A.1 summarizes the backgrounds to  $K_L \rightarrow \mu^+ \mu^- \gamma \gamma$ . There are two kinds of background sources:  $K_L \rightarrow \mu^+ \mu^- \gamma$  and kaon decays including  $\pi^\pm$ s which are misidentified as muons. The mechanisms for misidentification are described in Section 4.1.

Decay mode	Branching Ratio
$K_L \rightarrow \mu^+ \mu^- \gamma + \gamma_{acc}$	$3.23 \times 10^{-7}$
$K_L \rightarrow \pi^0 \pi^+ \pi^-$	0.123
$K_L \rightarrow \pi^\pm \mu^\mp \nu(\bar{\nu}) + 2\gamma_{acc}$	0.273
$K_L \rightarrow \pi^+ \pi^- + 2\gamma_{acc}$	$2.03 \times 10^{-3}$
$K_L \rightarrow \pi^+ \pi^- \gamma + \gamma_{acc}$	$4.61 \times 10^{-5}$
$K_L \rightarrow \pi^0 \pi^\pm \mu^\mp \nu$	$5.88 \times 10^{-5}$

Table A.1: Background candidates to  $K_L \rightarrow \mu^+ \mu^- \gamma \gamma$  with their branching ratio

## A.2 Event Selection

The event reconstruction and particle identifications used the same procedure and requirements as  $K_L \rightarrow \pi^0 \mu^+ \mu^-$ . Here, we will describe the kinematic requirements which were different from  $K_L \rightarrow \pi^0 \mu^+ \mu^-$  analysis.

### A.2.1 Photon Energy

$K_L \rightarrow \mu^+ \mu^- \gamma \gamma$  is  $K_L \rightarrow \mu^+ \mu^- \gamma$  with an internal bremsstrahlung photon. The photon in  $K_L \rightarrow \mu^+ \mu^- \gamma$  has large energy because  $K_L \rightarrow \mu^+ \mu^- \gamma$  comes from the intermediate state  $K_L \rightarrow \gamma^* \gamma$ .  $K_L \rightarrow \pi^\pm \mu^\mp \nu(\bar{\nu})$  becomes a background to  $K_L \rightarrow \mu^+ \mu^- \gamma \gamma$  when the  $\pi^\pm$  is misidentified as muon and there are two accidental photons. The accidental photons typically have low energy as shown in Figure A.1. We require at least one photon to have more than 10 GeV. This cut retains 81.8% of signal while rejecting 36.1% of  $K_L \rightarrow \pi^\pm \mu^\mp \nu(\bar{\nu})$  events.

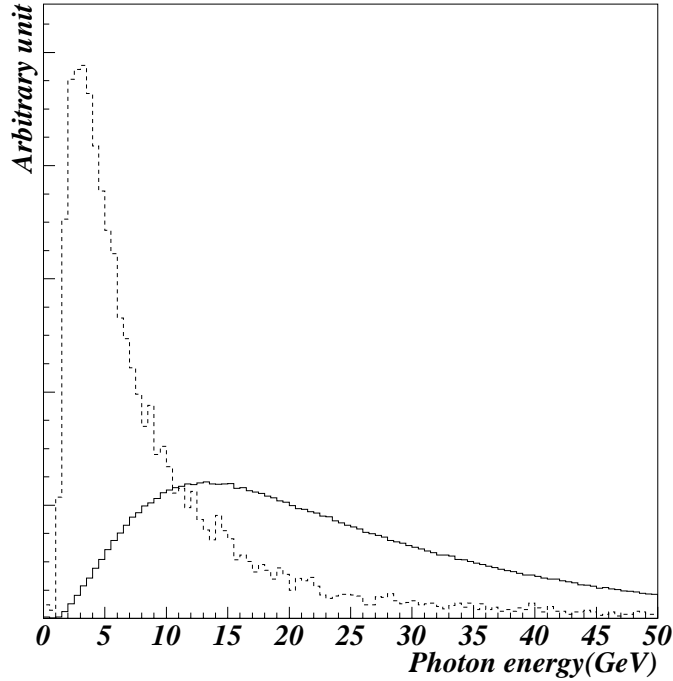


Figure A.1: The energy distribution of the photon in the  $K_L \rightarrow \mu^+ \mu^- \gamma$ (solid) and the accidental photon(dot).

### A.2.2 $\pi^0$ mass

The photons in  $K_L \rightarrow \pi^0 \pi^+ \pi^-$  and  $K_L \rightarrow \pi^0 \pi^\pm \mu^\mp \nu$  come from  $\pi^0 \rightarrow \gamma \gamma$ . Therefore, the reconstructed mass of two photons is peaked at  $135 \text{ MeV}/c^2$ . In

case of  $K_L \rightarrow \mu^+ \mu^- \gamma \gamma$ , the  $M_{\gamma\gamma}$  has a wide distribution as shown in Figure A.2. We required the  $M_{\gamma\gamma}$  to be less than  $130(MeV/c^2)$ . This cut rejected most of  $K_L \rightarrow \pi^0 \pi^\pm \mu^\mp \nu$  and  $K_L \rightarrow \pi^0 \pi^+ \pi^-$  which include punched through  $\pi^\pm$ , while keeping 52% of signal.

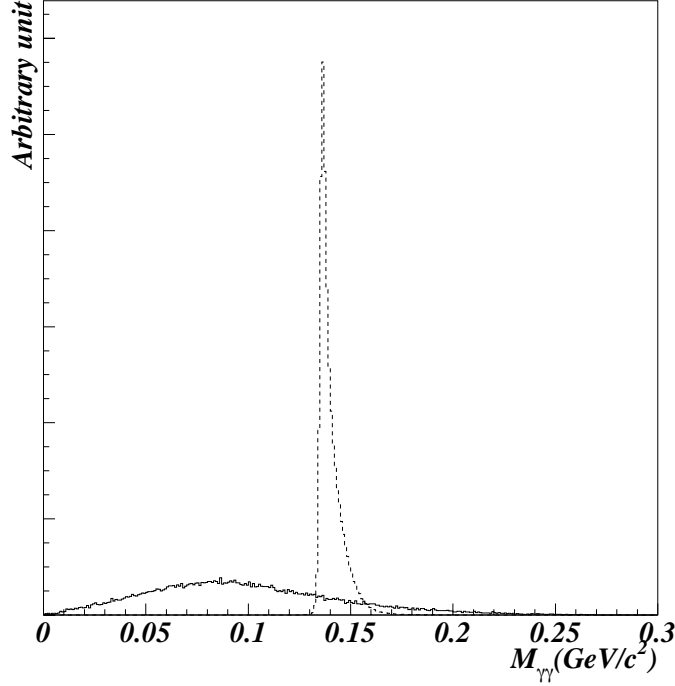


Figure A.2: The  $\pi^0$  distribution of the  $K_L \rightarrow \mu^+ \mu^- \gamma \gamma$  MC events(solid line) and  $K_L \rightarrow \pi^0 \pi^+ \pi^-$  MC events(dash line) after particle identification. These distributions are normalized by area.

### A.2.3 Missing Longitudinal Momentum Parameter( $P_{\pi^0}^2$ )

About 8% of  $K_L \rightarrow \pi^0 \pi^+ \pi^-$  with both  $\pi^\pm$  decayed can survive  $M_{\gamma\gamma}$  cut, because the  $M_{\gamma\gamma}$  distribution for those events was smeared by the mismeasurement of the track momentum.

In the  $K_L \rightarrow \mu^+ \mu^- \gamma \gamma$  analysis, we used  $P_{\pi^0}^2$  to reject  $K_L \rightarrow \pi^0 \pi^+ \pi^-$  by using Equation 4.3 assuming  $\pi^\pm$  mass for the charged tracks. Figure A.3 shows the  $P_{\pi^0}^2$  distribution of MC events for  $K_L \rightarrow \mu^+ \mu^- \gamma \gamma$ , and  $K_L \rightarrow \pi^0 \pi^+ \pi^-$  where both  $\pi^\pm$ s decayed in flight. For the  $K_L \rightarrow \pi^0 \pi^+ \pi^-$  events,  $P_{\pi^0}^2$  is larger than 0 with some smearing which was caused by resolution and mismeasurement of the decayed  $\pi$  momentum.  $K_L \rightarrow \mu^+ \mu^- \gamma \gamma$  distribution is peaked below 0. We required the  $P_{\pi^0}^2$  to be less than -0.06. The efficiency of this cut for the signal is 92.2%. The 92.7% of  $K_L \rightarrow \pi^0 \pi^+ \pi^-$  was rejected by this cut.

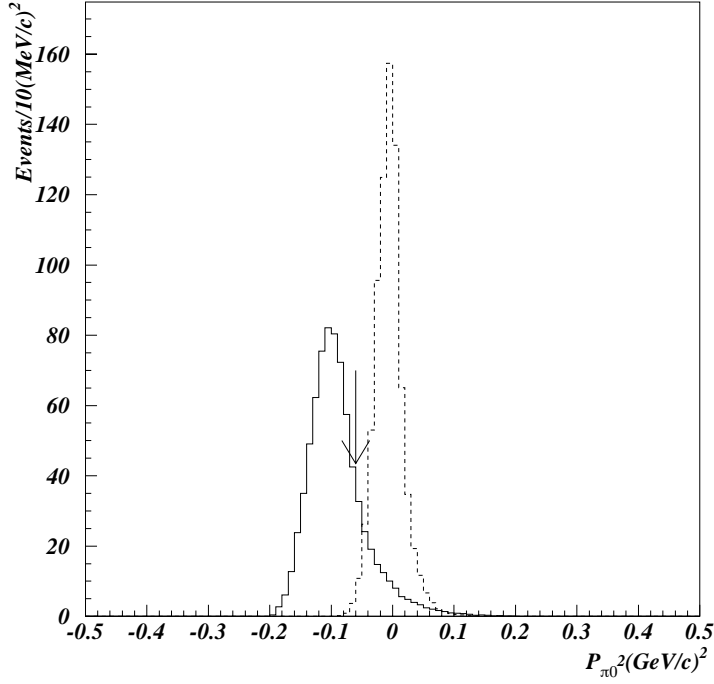


Figure A.3:  $P_{\pi^0}^2$  distribution for  $K_L \rightarrow \mu^+ \mu^- \gamma \gamma$  (solid line) and  $K_L \rightarrow \pi^0 \pi^+ \pi^-$  (dashed line) which include both  $\pi^\pm$  decayed in flight. We required the  $P_{\pi^0}^2$  to be less than -0.06 as indicated arrow in the plot. The distributions are normalized by area.

#### A.2.4 Invariant Mass of the Charged Tracks ( $M_{\mu\mu}$ )

The  $M_{\mu\mu}$  distribution for  $K_L \rightarrow \mu^+ \mu^- \gamma \gamma$  and  $K_L \rightarrow \pi^\pm \mu^\mp \nu(\bar{\nu})$  decays are shown in Figure A.4. Since the  $M_{\mu\mu}$  distribution is different between  $K_L \rightarrow \pi^\pm \mu^\mp \nu(\bar{\nu})$  and  $K_L \rightarrow \mu^+ \mu^- \gamma \gamma$ , we required the  $M_{\mu\mu}$  to be less than  $340 \text{ MeV}/c^2$ . The efficiency of this cut for the signal is 77.7%. The 92.9% of  $K_L \rightarrow \pi^\pm \mu^\mp \nu(\bar{\nu})$  decays were rejected by this cut.

#### A.2.5 Angle between 2 Photons

A useful quantity for rejecting the  $K_L \rightarrow \pi^\pm \mu^\mp \nu(\bar{\nu})$  events from  $K_L \rightarrow \mu^+ \mu^- \gamma \gamma$  signal region is  $\cos\theta_{\gamma\gamma}$ , where  $\theta_{\gamma\gamma}$  is the opening angle between two photons in the center of the mass system, as illustrated in Figure A.5. For  $K_L \rightarrow \mu^+ \mu^- \gamma \gamma$ ,  $\cos\theta_{\gamma\gamma}$  is peaked at -1 as shown in Figure A.6, which means the two photons are emitted back-to-back. In case of  $K_L \rightarrow \pi^\pm \mu^\mp \nu(\bar{\nu})$ , the two photons are accidental photons, so there is no correlation between the photons. We required the  $\cos\theta_{\gamma\gamma}$  to be less than -0.3. The efficiency of this cut for the signal is 77.1%. This cut rejects 85.3% of  $K_L \rightarrow \pi^\pm \mu^\mp \nu(\bar{\nu})$ .

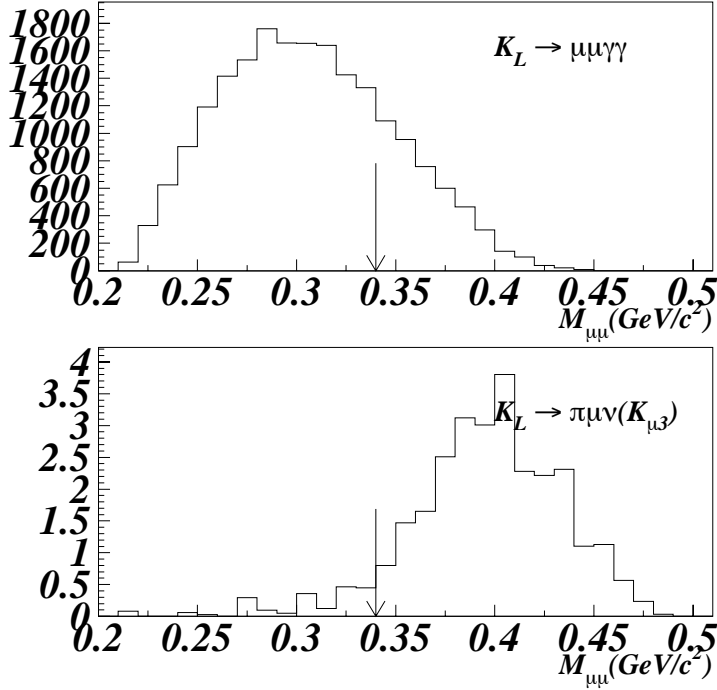


Figure A.4:  $M_{\mu\mu}$  distribution for each decay after the  $\pi^0$  mass cut. The upper plot shows the distribution for the  $K_L \rightarrow \mu^+\mu^-\gamma\gamma$ . The lower plot shows the distribution for the  $K_L \rightarrow \pi^\pm\mu^\mp\nu(\bar{\nu})$ . We required  $M_{\mu\mu} < 0.34\text{GeV}/c^2$  as indicated by the arrow.

### A.2.6 Kaon mass and $P_T^2$

Kaon mass and  $P_T^2$  requirements are exactly the same as the  $K_L \rightarrow \pi^0\mu^+\mu^-$  analysis. ( $492 < M_K \text{ MeV}/c^2 < 504$  and  $P_T^2 < 100(\text{MeV}/c)^2$ )

### A.2.7 Summary of the Event Selection

Table A.2 lists the analysis cuts, and the efficiencies for the  $K_L \rightarrow \mu^+\mu^-\gamma\gamma$  MC events at each stage. The acceptance was corrected for muon energy deposit and MU3 efficiency as was for the  $K_L \rightarrow \pi^0\mu^+\mu^-$ .

The acceptance for the  $K_L \rightarrow \mu^+\mu^-\gamma\gamma$  after corrections is 0.14%. In Section 4.7, we observed 377919  $K_L \rightarrow \pi^0\pi^+\pi^-$  events, and derived that the number of kaon decays in this experiment is  $2.68 \times 10^{11}$ .

The daughter particles of  $K_L \rightarrow \mu^+\mu^-\gamma\gamma$  are exactly the same as  $K_L \rightarrow \pi^0\mu^+\mu^-$ . Therefore, the sources of the uncertainty on SES were the same as for  $K_L \rightarrow \pi^0\mu^+\mu^-$ . We estimated the systematic uncertainties of the SES for  $K_L \rightarrow \mu^+\mu^-\gamma\gamma$  with the same procedure as for  $K_L \rightarrow \pi^0\mu^+\mu^-$ .

Table A.3 summarizes all the systematic uncertainties on the SES of  $K_L \rightarrow$

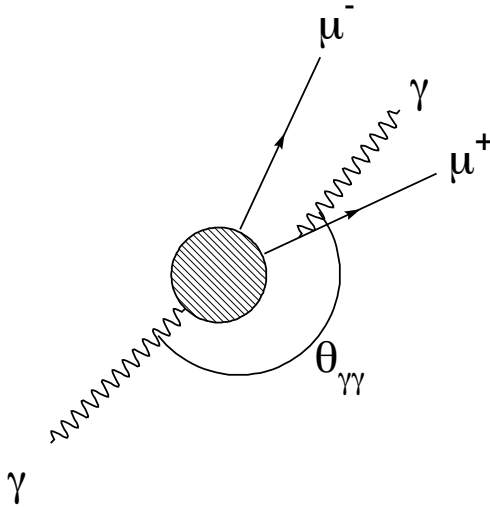


Figure A.5: The illustration showing the angle between two photons in the center of mass system.

$\mu^+\mu^-\gamma\gamma$ . By summing each uncertainty quadratically, we obtained the overall uncertainty of 7.09%. We generated  $K_L \rightarrow \mu^+\mu^-\gamma\gamma$  event with  $M_{\gamma\gamma} > 1MeV/c^2$ . According to Equation 4.4 and the acceptance of  $K_L \rightarrow \mu^+\mu^-\gamma\gamma$ , the single event sensitivity for  $K_L \rightarrow \mu^+\mu^-\gamma\gamma$  in this experiment is

$$SES(K_L \rightarrow \mu^+\mu^-\gamma\gamma, M_{\gamma\gamma} \geq 1MeV/c^2) = [2.63 \pm 0.0037(stat.) \pm 0.186(sys.)] \times 10^{-9}.$$

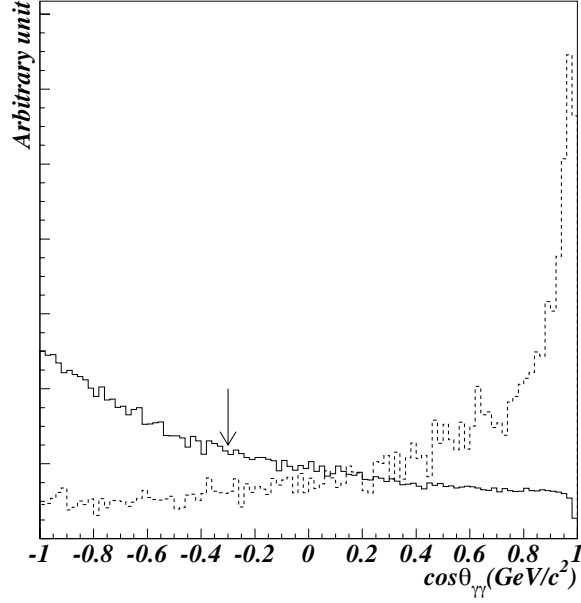


Figure A.6: The  $\cos\theta_{\gamma\gamma}$  distribution of  $K_L \rightarrow \mu^+\mu^-\gamma\gamma$  and  $K_L \rightarrow \pi^\pm\mu^\mp\nu(\bar{\nu})$ . The solid(dashed) line represents the distribution for  $K_L \rightarrow \mu^+\mu^-\gamma\gamma(K_L \rightarrow \pi^\pm\mu^\mp\nu(\bar{\nu}))$  after  $P_{\pi_0}^2$  cut. The arrow shows our requirement.

Cut	$K_L \rightarrow \mu^+\mu^-\gamma\gamma$ MC
Level 1,2	27.4%
Level 3	83.5%
Event Reconstruction	5.1%
Muon energy	92.8%
Track Momentum	76.3%
Photon Energy	81.8%
$M_{\gamma\gamma}$	52.1%
$P_{\pi_0}^2$	92.2%
$M_{\mu\mu}$	76.9%
Angle between two photons	77.1%
$P_T^2$	76.7%
Kaon mass	93.8%
Kaon momentum	100.0%
muon energy deposit in CsI correction	+3.3%
MU3 efficiency correction	-1.2%
Acceptance of $K_L \rightarrow \mu^+\mu^-\gamma\gamma$	0.14%

Table A.2: Analysis Cuts and efficiencies for  $K_L \rightarrow \mu^+\mu^-\gamma\gamma$ .

Source of Uncertainty	(%)
BR( $K_L \rightarrow \pi^0 \pi^+ \pi^-$ )	1.59
MC statistics	0.224
Energy shifted by 0.7%	5.11
Energy smeared by 0.3%	0.0987
Inner crystal energy shifted by 1.0%	0.0121
Inner crystal energy smeared by 0.9%	0.174
Momentum scale shifted by 0.30%	0.557
Momentum resolution smeared by 0.53%	0.803
$\chi_{vertex}^2$	0.239
$\pi^0$ mass	1.47
Chamber inefficiency	0.320
Particle identification	4.20
Trigger difference	0.802
Total Systematic Uncertainty	7.09

Table A.3: The systematic error from each source.

## A.3 Background Estimation

We will describe the background estimation for  $K_L \rightarrow \mu^+ \mu^- \gamma \gamma$ . First, we describe the uncertainty of the expected number of the background. Furthermore, we will describe the consistency between data and MC.

### A.3.1 Correction for Background Estimation

As described in Chapter 3, we generated the background decays which include  $\pi^\pm$  by using two special techniques to simulate  $\pi^\pm$  decay and  $\pi^\pm$  punchthrough. However, as shown in Figure 3.2, the  $\pi^\pm$  generated by MC have a smaller probability of being misidentified as muons. This discrepancy can underestimate the number of background events in the signal region. In order to estimate the effect of this discrepancy, the event weight of the  $\pi^\pm$  in the momentum range 10-15(15-20)GeV/c was increased by 17%(6.48%). Only the background from  $K_L \rightarrow \pi^\pm \mu^\mp \nu(\bar{\nu})$  decay had events with  $\pi^\pm$  below 20 GeV/c, surviving all the cuts. The changes in the number of background events are summarized in Table A.4.

mode	option	Size of the correction(%)
$K_L \rightarrow \pi^\pm \mu^\mp \nu(\bar{\nu})$	D	+5.02
$K_L \rightarrow \pi^\pm \mu^\mp \nu(\bar{\nu})$	P	+16.8

Table A.4: The summary of the correction for the misidentification. D represents a  $\pi^\pm$  decayed in flight before the CsI calorimeter. P means that a  $\pi^\pm$  punched through the muon filters.

### A.3.2 Uncertainty of the background estimation

The estimated number of background events was a product of three components: the number of decayed parent particles, branching ratio, and acceptance. This section will describe the uncertainty of these contributions.

#### Monte Carlo statistics

We estimated the number of remaining events for each background by generating 17.9 to  $2 \times 10^4$  times larger MC sample than real data as summarized in Table 5.5. Only  $K_L \rightarrow \pi^\pm \mu^\mp \nu(\bar{\nu})$  can survived all the cuts for selecting  $K_L \rightarrow \mu^+ \mu^- \gamma \gamma$ .  $K_L \rightarrow \pi^\pm \mu^\mp \nu(\bar{\nu})$  decay was generated with a weight for each event. We estimated systematic error of the MC events for each case as described in Section 5.3.2. Table A.5 summarizes the statistical uncertainties on the MC events.

mode	Uncertainty(%)
$K_L \rightarrow \mu^+ \mu^- \gamma$	30.3
$K_L \rightarrow \pi^\pm \mu^\mp \nu(\bar{\nu})\text{D}$	37.6
$K_L \rightarrow \pi^\pm \mu^\mp \nu(\bar{\nu})\text{P}$	35.7

Table A.5: The summary of the uncertainty of the background decays to  $K_L \rightarrow \mu^+ \mu^- \gamma \gamma$  from the MC statistics.

### Branching Ratio

As well as  $K_L \rightarrow \pi^0 \pi^+ \pi^-$ , the Particle Data Group's[4] branching ratios were used to estimate the number of the background events in the signal region. Table A.6 lists the uncertainties in the branching ratios for all the background decays.

mode	Uncertainty(%)
$K_L \rightarrow \mu^+ \mu^- \gamma$	8.61
$K_L \rightarrow \pi^\pm \mu^\mp \nu(\bar{\nu})$	0.920

Table A.6: The summary of the uncertainty from the branching ratio of the background decays.

### The number of $K_L$ decays

The statistics of the accepted  $K_L \rightarrow \pi^0 \pi^+ \pi^-$  MC led to an error of 0.150%, and the number of observed  $K_L \rightarrow \pi^0 \pi^+ \pi^-$  led to an uncertainty of 0.163%. The quadratic sum of the two sources came to be 0.221%.

### A.3.3 Summary for backgrounds

Table A.7 summarizes the expected number of background events with their uncertainties after the corrections described in Section 5.2. The total number of background events was estimated to be  $0.70 \pm 0.21$  by MC. The background was dominated by  $K_L \rightarrow \pi^\pm \mu^\mp \nu(\bar{\nu})$  with a  $\pi^\pm$  decayed in flight.

### A.3.4 Consistency between Data and MC

We estimated the number of background events which passed all the  $K_L \rightarrow \mu^+ \mu^- \gamma \gamma$  requirements. In order to confirm our understanding of the background, we will compare the background MC events and data.

decay mode	option	#events
$K_L \rightarrow \mu^+ \mu^- \gamma + \gamma_{acc}$		$0.143 \pm 0.0450$
$K_L \rightarrow \pi^0 \pi^+ \pi^-$	DD	$< 0.0558$
$K_L \rightarrow \pi^0 \pi^+ \pi^-$	DP	$< 0.0106$
$K_L \rightarrow \pi^0 \pi^+ \pi^-$	PP	$< 0.0105$
$K_L \rightarrow \pi^\pm \mu^\mp \nu(\bar{\nu}) + 2\gamma_{acc}$	D	$0.362 \pm 0.136$
$K_L \rightarrow \pi^\pm \mu^\mp \nu(\bar{\nu}) + 2\gamma_{acc}$	P	$0.199 \pm 0.0702$
$K_L \rightarrow \pi^0 \pi^\pm \mu^\mp \nu$	D	$< 0.00454$
$K_L \rightarrow \pi^0 \pi^\pm \mu^\mp \nu$	P	$< 0.00413$
$K_L \rightarrow \pi^+ \pi^- \gamma + \gamma_{acc}$	all	negligible
$K_L \rightarrow \pi^+ \pi^- + 2\gamma_{acc}$	all	negligible
Total		$0.704 \pm 0.211$

Table A.7: Summary of the number of the events from various background source. D represented a  $\pi^\pm$  decayed in flight before CsI calorimeter. P denoted that a  $\pi^\pm$  punched through the muon filter.

### Comparisons in Side Bands

In this section, we will compare the number of background events in the side band region in the reconstructed mass and  $P_T^2$  distributions between data and MC.

Figure A.7 shows the reconstructed kaon mass distribution with all the cuts except for kaon mass cut. In the region (A) ( $0.48 < M_{\pi^0 \mu^+ \mu^-} (GeV/c^2) < 0.492$ ), there are 2 events in data, while MC predicted  $0.72 \pm 0.27$  events. In region (C) ( $0.504 < M_{\pi^0 \mu^+ \mu^-} (GeV/c^2) < 0.515$ ), there are no events left in data, while MC predicted  $1.57 \pm 0.20$  events. Both kinds of  $K_L \rightarrow \pi^\pm \mu^\mp \nu(\bar{\nu}) + 2\gamma_{acc}$  events ( $\pi^\pm$  decay in flight and  $\pi^\pm$  punch through) were scattered in all region at random. In the region (C), half of the survived events are  $K_L \rightarrow \mu^+ \mu^- \gamma + \gamma_{acc}$ . In regions (A), the difference between the expected number of events and the observed number of events are within statistical error. The region (B) is the signal region for the  $K_L \rightarrow \mu^+ \mu^- \gamma \gamma$ , and events in data are still being masked.

Figure A.8 shows the  $P_T^2$  distribution with all the cuts except for the  $P_T^2$  cut. There are 3 events in region (B) ( $0.0001 < P_T^2 (GeV/c)^2 < 0.0005$ ) and 7 events in region (C) ( $0.0005 < P_T^2 (GeV/c)^2 < 0.001$ ), respectively. MC predicts number of background events;  $0.70 \pm 0.21$  events in the signal region (A) ( $P_T^2 < 0.0001$ ),  $4.69 \pm 0.70$  events in region (B),  $4.74 \pm 0.66$  events in region (C). The numbers in region (B) and (C) were consistent between data and MC within statistical error. The events in all regions are dominated by  $K_L \rightarrow \pi^\pm \mu^\mp \nu(\bar{\nu}) + 2\gamma_{acc}$  with both  $\pi^\pm$  misidentification cases.

### A.3.5 Summary of the background estimation

We conclude that the sources of background are well understood, and the shape of each source is correctly reproduced in MC. The number of background events

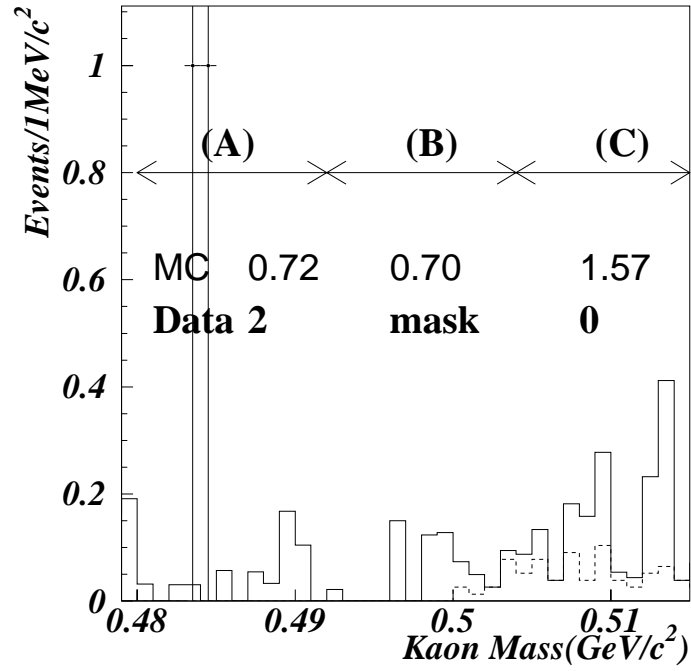


Figure A.7: The kaon mass distribution in the  $P_T^2 < 100(\text{MeV}/c)^2$  region. The dot indicates the data. The open histogram represents the summed MC. The dashed line shows the contribution from  $K_L \rightarrow \mu^+ \mu^- \gamma + \gamma_{acc}$ . Most of the other contribution is from  $K_L \rightarrow \pi^\pm \mu^\mp \nu(\bar{\nu}) + 2\gamma_{acc}$ .

in the side band region are well reproduced.

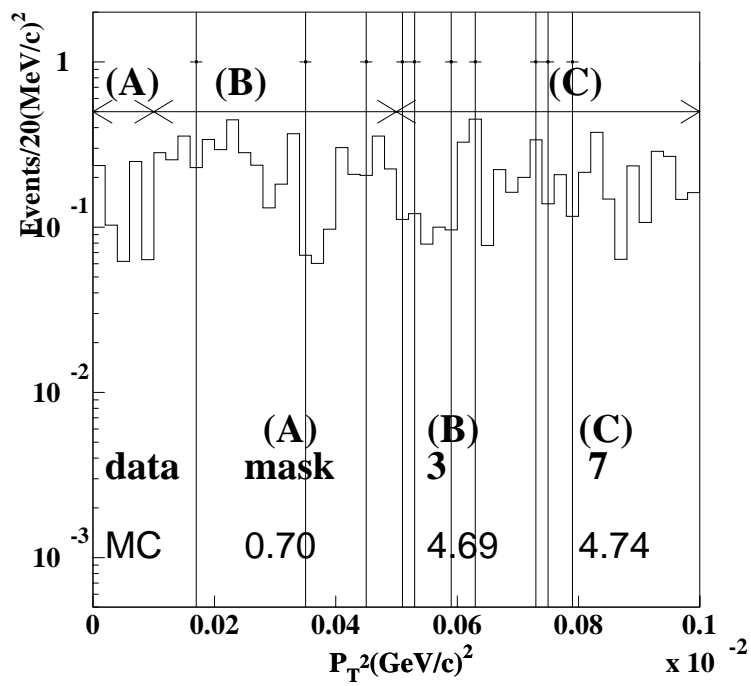


Figure A.8: The  $P_T^2$  distribution in the kaon mass region. The dots indicate data. The open histogram represents the summed MC.

## A.4 Criteria for claiming $K_L \rightarrow \mu^+ \mu^- \gamma \gamma$ observation

As described in Section 7.1, we will define the criteria for claiming the discovery of  $K_L \rightarrow \mu^+ \mu^- \gamma \gamma$ . Table A.8 shows the expected number of background events based on the Poisson distribution. The calculation was based on 0.70 background events.

#observed	Poisson Prob.
0	0.4946
1	0.3482
2	0.1225
3	0.02876
4	0.00506
5	0.000713
6	0.000084

Table A.8: Poisson probabilities to the observed background events while 0.704 background events are expected.

Usually, we require more than  $3\sigma$  significance to claim a new discovery. This means that the probability of making an error is less than 0.3%, based on the Gaussian distribution. In our case, this corresponds to the probability of observing 5 or more events. Therefore, if we find 5 or more events in the signal region, we will claim the discovery of  $K_L \rightarrow \mu^+ \mu^- \gamma \gamma$ .

## A.5 Result

Figure A.9 shows the reconstructed kaon mass distribution with all the cuts except for the kaon mass cut.

We observed 5 events in the signal region, which lead to claim the discovery. Finally, we calculated the branching ratio from the results. We set

$$BR(K_L \rightarrow \mu^+ \mu^- \gamma \gamma, M_{\gamma\gamma} \geq 1 \text{ MeV}/c^2) = [1.13 \pm 0.55(\text{stat}) \pm 0.08(\text{sys.})] \times 10^{-8}.$$

The result is consistent with QED prediction,  $BR(K_L \rightarrow \mu^+ \mu^- \gamma \gamma) = [9.1 \pm 0.78] \times 10^{-9}$ .

Usually, the branching ratio of the decay which include radiative photon is measured with the cutoff energy in the center of mass system. Figure A.10 shows the energy of the radiative photon in the center of mass system for the event at the generation and after all cuts. According to the distribution of the accepted events, we calculated the branching ratio of  $K_L \rightarrow \mu^+ \mu^- \gamma \gamma$  with the cutoff  $E^* > 10 \text{ MeV}$ .

$$BR(K_L \rightarrow \mu^+ \mu^- \gamma \gamma, E^* \geq 10 \text{ MeV}) = [1.55 \pm 0.74(\text{stat}) \pm 0.11(\text{sys.})] \times 10^{-9}.$$

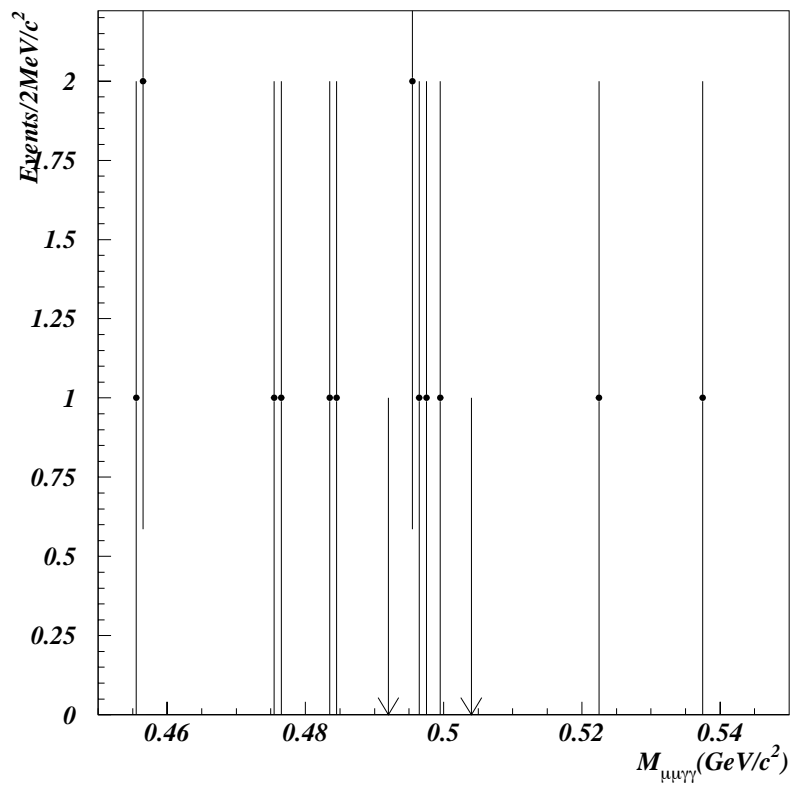


Figure A.9: The reconstructed mass distribution with all cuts except for the mass cut. There are two events in the masked region.

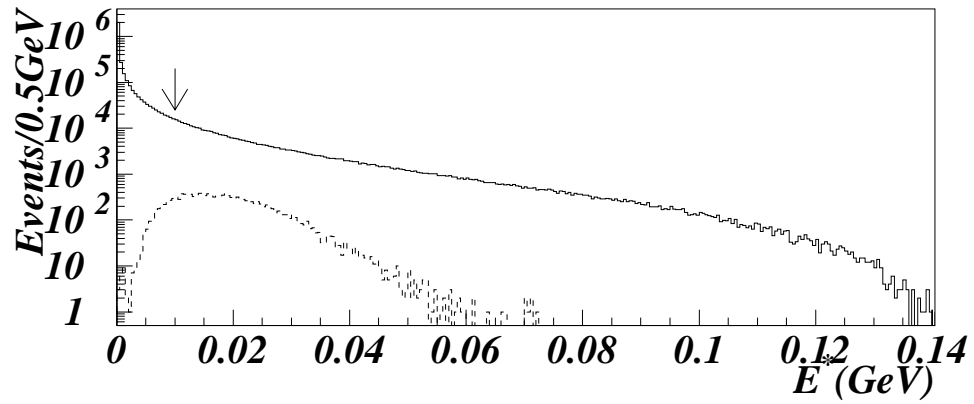


Figure A.10: The spectrum of the minimum energy photon in our  $K_L \rightarrow \mu^+ \mu^- \gamma \gamma$  MC events. The solid line shows the spectrum at the generation. The dashed line shows the spectrum for the accepted events. The arrow shows the cutoff which was used to calculate the branching ratio.

# Appendix B

## Measurement of the Muon Scattering in Muon system

We measured the scattering angle distribution of muons by Muon run data. The momentum kick of the spectrometer magnet was set to be 204 MeV/c to measure the muon momentum. We took the data with a trigger which required more than 1 hit in both the V trigger bank and the Mu2 bank.

In order to measure the muon scattering angle in the muon system, the following conditions were required to the Muon Run data \*.

- 1 reconstructed track pointing to the CsI calorimeter.
- More than 1 hit in the MU2 bank.
- 1 hit in each MU3 bank.(no extra hit)
- The extrapolated position of the both downstream tracks is more than 20cm from MU3 bank edge.

After selecting events which satisfied above requirements, we calculated deflected distance( $\delta_{scat}$ ) at MU3 bank,

$$\delta_{scat} = MISPOS_{MU3} - CPOS_{MU3}, \quad (B.1)$$

for x and y direction, where  $MISPOS_{MU3}$  represents the extrapolated track position at MU3 bank, and  $CPOS_{MU3}$  represents center of the hit counter position. We fitted the distribution of  $\delta_{scat}$  to Gaussian at each 1GeV/c momentum range for each direction as shown in Figure B.1. Figure B.2 shows the fitted sigma as a function of the muon momentum.

Furthermore, we fit the distribution as shown in Figure B.2 from 8 (GeV/c) to 13 (GeV/c) to the function: $f(x) = a/p(\text{GeV}/c) + b$  where  $a$  and  $b$  were fit parameters. The  $\delta_{scat}$  for high momentum muon came from the counter width. Therefore, the fit range was selected to avoid the effect from the counter width.

Figure B.3 shows  $\delta_{scat}$  of the muon in  $K_L \rightarrow \pi^\pm \mu^\mp \nu(\bar{\nu})$  for the data and MC which used the function  $f(x)$ . There is a 5 % discrepancy in range 15~30GeV/c, but the scattering for the other momentum range is well-reproduced.

---

\*The detail of the event reconstruction were described in Section 4.3.

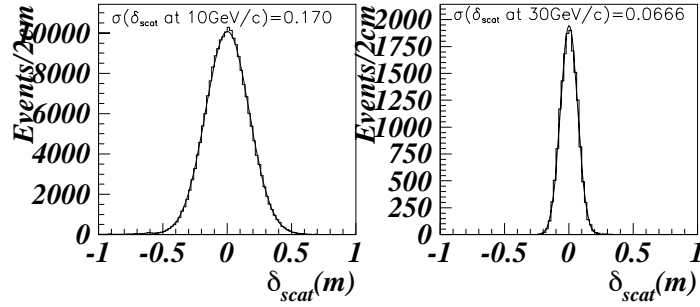


Figure B.1: The  $\delta_{scat}$  distribution. The left plot shows the distribution for 10~11GeV/c muons. The right plot shows the distribution for 30~31GeV/c.

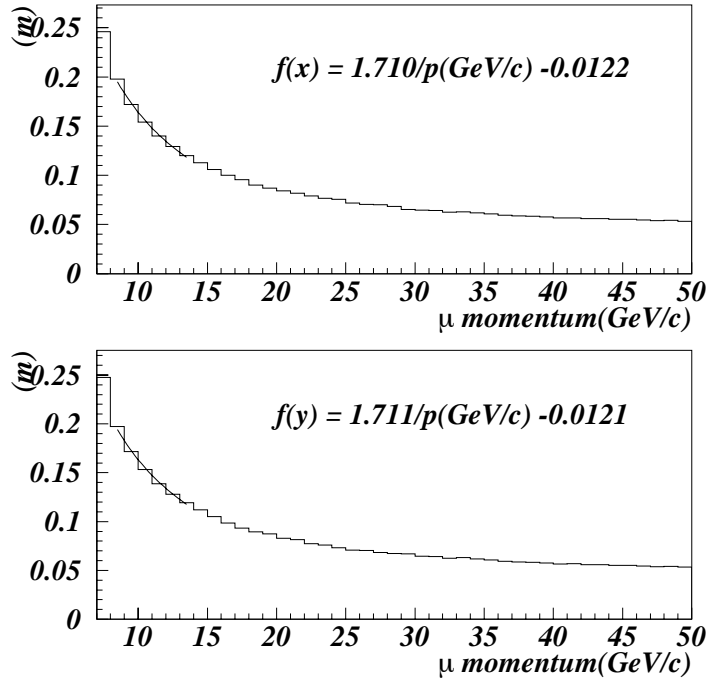


Figure B.2: The  $\delta_{scat}$  distribution as a function of the muon momentum. The upper plot shows the distribution for x direction. The lower plot shows the distribution for y direction.

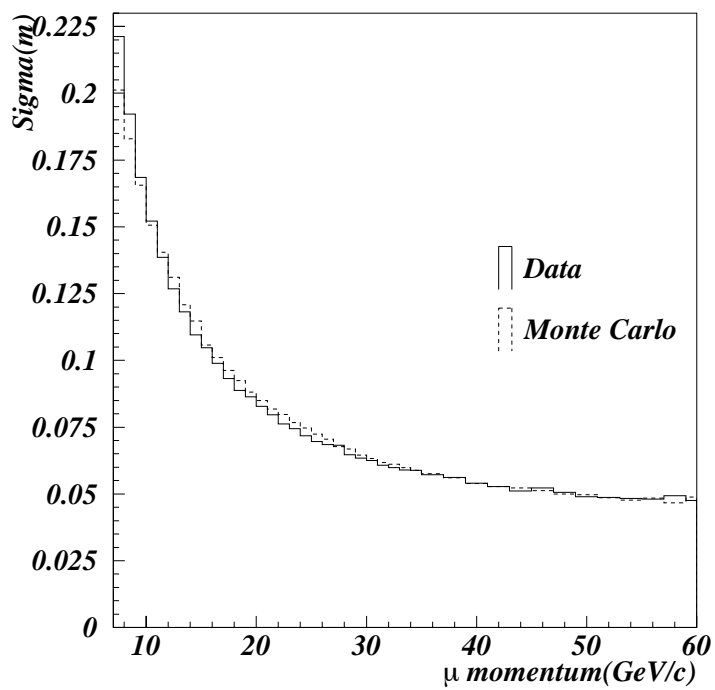


Figure B.3: The  $\delta_{scat}$  distribution as a function of  $\mu$  momentum for data(solid) and MC(dash) in  $K_L \rightarrow \pi^\pm \mu^\mp \nu(\bar{\nu})$  decays.

# Bibliography

- [1] J. H. Christenson, J. W. Cronin, V. L. Fitch, R. Turlay, Phys. Rev. Lett. 13(1964)138.
- [2] L. Maiani, in Proceedings of the International
- [3] L. Wolfenstein, Phys. Rev. Lett. 51(1983)1945.
- [4] Particle Data Group, Phys. Rev. D54, (1996)1.
- [5] S. Bennett et al, Phys. Rev. Lett. 19(1967)993.
- [6] D. Dorfan et al, Phys. Rev. Lett. 19(1967)987.
- [7] L.K.Gibbons et al., Phys. Rev. Lett. 70.(1993)1199.
- [8] G.D.Barr et al.,Phys. Lett. B317(1993)233.
- [9] D.A. Harris et al.,Phys. Rev. Lett. 71.(1993)3918.
- [10] D.A. Harris et al.,Phys. Rev. Lett. 71.(1993)3914.
- [11] J. Adams et al.,Phys. Lett. B447(1999)240.
- [12] L. Littenberg and G. Valencia, Rare and radiative kaon decays, Technical Report FERMILAB-Pub-93-004, Fermilab, March 1993.
- [13] L.M. Sehgal, Phys. Rev.D38(1988)808.
- [14] S.Adler et al.,Phys. Rev. Lett. 79.(1997)4756.
- [15] G. Ecker, Preprint hep-ph/9608226.
- [16] P.Heiliger and L.M. Sehgal, Phys. Rev. D 47.(1993)4920.
- [17] G.Ecker,A.Pich, and E. de Rafael, Nucl. Phys. B**291**(1987)692.
- [18] L.Wolfenstein, Phys. Rev. Lett., 13(1964)562.
- [19] L. Hall and L.Randall, Nucl. Phys. B274(1986)157.
- [20] G. Colangelo and G. Isidori, Preprint LNF-98-026-P, hep-ph/9808487.

- [21] G.Ecker,A.Pich, and E. de Rafael, Nucl. Phys. B303(1988)665.
- [22] A.J. Malensek, Preprint FN-341, Fermi National Accelerator Laboratory, October 1981.
- [23] N.M. Kroll and W.Wada, Phys. Rev. 98.(1955)1355.
- [24] G. Donaldson et al, Phys. Rev. D9.(1974)2960.
- [25] W.R. Nelson, H. Hirayama, and W.O. Rogers, The egs4 code system, Preprint SLAC Report-265, Stanford Linear Accelerator Center, 1985.
- [26] A.F. Bielajew, Preprint PIRS-0287(1991).
- [27] GEANT Detector Description and Simulation Tool, CERN Program Library Long Writeup W5013.
- [28] R. Talman, Nucl. Inst. and Math. 159(1979)189.
- [29] H.Maccabee and D. Padworth, Phys. Lett. A30(1969)241.
- [30] R.A. Briere, PhD thesis, University of Chicago, June 1995.
- [31] R.J. Tesarek, KTeV Internal Memo 0184, June 1994.
- [32] Louis Lyons, Statistics for nuclear and particle physicists,(Cambridge University Press) Sec 1.4.2, page 13.